A regionally refined and mass-consistent atmospheric and hydrological de-aliasing product for GRACE, GRACE-FO and future gravity missions

Anne Springer[1], Christian A. Mielke[1], Ziyu Liu[2], Shashi Dixit[2], Petra Friederichs[2], Jürgen Kusche[1]

[1]Institute of Geodesy and Geoinformation, University of Bonn, Bonn, Germany
[2]Institute of Geosciences, University of Bonn, Bonn, Germany

Key Points:

- We provide an atmosphere-hydrology de-aliasing product with regional mass-consistent refinement over Europe.
- Using non-hydrostatic as opposed to hydrostatic numerical weather prediction model output significantly impacts the de-aliasing product.
- We found that for extreme events additional moisture fields unaccounted in present AOD models can reach magnitudes relevant for de-aliasing.

Corresponding author: Anne Springer, springer@geod.uni-bonn.de

Corresponding author: Christian A. Mielke, mielke@geod.uni-bonn.de

Abstract

De-aliasing products are used in the estimation process of satellite-based gravity field computation to reduce errors from high-frequency mass variations that alias into monthly gravity fields. The latest official product is AOD1B RL07 and describes non-tidal atmosphere and oceanic mass variations at 3-hourly resolution. However, the model-based de-aliasing products are inevitably incomplete and prone to temporally and spatially correlated errors that substantially contribute to errors in the estimated gravity fields. Here, we investigate possible enhancement of current de-aliasing products by nesting a regional high-resolution atmospheric reanalysis over Europe into a global reanalysis. As further novelty we include almost mass consistent terrestrial water storage variability from a regional hydrological model nested into a global model as additional component of the de-aliasing product. While we find in agreement with earlier studies only minor contributions from increasing the temporal resolution beyond 3-hourly data, our investigations suggest that contributions from continental hydrology and from regional non-hydrostatic atmospheric modeling to sub-monthly mass variations could be relevant already for gravity fields estimated from current gravity missions. Moreover, in the context of extreme events, we find regionally contributions from additional moisture fields, such as cloud liquid water, in the order of a few mm over Europe. We suggest this needs to be taken into account when preparing data analysis schemes for future space gravimetric missions.

Plain Language Summary

Observing temporal variations in the Earth's gravity field with satellite gravimetry plays an essential role for monitoring mass transports on and underneath the Earth's surface. This is crucial for understanding the evolution of floods and droughts, the role of groundwater pumping, and to quantify the melting of ice sheets and glaciers and the resulting sea level rise. In order to isolate the target variable (e.g., terrestrial water storage changes) unwanted signals (e.g., fast mass variations in the atmosphere) need to be removed in the gravity field estimation process using background models, so-called de-aliasing models. This paper focuses on improving background models by incorporating regional high-resolution models, which more specifically resolve certain processes in the atmosphere. Our hypothesis is that this will lead to better gravity fields with increased spatial resolution and less noise. Moreover, we find that considering fast hydrological variations as additional background model could improve gravity fields from the current satellite mission GRACE-FO. For the first time, we quantify contributions from so far neglected atmospheric moisture fields, such as cloud liquid water, to enhance background models in the context of extreme events – which, however, will likely be in particular relevant for more sensitive gravity missions in the future.

1 Introduction

The GRACE and GRACE Follow-On (GRACE-FO) satellite missions have provided unique data sets for studying the mass loss of the world's ice sheets and glaciers (Tapley et al., 2019; Wouters et al., 2019), variability and extremes in terrestrial water storage (TWS) (Kusche et al., 2016; Zhao et al., 2017; Gerdener et al., 2020; Han et al., 2021) and its long-term response to anthropogenic forcing (Rodell et al., 2018), and the mass-related component of sea level change (WCRP Global Sea Level Budget Group, 2018). However, the spatial resolution of the standard monthly GRACE/-FO data products is limited to about 300-400 km, which is insufficient for many potential applications (Pail et al., 2015; Wiese et al., 2022).

The biggest obstacle to improving the resolution of gravity fields with a single-pair satellite mission is, next to instrument noise, the temporal aliasing of high frequency mass variations due to the poor sampling geometry (Flechtner et al., 2016; Behzadpour et al., 2019). In the current GRACE/-FO processing (see, e.g. Dahle et al., 2019), the effect

of tidal and sub-monthly non-tidal mass variations in ocean and atmosphere is removed from level-1 data on the basis of model forecast simulations, so-called Atmosphere and Ocean De-aliasing (AOD) data (Dobslaw, Bergmann-Wolf, Dill, Poropat, Thomas, et al., 2017). Corresponding monthly mean AOD fields are provided to users in level-2 data (spherical harmonic coefficients) for optionally restoring them depending on the application (Uebbing et al., 2019). However, these AOD products are inevitably imperfect, and errors map into the GRACE/-FO level-2 data affecting science results even at longer timescales (Velicogna et al., 2001; Han et al., 2004; Boy & Chao, 2005; Wahr et al., 2006; Seo et al., 2008; Bonin & Chambers, 2011; Kvas, Behzadpour, et al., 2019b; Kvas & Mayer-Gürr, 2019; Zhou et al., 2023).

Candidate future gravity missions either as a successor of GRACE-FO, such as GRACE-C (envisaged from about 2027; Flechtner (2020)) and the Mass-Change and Geosciences International Constellation (MAGIC, from about 2031; according to Massotti et al. (2021)), or in the long run, concepts based on quantum technology (Rossi et al., 2023), seek to overcome the temporal aliasing problem partly by flying multiple satellite pairs, possibly some in inclined orbits. However, due to the still limited sampling even of multi-pair missions (Elsaka et al., 2014), contamination with unmodeled high frequency mass variations will likely become the single most dominant error source, after instrument technology improves. In addition, we speculate that mission targets will be set higher in temporal and spatial resolution, with higher demands in AOD modeling.

The biggest contribution to non-tidal sub-monthly time variability of the Earth's gravity field is actually due to atmospheric mass variations (Thompson et al., 2004). It should be mentioned here that in non-ocean applications of GRACE/-FO data, the atmospheric de-aliasing fields removed during gravity field processing are usually not restored to the estimated monthly gravity fields since one is interested in groundwater, snow or ice mass change, and atmospheric mass variations have never been part of the mission objectives.

The Earth's lower atmosphere mainly consists of dry air constituents, and of water in different states; i.e. water vapor, cloud water, rain water, cloud ice and snow. Modeling the atmosphere contribution to AOD entails that multi-level fields from numerical weather prediction (NWP) model runs are converted to 4D mass density, and then further to time series of spherical harmonic potential coefficients. This involves a 3D integration approach including various approximations (Swenson & Wahr, 2002; Boy & Chao, 2005). Many efforts have been made by previous studies to identify the effect of lateral and vertical discretization, quadrature and interpolation approaches, orography representation (Dobslaw, 2016), and the geometrical and physical approximations being applied in the georeferencing of pressure-level fields (Forootan et al., 2013; Yang et al., 2021) during the vertical integration (Table B2).

The latest release of the official AOD data, AOD1B (RL07; Shihora et al., 2022), makes use of European Centre for Medium-Range Weather Forecasts (ECMWF) ERA5 reanalysis data concatenated with ECMWF forecast (hereafter IFS) simulations. AOD coefficients are computed at 3-hourly resolution, and completed up to degree and order 180 using an ellipsoidal reference surface. The vertical integration procedures follows Dobslaw, Bergmann-Wolf, Dill, Poropat, and Flechtner (2017) and implements findings by Swenson and Wahr (2002) and Boy and Chao (2005), who demonstrated the importance of considering the vertical structure of the atmosphere in the de-aliasing approach (i.e., 3D vs 2D surface pressure method). Here, as to the best of our knowledge in all previous studies, only the dry air and the water vapor (i.e., specific humidity) fields are being used, while other (additional) moisture fields, i.e., rain water content, cloud water content, cloud ice content and snow content, are disregarded.

A number of studies (Forootan et al., 2013; Yang et al., 2021; Shihora et al., 2022) have compared the use of atmospheric fields from the IFS and the reanalyses ERA-Interim (ERA-I hereafter) and ERA5 for de-aliasing. The spatial resolution of ECMWF-IFS has

changed over time and is about 9 km since 2016, while ERA-I and ERA5 have a grid resolution of 79 km and 31 km, respectively. Dobslaw (2016) showed that mapping surface pressure grids from both the operational ECMWF model and ERA-I to a common reference orography allows to reduce relative biases and residual variability by about one order of magnitude, and achieves consistency at a level of about 1 hPa. Moreover, Dobslaw et al. (2016) derived pairwise RMS differences of band-passed surface pressure for periods of 10–30 days; for related ECMWF models they found differences of ∼0.2 hPa (equivalent to 2 mm change in water height), whereas comparisons to the Climate Forecast System Reanalysis (CFSR; Saha et al., 2010) and NASA's Modern Era Retrospective Analysis for Research and Applications (MERRA; Rienecker et al., 2011) reanalyses led to RMS differences of up to 0.7 hPa in Antarctica. One may conclude at this point that global atmospheric modeling has already, or will in the near-future, converge to an extent sufficient for AOD modeling.

Independent of the definition of the equipotential surface used for referencing the height coordinate, all current NWP models simulate the atmosphere with a spherical geopotential assumption (White et al., 2005). The shallow-atmosphere assumption is a geometric approximation that satisfies Lagrangian symmetries and thus conservation equations; its main advantage is that it allows a separation of the variables in the vertical and the horizontal direction (White et al., 2005). The hydrostatic approximation commonly employed in global atmospheric models further assumes that the vertical acceleration $D/Dt\dot{z} \approx 0$ is negligible. As a consequence, vertical changes in density are determined by temperature only, since pressure is constraint by the vertical velocity equation, which is reduced to $dp = -\rho g dz$. All models considered for AOD products so far have in common that their physics implementation makes use of the hydrostatic and shallow-atmsophere assumptions.

It is largely unknown how big the errors in temperature, surface pressure, and specific humidity and in the resulting AOD coefficients are, and to what extent they can be estimated from comparing model forecasts and reanalyses. It is further unclear to what extent such errors propagate through the GRACE/-FO level-2 processing and whether they can be partly mitigated by restoring monthly mean atmospheric mass fields, whether reliable error estimates can potentially be used in least-squares weighting procedures (Zenner et al., 2010), or in the assessment of future mission concepts (Dobslaw et al., 2015, 2016). Abrykosov et al. (2021) demonstrated additional benefit for gravity retrieval performance from incorporating ocean tide error covariance matrices. However, the additional benefit was found to be limited by the performance of the non-tidal atmospheric and oceanic components of the de-aliasing product, which stresses again the importance of improving these products.

Over the global ocean and at a wide range of frequencies, the sea surface reacts to pressure forcing in a way that is generally described as "inverse barometric effect" (Wunsch & Stammer, 1997). This means that the mass of an atmosphere-ocean column is conserved to first order. In the atmosphere-ocean de-aliasing procedure, an ocean model is forced by pressure and surface winds and thus provides a more realistic picture. However, it is clear that errors in atmospheric surface pressure are still to first order absorbed in the ocean response that is forced with the same atmosphere model. Since the focus of this contribution is not on providing an operational AOD product, we chose not to force an ocean model here and the evaluations in this study will, for the time being, refer to the atmosphere only.

Since atmospheric water mass redistribution occurs between water vapor, cloud liquid water and other constituents via phase changes, total mass can only be conserved if all mass-related model fields are consistently considered in the AOD computation, which is currently not the case. While the total mass fraction of moisture fields other than water vapor, i.e., the above defined "additional moisture fields", is thought to be smaller than 1 mm in equivalent water height (EWH) in the global average, we will show that

the sum of these fields may reach in localized extremes, e.g., in case of a thunderstorm, values larger than 5 mm EWH. For tropical storms we expect even larger values. This means, in the case of extremes the additional moisture fields can reach about the same magnitude as water vapor variability in regular conditions and, thus, become relevant not only for de-aliasing products but also when analyzing extremes based on TWS maps.

A somewhat related consistency problem then occurs when rain or snow hits the land surface and evapotranspiration adds to atmospheric water vapor. The mass flux across the land-atmosphere interface would need to be derived from coupled model components, if one were to confront GRACE/-FO or future gravimetric mission data consistently with a simulation of mass change in the full atmosphere and hydrological column. Such fully coupled models do not yet exist globally with a resolution sufficient for de-aliasing. Instead, in the present situation, TWS change is mostly derived from off-line hydrological models – while this is a best-practice approach if, e.g., precipitation data introduced as forcing data into these models is inconsistent with the atmospheric de-aliasing product, it should at least be noted that derived TWS change is not mass-consistent with the AOD procedures and also modeled evapotranspiration does not feedback into the atmosphere. We speculate that this again will lead to likely small but essentially unknown errors.

In order to explain the conundrum, let us follow the path of water in a thought experiment: If we imagine an area of strong local water vapor convergence, possibly driven by evapotranspiration over land, at some point cloud ice or liquid water may rapidly form and then lead to convective rainfall events. Such extreme weather events then often lead to catastrophic flooding. While a space gravimetric observable such as intersatellite tracking will track the entire, uninterrupted history of the resulting mass convergence in the atmosphere and later at the land surface, the conventional AOD procedure will remove a modeled large-scale water vapor field from these. As a result the de-aliased observations still contain a residual water vapor mass signal, the full cloud ice and liquid water signal, and of course the signature of the resulting rainfall in terms of land water storage change.

High-frequency mass redistribution of TWS, albeit occurring at longer timescales as compared to atmospheric mass variability, may cause additional temporal aliasing artefacts that are not taken into account when using the standard de-aliasing product AOD1B for estimating monthly GRACE fields. However, some studies (Zenner et al., 2014; Eicker & Springer, 2016; Ghobadi-Far et al., 2022) have suggested that removing sub-monthly hydrological mass redistribution prior to level-1 GRACE analysis may help in mitigating aliasing errors. This is also confirmed by, e.g., Kvas, Behzadpour, et al. (2019a) who considered terrestrial hydrology based on the Land and Surface Discharge Model (LSDM; Dill, 2008) as additional de-aliasing product and by Schindelegger et al. (2021) who used experimental (un-reduced, full-signal) daily GRACE solutions for de-aliasing in lieu of model simulations. In this paper we will revisit the question whether AOD and hydrological de-aliasing (called AOHD in the following) may be an asset for future de-aliasing products, while at the same time suggesting a way to maintain (as far as possible) mass consistency across the land-atmosphere interface.

With expanding HPC opportunities, global models move to even higher spatial resolution and non-hydrostatic computations become a necessity. Since it is unclear what this will mean for AOD computations, both in terms of required mathematical procedures and in terms of expected differences in mass variability compared to the conventional analyses, we decided to investigate the use of the non-hydrostatic, regional COSMO-REA6 atmospheric data set (Bollmeyer et al., 2015) for de-aliasing. COSMO-REA6 has been successfully validated in several studies, including its land-atmosphere water fluxes compared against GRACE and runoff data and global atmospheric reanalyses (Springer et al., 2017).

We used COSMO-REA6 atmospheric forcings to run the Community Land Model (CLM) version 3.5. This allows us to complement the COSMO-REA6 atmospheric mass variability with nearly mass-consistent hydrological storage variations, again, of course, limited to the European Coordinated Regional Climate Downscaling Experiment (EURO-CORDEX) domain. A caveat may be that the evaporative fluxes in COSMO-REA6 were not consistently derived from our own CLM run; yet we believe this provides a very good approximation to mass-consistent atmosphere (A) and hydrology (H) fields. For consistency, we use ERA-I for the remaining part of the atmosphere, and output from the WaterGAP Global Hydrology Model (WGHM; Müller Schmied et al., 2021) for the global hydrological component. We developed mathematical procedures for the re-gridding and nesting of global and regional data sets prior to spherical harmonics computation. The de-aliasing product AHD-UB generated in this study is available from Mielke et al. (2023).

To the best of our knowledge, this is the first investigation on the use of regional, non-hydrostatic atmospheric model data for mass de-aliasing, and it is also the first study that looks at mass-consistent hydrological de-aliasing. The methods that we describe here could be applied to other continental regions where high-resolution non-hydrostatic reanalyses exist already now (e.g., the North American Regional Reanalysis, NARR; Hunter et al., 2020). The same AOHD data could then be used for removing atmospheric and hydrological mass variability from other geodetic data where higher spatial resolution than for space gravimetry is required, e.g., in the case of terrestrial gravimetry or GNSS. To our knowledge, this is also the first study which explicitly separates the contribution of different atmospheric constituents, such as dry air and water vapor also including rain water, cloud water, cloud ice, and snow to total mass variability.

This paper is organized as follows: in the main part we provide results, discussion and possible future investigations. We focus on December 2007 for the results in the main part and we make additional figures available for February, June, and December 2007 in the supplementary material (SM). In the Appendix, we (i) introduce the applied models and data sets, (ii) provide a comprehensive summary of the vertical integration method applied in this study and in previous publications (Table B2) and (iii) explain the nesting of regional into global models.

2 Results

We investigate sub-monthly vertically integrated atmospheric and hydrological mass variations and discuss the contribution from: (i) increasing the temporal resolution of numerical models, (ii) applying regional high-resolution (and non-hydrostatic) models, (iii) considering additional atmospheric moisture fields with particular regard to extreme events, and (iv) taking into account continental hydrology.

For the atmospheric component we included two global and two regional NWP reanalyses in our study, the global ECMWF models ERA-Interim (ERA-I) and ERA5 that are part of the official AOD models (Dobslaw, Bergmann-Wolf, Dill, Poropat, Thomas, et al., 2017; Shihora et al., 2022), the Copernicus regional reanalysis for Europe (CERRA), and the Consortium for Small-scale Modeling reanalysis at 6 km resolution (COSMO-REA6), with the latter being the only non-hydrostatic model (Annex A1).

For the hydrological component we make use of the WaterGAP Global Hydrology Model (WGHM; Müller Schmied et al., 2021) and the regional high-resolution Community Land Model (CLM; Oleson et al., 2008) in version 3.5 (Annex A2). We integrated output from the NWP models vertically based on the ITG-3D approach (Forootan et al., 2013) as described in Annex B2 and nested regional into global models following Annex B4.

The first order mass consistent global atmosphere and hydrology de-aliasing data set with regional refinement over the EURO-CORDEX domain, the so-called AHD-UB

data set, is available from Mielke et al. (2023) for the year 2007. In this manuscript we show examples for December 2007; results for March, June, and September are provided in the supplementary material (SM).

In the following, we will (i) describe how atmospheric vertically integrated mass (VIM) changes when using different NWP models at different temporal and spatial resolution, (ii) discuss the magnitude of the individual wet atmosphere components, and (ii) assess contributions of continental hydrology to sub-monthly mass variability. Temporal variability of a specific data set, e.g., within one month, is provided as standard deviation computed with respect to the monthly mean. Differences of the temporal variability represented by the individual data sets are computed as root mean square deviation (RMSD).

2.1 Contribution of high-resolution atmospheric models

High-resolution regional models may provide improved VIM variations compared to global models due to their increased spatial and temporal resolution and by explicitly implementing non-hydrostatic dynamics. Both aspects lead to better resolved small-scale processes that potentially provide an asset for obtaining more realistic VIM estimates in particular in the case of localized extreme events.

As expected, we find that sub-monthly VIM varies within a range of 870 mm (SM Figure S4). The standard deviation of VIM with respect to the monthly mean reaches values between 10 and 250 mm in December 2007 (Figure 1). The mid-latitudes are characterized by strong baroclinic instabilities leading to mass fluctuations due to cyclone activity and by large-scale pressure variations such as the North Atlantic Oscillation.

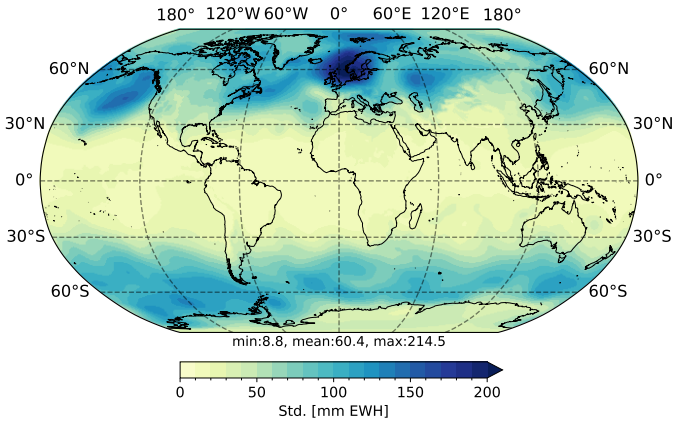

Figure 1. Standard deviation of ERA5-based sub-monthly vertically integrated atmospheric mass in December 2007.

The geometric height at the surface level, referred to as orography here, varies among individual NWP models and contributes to differences in VIM. The orography of each of the models is compared in Figure 2 over Europe. For ERA5 and ERA-I the orography was derived from the geopotential following the OFCM (Office of the Federal Coordinator for Meteorological Services and Supporting Research) conventions according to Forootan et al. (2013); see also Equation B7. For CERRA the geopotential heights were converted to orography, accordingly. As COSMO-REA6 is based on terrain-following coordinates (Doms, 2011), the geometric height is provided directly as surface orography.

The largest differences in orography are found in mountainous areas, where higher spatial resolution allows a more detailed representation of elevation differences. Comparing the global models, where orography is averaged over 31 km (ERA5) or 79 km (ERA-I), and the regional models with ∼6 km grid width (COSMO-REA6, CERRA), differences of several hundred meters are found in regions such as the Alps (Figure 2). For the two high-resolution models, we generally find smaller differences of tens of meters, although differences of several hundred meters are possible locally due to different grid conventions.

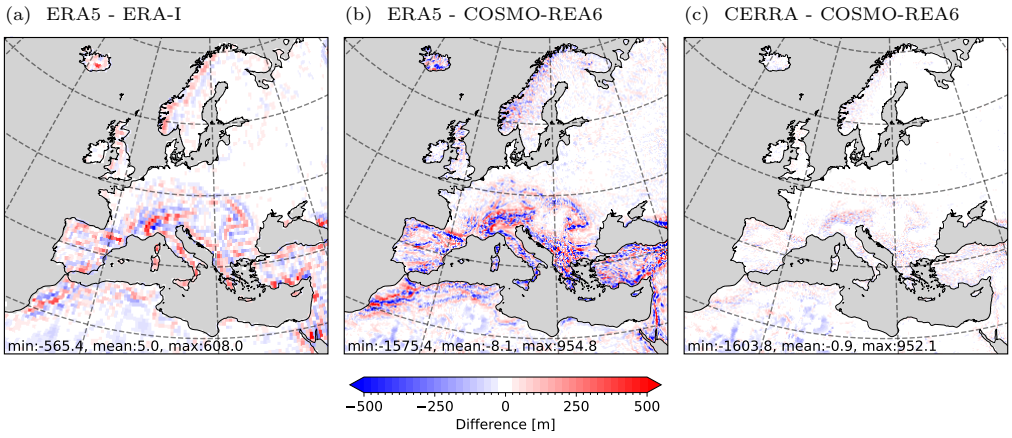

Figure 2. Differences in orography in meters over the EURO-CORDEX domain for selected models plotted on a 0.25° grid for the global models in (a) and on a linearly interpolated 0.1° grid in (b) and (c).

In 2017, with the RL06 product, the temporal resolution of the AOD1B product was increased from 6-hourly to 3-hourly sampling (Dobslaw, Bergmann-Wolf, Dill, Poropat, Thomas, et al., 2017). We computed the impact of the increased temporal resolution by first sampling to the coarser time intervals and then linearly interpolating to compare to the data set with the higher sampling frequency. After subtracting the respective monthly mean values, we calculated the root mean square deviation (RMSD) between the two data sets. Over Europe, Figure 3b shows differences in VIM variability of about 1 to 5 % (RMSD differences of 2 to 6 mm) when moving from 6-hourly to 3-hourly fields. Moving further from 3-hourly de-aliasing fields to 1-hourly fields captures additionally about 0 to 3 % (RMSD differences of 1 to 4 mm) of total sub-monthly variability (Figure 3c and SM Figure S5-S7). Generally, the change in VIM variability when moving from 6-hourly fields to 3-hourly fields is about twice as large as the effect when moving from 3-hourly to 1-hourly fields. This means, in terms of VIM variability, that the impact of switching from 3-hourly fields to 1-hourly fields is comparable to switching the version of the de-aliasing model from ERA-I to ERA5 (Figure 4). Over mountainous areas, differences in the overall variability are smaller due to smaller absolute values of VIM.

The change from ERA-I to ERA5 results in only small differences in larger-scale VIM patterns of about 5 mm (2 to 4 % of total sub-monthly variability, Figure 4a). Differences in VIM between the regional CERRA reanalysis and the global ERA5 reanalysis show small-scale differences of similar magnitude with larger differences possible in mountainous regions (Figure 4b) due to differences in orography. Interestingly, the differences in sub-monthly VIM variability between COSMO-REA6 and ERA5 models can be twice as large as those between CERRA and ERA5, or between ERA-I and ERA5. The differences between COSMO-REA6 and CERRA reach about the same magnitude as between COSMO-REA6 and ERA5. In this case, however, small-scale differences do

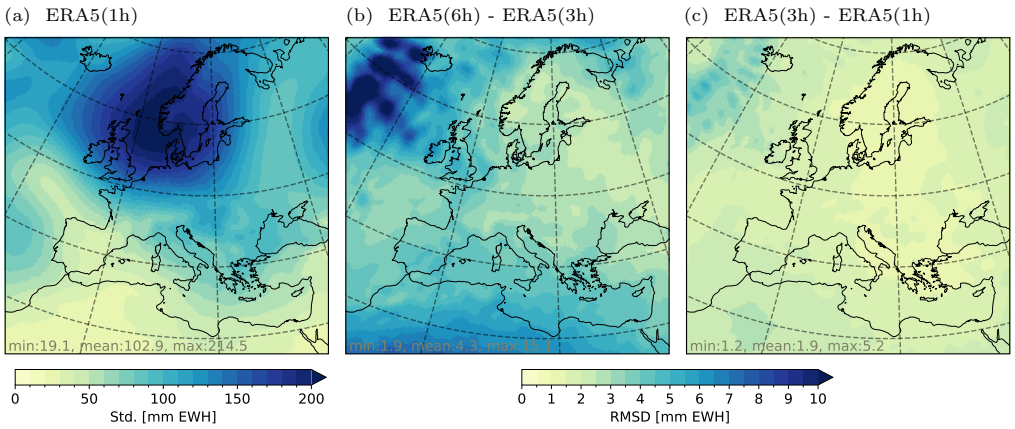

Figure 3. RMSD of sub-monthly atmospheric mass in December 2007 over the EURO-CORDEX region for (a) 1-hourly ERA5, (b) 6-hourly (linearly interpolated) ERA5 minus 3-hourly ERA5, and (c) 3-hourly (linearly interpolated) ERA5 minus 1-hourly ERA5. In order to compute differences between time series with different temporal resolution, the lower-resolution time series is linearly interpolated to the higher-resolution time steps.

not occur because the models have approximately the same spatial resolution. One reason for the differences in the VIM variability of COSMO-REA6 compared to the other models may be that COSMO-REA6 is the only non-hydrostatic model.

To take a closer look at the temporal evolution of the VIM of each model, we examined VIM averaged over five regions. Each of them covers about 280,000 km^2 (Figure 5), which roughly corresponds to the spatial footprint of the GRACE mission. The regions are over the North Sea on the British coast (A), over France (B), over the Alps (C), over the Mediterranean Sea on the east coast of Sicily (D), and over Turkey (E).

In general, sub-monthly VIM varies in December 2007 in a range of 600 mm EWH for footprint A (North Sea) with a significant increase after one third of the month (Figure 6). Indeed, a series of low pressure systems passed over Northern Germany and the North Sea in the first half of December, whereas the second half of December was characterized by stable high-pressure conditions. Differences between CERRA vs. ERA5 tend to be slightly smaller than differences between ERA-I vs. ERA5. Generally, differences between these models are below 10 mm EWH and they resemble random noise (see also SM Figure S11-S19). In contrast, the temporal evolution of VIM from COSMO-REA6 deviates more significantly and in a non-random, systematic way from the other models. This could be related to the fact that the local dynamics are better captured in COSMO-REA6 due to the higher model resolution and the non-hydrostatic formulation. In fact, over the North Sea, VIM from COSMO-REA6 differs by up to 20 mm from ERA5 (Figure 6b and SM Figure S11).

2.2 Contribution of wet atmosphere components

Water vapor content should not be neglected when calculating the VIM, as it can account for about 10 % of the total variability (Figure 7, second column). However, the contribution of moisture in the form of rain, cloud water, cloud ice, and snow to VIM variability has not been studied so far. To estimate their contribution, we compare VIM from COSMO-REA6 of (i) dry air components only VIM_{dry}, (ii) dry air including wa-

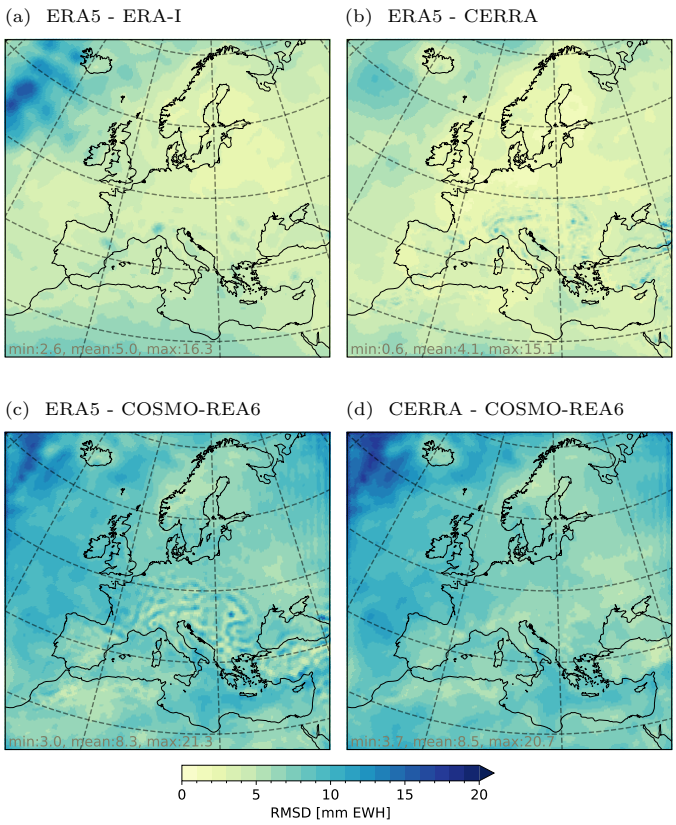

Figure 4. RMSD of vertically integrated atmospheric mass in December 2007 over the EURO-CORDEX domain between 3-hourly data from (a) ERA5 and ERA-I (interpolated from 6-hourly fields), (b) ERA5 and CERRA, (c) ERA5 and COSMO-REA6, and (d) CERRA and COSMO-REA6.

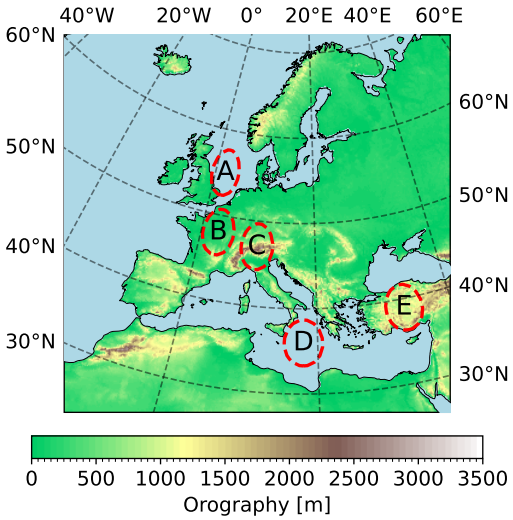

Figure 5. Orography of the COSMO-REA6 model and location of investigated GRACE footprints (A-E) over Europe with a radius of 300 km.

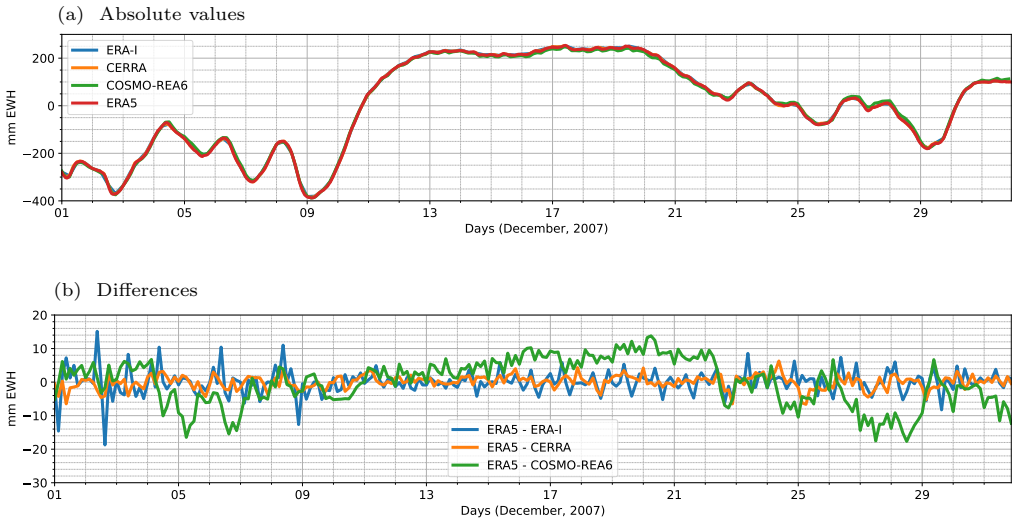

Figure 6. (a) Area-averaged sub-monthly vertically integrated atmospheric mass of all models within footprint A (North Sea at the British coast) and (b) the respective differences in comparison to ERA5 in December 2007.

ter vapor VIM_{hum}, and (iii) moist air including rainwater, cloud water, cloud ice, and snow VIM_{wet} additionally to VIM_{hum}.

As expected, the contribution of the additional moisture fields (<1 mm with respect to the RMSD) is small compared to that of water vapor (Figure 7a-c). However, during extreme events, the VIM variability due to the additional moisture fields can locally reach values of several mm EWH, accounting for up to 2 % of the variability of the total VIM_{wet} (Figure 7d-f). As an example we show daily RMSD computations of VIM on 5 December 2007 when heavy rainfall lead to flooding over Cyprus and Turkey (Figure 7d-f). The signature of the additional moisture fields is clearly visible for the specific day with a magnitude of about 3 mm in terms of RMSD.

Other examples are a heavy precipitation event that occurred in the Mediterranean Sea near Sicily on 4 June (SM Figure S20f); and an extreme event in the East of Great Britain on 25 June (SM Figure S20l). Particularly interesting is also the situation of the period between 19-23 December 2007, when heavy thunderstorms with supercells and hail struck Germany (Hechler & Bissolli, 2011). Figure S20i in SM shows contributions of additional moisture fields to VIM variations over large parts of Germany with a magnitude of up to 5.9 mm.

We show the impact of additional moisture fields in more detail for individual footprints over Europe. The contribution from water vapor to VIM variability reaches values of about 7 mm over Turkey (Figure 7g), and exceeds 15 mm in the first half of December 2007 over France (Figure S23b). In the case of the extreme event over Turkey the contribution of the additional moisture fields to VIM, which is not taken into account in the official AOD products, reaches 2 mm, i.e., 30 % of the contribution from water vapor.

2.3 Contribution of continental hydrology

Unlike water vapor variability, short-term water storage changes at the land surface and the sub-surface are not considered as part of the standard AOD de-aliasing. Figure 8a shows sub-monthly variability of TWS globally based on output of the global hy-

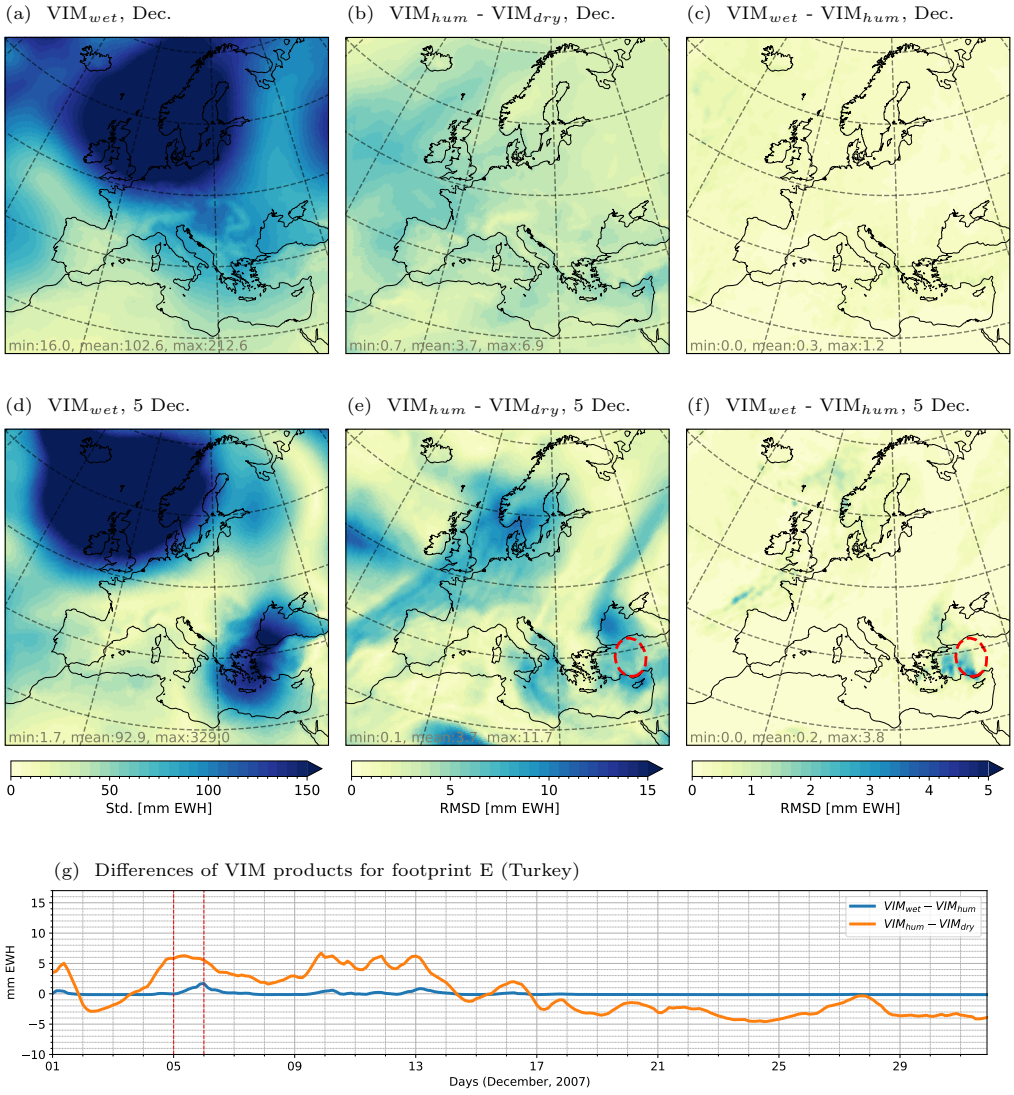

Figure 7. VIM based on (i) only dry air density variations (VIM$_{dry}$), (ii) dry air density and water vapor (VIM$_{hum}$), and (iii) dry air, water vapor including rain, cloud water, cloud ice and snow (VIM$_{wet}$). First row shows (a) standard deviation of VIM$_{wet}$, and the RMSD for (b) VIM$_{hum}$ versus VIM$_{dry}$, and (c) VIM$_{wet}$ versus VIM$_{hum}$ for the entire December 2007. The second row shows standard deviation and RMSD for 5 December 2007. Exemplarily, (g) shows VIM differences for footprint E over Turkey (red dashed circle) in (e) and (f). Differences between VIM$_{hum}$ and VIM$_{dry}$ are in orange, and between VIM$_{wet}$ and VIM$_{hum}$ in blue.

drological WGHM model for December 2007. The standard deviation of submonthly variability of TWS reaches values larger than 50 mm, and it is particularly high in equatorial regions. Most significant variations are observed over the Amazon, the Ganges Delta, and the Saint Elias Mountains (North America). Over Europe, sub-monthly TWS variability varies regionally and the model suggests a magnitude between 5 and 30 mm. During the month of June particularly high variations arose over the Scandinavian Mountains with a standard deviation of around 100 mm EWH likely due to snow variability (SM Figure S25). In general, the sub-monthly TWS variability from the regional high-resolution model CLM (Figure 8b) shows more pronounced local features and larger RMSD values than WGHM. Over Europe, differences between sub-monthly TWS variability from the global model WGHM and the regional model CLM can be as large as total sub-monthly TWS variability (Figure 8c). We suspect that the way how WGHM disaggregates meteorological forcing data within the month is partly responsible for this.

Sub-monthly variability of TWS is characterized by linear evolution over several days over Europe (Figure 8d). In December 2007 strong rainfalls occurred in large parts of Europe leading to an increase in TWS. The storm event of 2 December 2007 is clearly visible for the footprints over France and over the Alps (SM Figure S30). The two models, WGHM and CLM, show generally the same patterns with a slightly larger range of variability for CLM. In the Alpine region small ($\sim$ 1 mm) sub-daily variations of TWS are visible in the CLM model (SM Figure S30). For extreme events, terrestrial water storage anomalies (TWSA) simulated by CLM show immediate responses with steep TWSA curves, whereas WGHM simulates a smoother change in TWSA.

3 Discussion

Future satellite gravity missions are expected to provide gravity fields and mass change maps with higher resolution as compared to GRACE and GRACE-FO. However, we will achieve substantial progress only if de-aliasing models can be improved. We suggest that it is time to reconsider, besides the tidal and non-tidal ocean components, also the atmosphere contribution. Recent improvements on the atmospheric part of the AOD product included (i) homogenizing surface pressure time-series from different NWP models to a common reference orography, (ii) moving from ERA-I to ERA5, (iii) moving from 6-hourly resolution to 3-hourly resolution or even 1-hourly resolution, and (iv) updating geometric, physical, and numerical approximations. Forootan et al. (2013) and Yang et al. (2021) showed that a more realistic geometrical and physical shape of the Earth, together with better approximation of latitude- and altitude-dependent gravity acceleration in the vertical integration process, leads to differences in VIM of few 0.01 mm in terms of geoid height without degree 0 and 1 coefficients, i.e. less than 1 mm EWH. With AOD-RL06 the temporal resolution of the de-aliasing product was increased from 6-hourly data to 3-hourly data, which lead to differences in the geoid of about 0.1 mm averaged over one year (Yang et al., 2021), i.e. few mm EWH. Further increasing the temporal resolution to 1-hourly fields was assessed by Shihora et al. (2022) and Yang et al. (2021). Yang et al. (2021) quantified the impact on the geoid to about 0.04 mm over Europe and up to 0.08 mm in equatorial regions again averaged over one year. In line with this, Shihora et al. (2022) suggested that the differences between hourly data and hourly fields interpolated from 3-hourly fields are negligible for current applications. The impact of changing the NWP model from ERA-I to ERA5 was found to alter geoid height variability by about 0.1 to 0.3 mm, which corresponds to 1 to 5 mm EWH (Yang et al., 2021). For long-term consistency of the official de-aliasing product, Dobslaw (2016) mapped the global reanalysis and analysis fields to a common reference orography, thus achieving consistency of residual variability of surface pressure at the level of 10 mm. The implication is that the atmospheric component of the official AOD-RL07 product is well tailored for current gravity missions, while for future missions with significantly more demanding requirements, steps towards an even higher temporal resolution and better long-term consistency will become necessary.

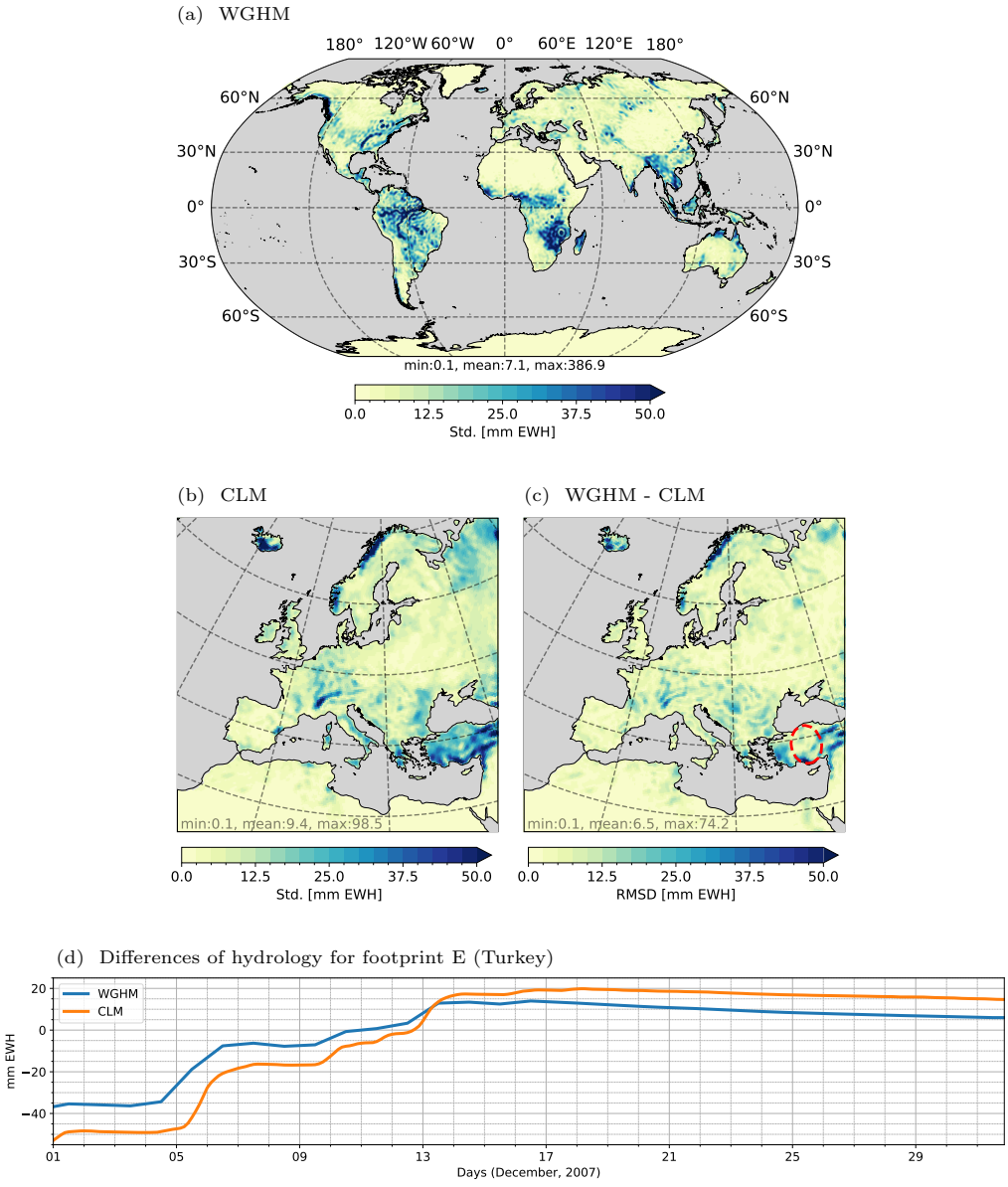

Figure 8. Standard deviation of sub-monthly variability of (a) WGHM- and (b) CLM-based water mass in December 2007. (c) RMSD between both models. (d) Sub-monthly terrestrial water mass variations of WGHM (blue) and CLM (orange) models for footprint E in December 2007.

All previous studies relied on global NWP models which are currently only available at limited spatial resolution (>30 km), and they are all based on the hydrostatic assumption. In this paper, we investigated the use of regional high-resolution NWP model output for future de-aliasing products, including also the non-hydrostatic model COSMO-REA6 for the European CORDEX region. Moreover, we analyzed contributions from currently neglected additional atmospheric moisture fields and the terrestrial hydrology to high-frequency mass variability. We interpret our results also in the context of future gravity missions.

Over Europe, moving from 6-hourly to 3-hourly adds variability in the order of 3 to 10 mm EWH to VIM, whereas the effect of moving from 3-hourly to 1-hourly fields is half as large and usually smaller than 5 mm (Figure 3). More specifically, averaged over the study domain, VIM variability computed from ERA5 data increased by 4 mm EWH for 6-hourly vs 3-hourly data, and by 1.6 mm EWH for 3-hourly versus 1-hourly data. For COSMO-REA6 increased temporal resolution has the same effect like for ERA5 in terms of magnitude of surface pressure variability, which means that better resolving small-scale processes within a regional model does not necessarily capture more variability at shorter time scales. Yet, for ground-based applications like GNSS or terrestrial gravimetry a product with higher spatial and temporal resolution is an interesting option for vertical loading corrections. It should be kept in mind, that atmospheric tides were not removed here. However, their impact can be assumed to be not significant for our analysis in the mid-latitudes (Yang et al., 2021).

Shihora et al. (2022) found, after careful removal of tidal signals, contribution of hourly temporal resolution versus 3-hourly resolution of about 5 mm and decided based on that analysis to keep the official AOD product at 3-hourly resolution. Likewise, Yang et al. (2021) computed the impact from higher temporal resolution to reach values of about 0.2 mm geoid height (which corresponds to about 5 mm EWH) and suggested to test them as AOD product in the gravity field processing chain. Indeed, the impact from increasing the temporal resolution from 3-hourly fields to 1-hourly fields on VIM is as large as the impact from updating the NWP model version from ERA-I to ERA5, and about 10 times as large as the impact from the refined vertical integration approach suggested by Yang et al. (2021).

Recently, the MAGIC mission was decided to be launched as a successor of GRACE-FO. Monthly fields are expected to possibly have an accuracy of 10 mm EWH (GRACE-FO 20 mm) at 300 km spatial scale (Heller-Kaikov et al., 2023; Wiese et al., 2022). Future quantum gravimetry missions aim at providing monthly fields with an accuracy smaller than 10 mm EWH and daily fields with an accuracy of few centimeters. Given these numbers, for future gravity remote sensing application we suggest to transition to 1-hourly AOD products.

Will it be possible to improve computations of vertically integrated atmospheric mass through the use of high-resolution models, which are currently available only as regional (limited-area) configurations? We find that differences between VIM from ERA-I, ERA5 and CERRA are all in the same range with mean RMSD values averaged over the EURO-CORDEX area between 3 to 7 mm for the individual months. These differences may arise from (i) differences in the forecast model applied by the NWP models, (ii) assimilation of differently processed or new observation data sets, and (iii) different spatial resolution and, thus, distinct parameterization schemes of smaller scale processes. In contrast, the VIM variability from COSMO-REA6 differs noticeably from the other models, with RMSD values that can be more than twice as large compared to those from the other model comparisons. Our sensitivity studies show that this is not due to higher spatial resolution or the consideration of the additional moisture fields. Indeed, we assume that the larger differences can be explained by non-hydrostatic contributions from the COSMO-REA6 model. Of course, minor differences may also arise due to different choice of the orography. Bollmeyer et al. (2015) validated integrated water vapor from

different models against GPS observations over Germany, and found smaller biases for COSMO-REA6 in comparison to ERA-I. At this stage, however, we can only conclude that a de-aliasing product applying COSMO-REA6 over Europe will differ significantly from current products, at a scale comparable to the transition from AOD1B-RL05 to AOD1B-RL06. It is an open question whether this will lead to better estimation of monthly gravity fields already for GRACE and GRACE-FO missions and needs to be assessed in future. To address this issue, Yang et al. (2018) evaluated different de-aliasing products via computing level-1B pre-fit range-rate residuals. To be more precise, they investigated how well measured range-rates and range-rates modeled based on different AOD products fit together, and they found significant improvement of the atmospheric part of RL06 in comparison to RL05. As our product includes a refinement only over Europe, we expect only minor impact on global gravity field estimation.

The impact of extreme events on GRACE observations has been investigated solely looking at the contribution of hydrology in terms of TWS changes, either by analyzing estimated sub-monthly gravity fields (Save et al., 2016; Nie et al., 2023; Zhang et al., 2023) or by studying range-rate observations (Li et al., 2023; Han et al., 2021; Ghobadi-Far et al., 2022). In this paper, we moved a step further and investigated water mass anomalies that occur during extreme events before, in the form of precipitation, atmospheric water flux increases hydrological storage. In other words, we seek to track the fate of water during its entire travel through the atmosphere-land continuum. In more detail, we analyzed the contribution of atmospheric moisture fields that are currently disregarded in AOD modeling (rain water, cloud water, cloud ice and snow) to VIM in the context of extreme events. We found that locally these additional fields can reach values of few mm EWH over Europe, which amounts to about 2 % of total sub-monthly variability and up to 30 % of the contribution from water vapor. We speculate that for the catastrophic July 2021 event that led to widespread flooding over Western Germany, these values were exceeded by far. On small spatial scales the impact from additional moisture fields is comparable to the impact of switching, e.g., from ERA-I to ERA5 over continental areas. As we restricted our analysis to the EURO-CORDEX area, we cannot address the question here which magnitude the impact of this kind of events can reach over the oceans during hurricane season, and over land in tropical cyclone regions. Future studies are required to understand whether such localized strong events indeed map into monthly gravity field estimates.

Only few studies investigated the impact of sub-monthly hydrological variability on GRACE range-rate observations (Zenner et al., 2014; Eicker & Springer, 2016; Ghobadi-Far et al., 2022) or on monthly GRACE fields (Thompson et al., 2004). Indeed, Eicker and Springer (2016) showed that taking sub-monthly hydrological variability into account reduces K-band range rate residuals, i.e. the fit of modeled range-rates to measured range-rates, in particular in equatorial regions where substantial water mass changes at short time scales occur. At the time of the study conducted by Thompson et al. (2004) hydrological models did not provide reasonable short-term variability and, thus, did not improve monthly gravity field estimation. Ten years later, Luthcke et al. (2013) found that GRACE Mascon solutions improved when taking into account continental hydrology based on output from the GLDAS-NOAH model (Ek et al., 2003; Rodell et al., 2004). Kvas, Behzadpour, et al. (2019a) applied submonthly TWSA from the global Land Surface Discharge Model (LSDM; Dill, 2008) as additional de-aliasing product. However, global hydrological models usually focus on climate change and water resource assessments but not on flood forecasting, and as a consequence processes that can lead to fast-moving water transports are not well represented; also these models sometimes lack a suitable temporal resolution of the meteorological forcing data.

In our study, we compared high-frequency hydrological mass variations based on the output of two different hydrological models, the global model WGHM and the regional high-resolution model CLM3.5, which was forced with COSMO-REA6 data. As expected, sub-monthly TWS variability over Europe was found twice as large for CLM

(≈ 10 mm) compared to WGHM (≈ 5 mm over Europe), although large-scale patterns of TWS evolution agree for the two models. To some extent the higher variability of CLM3.5 can be explained by the higher temporal and spatial resolution and more hydrological processes being represented physically – some of differences will be averaged out at satellite height. Dobslaw et al. (2015) found high frequency variability of hydrological signals of about 5 mm in Europe and of about 15 mm in regions near to the equator, and isolated single events with fast water mass changes of few centimeters based on the LSDM model.

Although the contribution from continental hydrology to sub-monthly mass variations is about one magnitude smaller as compared to the atmospheric mass variability, we find that including hydrological variablity into total mass variability would lead to similar changes like increasing the temporal resolution from 6-hourly data to 3-hourly data for the atmospheric model, or changing the model version from ERA-I to ERA5 (but obviously only over the continents). In this light, the potential for improving the standard de-aliasing product by including sub-monthly hydrology should be assessed carefully in particular for future missions. However, two important obstacles will arise here: (i) current global hydrological models lack resolution and exhibit large uncertainties and we showed in this paper that differences can be almost as large as the signal while few, if any, high-resolution data sets exist at global scale. Alternatively, daily GRACE solutions could be assessed as additional de-aliasing product that accounts for hydrological mass variability; however, such solutions inevitably lack the spatial resolution required to resolve local strong events of significant size. (ii) We will have to avoid double bookkeeping of water masses that transition from the atmosphere to the land surface and to some part back into the atmosphere, involving phase changes. This can be achieved correctly only by using a fully coupled atmosphere-hydrology model. In this paper, we ensure consistency to first order over Europe by using output from the applied atmospheric model as forcings for the hydrological model.

In summary, from the experiments covered in this study, we can conclude that the impact on sub-monthly mass variability over Europe from (i) wet atmosphere contributions, (ii) updating hydrostatic model versions, (iii) increasing the temporal resolution of the NWP model from 6-hourly fields to 3-hourly fields, and (iv) adding TWS variations modeled by a global hydrological model are of about the same size. We find that the impact from using a non-hydrostatic NWP model and a regional hydrological model are considerably larger. Impacts from increasing the temporal resolution of the NWP model from 3-hourly fields to 1-hourly are smaller, and only very limited impact arises from considering additional moisture fields over Europe – which might be different for equatorial regions. One major asset of our regional refinement is a first order mass consistency across atmosphere and land surface. Due to the altitude of the satellites, further increasing the spatial resolution of NWP and hydrological models may likely not directly improve the de-aliasing process, but we suggest that it will indirectly lead to a better representation of local processes. In contrast to previous studies, which assessed anomalies with respect to a long-term mean, we assessed sub-monthly variability here. Thus, when comparing to previous results, one should keep in mind that the RMSD values we compute here are most likely slightly smaller.

For current satellite gravimetry missions, where de-aliasing includes already wet atmosphere contributions, a recent NWP model, and 3-hourly fields, at least the impact of hydrology on estimated gravity fields should be assessed carefully. For future more sensitive satellite missions also 1-hourly fields might become important. Contributions from moisture fields other than water vapor, i.e., rain water, cloud water, cloud ice and snow, might not only map into estimated monthly gravity fields in the case of extreme events, but are relevant also for other applications, such as loading computations for GNSS studies, in particular if one is interested in cyclones (Zhan et al., 2021). We suggest that these contributions will also be relevant if one aims at studying the evolution of extreme

precipitation, surface runoff and resulting flooding in integrative studies including space gravimetry data.

4 Outlook

We suggest that high-resolution de-aliasing data sets from refined atmospheric models, such as provided in this study, should be assessed at the level of K-band and laser ranging interferometry observations, both in view of improving the accuracy of monthly gravity field model estimates and the "direct" evaluation of level-1 data for mass transport monitoring. Particularly interesting will be a systematic impact assessment of the different contributions to mass variability shown in this contribution in the context of gravity field estimation. In future, we plan to include newly available reanalysis products, e.g., the new version of COSMO-REA6, and analysis with the Icosahedral Nonhydrostatic (ICON) model. A consistent global atmospheric data set will then be complemented by ERA5 outside of Europe. As long as no high-resolution non-hydrostatic global NWP reanalysis exists, another option will be to nest multiple regional NWP products simultaneously into one global model. Currently available regional high-resolution reanalyses focus on the Northern hemisphere and include the North American Regional Reanalysis (NARR; Hunter et al., 2020) and the East Asia Reanalysis System (EARS; Yin et al., 2023). Yet, we first need to understand if high-resolution non-hydrostatic models indeed represent more realistic mass variability.

Regarding future enhanced de-aliasing products, we recommend that the contribution of additional atmospheric moisture fields, i.e., cloud water, rain water, cloud ice and snow, should be investigated globally and possibly be included in the product. With respect to sub-monthly TWS variability we need to further investigate how output from different hydrological products influence the estimated gravity fields and which model is favorable and guarantees near real-time availability. Furthermore, we argue that in order to maintain mass consistency, improvements in Earth System Models (ESMs), which provide fully coupled representation of water fluxes, will be of major interest for a consistent dealasing product. For instance, for ERA7 enhanced coupling with the land data assimilation system is expected, which will provide new perspectives for de-aliasing and/or signal separation.

We envision two different strategies evolving: On the one hand, given that we now know very well that fast hydrological signals should be removed during de-aliasing, one could argue that signals in all compartments that can be modeled with reasonable confidence should be removed. This could lead to a situation where the gravity missions would "only" provide corrections to mass changes derived from compartmental models of some advanced ESM, with the challenge of separating observations into hydrology, ocean, and further contributions. On the other hand one could argue that model simulations and data assimilation are better at separating the data; in this situation one might assimilate space gravimetric observations directly into a coupled ESM - the challenge here might be that probably few coupled assimilation approaches could handle gravimetric data now.

Our study was constrained to the EURO-CORDEX domain. However, in particular continental hydrology and contributions from additional moisture fields are much larger in other regions. This means, a detailed analysis of these contributions, i.e. rain water, cloud water, cloud ice and snow, on a global scale would be interesting. In future, the sensitivity of gravity missions might also become interesting for improving NWP models, e.g., via data assimilation. Another future implication is – whether a future gravity mission, e.g., with standard daily gravity field products and spatial resolution as today or better, would consider either dry air mass or water vapor as target variables – this entails that we would need to derive model-free estimates of these from the space-gravimetric data; this appears challenging but may be facilitated via separating the dominating time-scales.

Other geodetic techniques that require the removal or consideration of time variable gravity effects due to atmospheric mass variations are terrestrial gravimetry (Neumeyer et al., 2004) and precise orbit determination (Cerri et al., 2010). Moreover, for GNSS and satellite altimetry it is required to derive vertical loading corrections due to atmospheric pressure (Mémin et al., 2020; König et al., 2021) and to model the dynamic response of the sea surface (Andersen et al., 2018). While in particular for station observables the requirements on spatial resolution may be much higher in the "near-zone", it is clear that consistency across all geodetic techniques would be a welcome goal.

Appendix A Data

A1 Atmospheric reanalyses

NWP models represent various physical processes in the atmosphere and at the ocean and land surface, on complex topography, and propagate their impact on the temporal evolution of pressure, temperature, wind, water vapor fields and clouds and precipitation via some simplified form of the Navier-Stokes equations. Many processes like cloud formation cannot be explicitly resolved and their impact is approximated via parameterization schemes.

The global reanalysis ERA-I and its successor ERA5 were developed by the European Centre for Medium-Range Weather Forecasts (ECMWF) and provide global atmospheric variables at multi-level fields. Compared to ERA-I, ERA5 has a higher horizontal grid resolution of 31 km (ERA-I: 79 km) and considers 137 pressure levels (ERA-I: 60 levels). The output frequency increased from 6-hourly data to 1-hourly data. Furthermore, the land surface model, i.e. the Tiled ECMWF Scheme for Surface Exchanges over Land (TESSEL), was updated to HTESSEL, which incorporates an improved formulation of soil hydraulic properties and more realistic surface runoff generation. Major improvements of ERA5 with respect to ERA-I are related to the number and handling of observations; ERA5 incorporated more comprehensive satellites observations and applied a new data-assimilation system. Additionally, ERA5 provides a 3-hourly uncertainty estimate for each parameter from a low-resolution 10-members ensemble, which was not available for ERA-I. The improved resolution, wider vertical coverage, and enhanced sampling of ERA5 enable a better representation of atmospheric patterns compared with previous global reanalyses, and show a considerable improvement especially in the troposphere with respect to ERA-I (Hoffmann et al., 2019; Hersbach et al., 2020).

Two high-resolution regional atmospheric reanalysis data sets are used in this study, namely the COSMO-REA6 and CERRA reanalyses. COSMO-REA6 (Bollmeyer et al., 2015) is based on the non-hydrostatic Consortium for Small-scale Modeling (COSMO) model (Doms, 2011). COSMO-REA6 applies a continuous nudging scheme (Schraff & Hess, 2003) to assimilate meteorological observations from radiosondes, aircraft and weather stations; the lateral boundary is constrained by ERA-I. The model grid of COSMO-REA6 is composed by an approximately 6 km staggered Arakawa-C horizontal grid and the terrain-following Gal-Chen hybrid height-based vertical coordinates with layer thickness increasing with altitude up to 22700 m corresponding to 40 hPa (Gal-Chen & Somerville, 1975; Arakawa & Lamb, 1981; Bollmeyer et al., 2015). The terrain-following coordinate system reduces the complexity of formulating lower boundary conditions when surface terrain is involved, where the lowest surface of constant vertical coordinate becomes conformal to the orography (Doms, 2011). Topography set-up for COSMO-REA6 is taken from Global Land One-kilometer Base Elevation (GLOBE ; Hastings & Dunbar, 1999; Asensio et al., 2020) topography.

The Copernicus European Regional ReAnalysis (CERRA) (Schimanke et al., 2021) is a collaborative effort led by the Swedish Meteorological and Hydrological Institute in cooperation with the Norwegian Meteorological Institute and Météo-France. In contrast to the non-hydrostatic, fully compressible hydro-thermodynamic of COSMO-REA6, CERRA

adheres to the hydrostatic assumption in line with global climate models. CERRA is based on the HARMONIE-ALADIN data assimilation system (Bengtsson et al., 2017; Termonia et al., 2018), includes the 3DVar deterministic CERRA reanalysis (CERRA-EDA) with 10 ensemble members for the upper air, and a surface reanalysis CERRA-LAND, which combines CERRA forcast fields and additional surface observation using an optimal interpolation algorithm. Compared to COSMO-REA6, more observations are assimilated into CERRA such as satellite radiance observations and other non-conventional observations, and the up-to-date ERA5 is applied for boundary conditions. The horizontal resolution of CERRA is 5.5 km (11 km for CERRA-EDA), the spatial domain covers entire Europe and surrounding seas, and vertically extends up to 1 hPa height with 106 levels (El-Said et al., 2021; Z. Q. Wang & Randriamampianina, 2021). For this study, we collected surface pressure, orography, air temperature, and specific humidity profiles from both regional reanalysis. Additional moist air contents including specific rain water content and specific cloud water/ice content from COSMO-REA6 were extracted. CERRA provides comparable variables but were not included in this study, because these variables were only available for forecast runs.

A2 Hydrological models

The global water resources and use model WaterGAP v2.2d (Müller Schmied et al., 2021) simulates daily water flows between all continental water storage compartments except glaciers at a 0.5° grid. The model is calibrated against mean annual river discharge of more than thousand gauging stations, located at the outlet of the respective drainage catchments. Human water abstraction from groundwater aquifers and surface water bodies and return flows are modeled by a linked groundwater and surface water use model (Döll et al., 2012, 2014). Climate forcings at daily resolution are obtained from WFDEI (WATCH Forcing Data methodology applied to ERA-Interim data; Weedon et al., 2014). In this study, we use daily TWS estimates that include canopy, snow, soil, groundwater, lakes, man-made reservoirs, wetlands and rivers.

Over Europe, we use TWS outputs from the Community Land Model version 3.5 (CLM3.5; Oleson et al., 2008) to increase the temporal and spatial resolution of our hydrological de-aliasing model in this region. CLM3.5 is a land-surface model that consists of multiple modules representing biogeophysical and biogeochemical processes, dynamic vegetation composition and structure, plant phenology, and the hydrological cycle. We run this model over the European COordinated Regional Downscaling EXperiment (CORDEX) area at 0.11° (∼12.5 km) resolution with hourly time steps. The model is forced with COSMO-REA6 6-hourly meteorological data (see Springer et al. (2019) for details on the set up). TWS estimates are aggregated over soil water and soil ice at different levels, snow water, canopy water, and water in the unconfined aquifer with hourly output intervals.

Appendix B Methods

B1 Water mass consistency across COSMO-REA6 and CLM

To obtain consistent atmospheric-hydrologic mass variations over Europe for the de-aliasing product, we use COSMO-REA6 to drive the CLM3.5 land surface model. Therefore, water masses in the hydrological model are consistent with atmospheric precipitation. However, the feedback from the land surface to the atmosphere is not yet consistent because evaporation in COSMO-REA6 differs from evaporation in our CLM3.5 run. We believe this is a second order effect, as evaporation fluxes generally evolve much more regularly than precipitation.

A substantial part of the sub-daily variability in atmospheric mass variability is due to solar forcing and thus corresponds to S_1, S_2 tides (solar or thermal tides). It is well-known that 6h fields do not permit an adequate resolution of the S_2 tide (Ray & Ponte,

2003), and therefore it is generally recommended to remove S_1 and S_2 signals from the atmospheric mass grids. Recent studies even consider minor tides (Yang et al., 2021; Shihora et al., 2022). However, the focus of this paper is on the influence of atmospheric processes and their representation in models, and so we refrain from computing and removing a dedicated solar tide model from each of the different cases. Instead, we propose that, for example, the tide model in Shihora et al. (2022) is simply removed consistently across different cases.

Below, we explain (i) how output from hydrostatic and non-hydrostatic atmospheric models is integrated to compute VIM, (ii) how VIM was computed in previous studies including the approach applied for the official atmospheric de-aliasing product RL07 and (iii) how regional and global atmospheric and hydrological models are nested together using a tapering approach.

B2 Vertical integration

Spatiotemporal mass variations for de-aliasing products are represented by sets of spherical harmonic coefficients $\Delta C_n^m(t)$ and $\Delta S_n^m(t)$ (Stokes coefficients) up to degree n and order m (Hofmann-Wellenhof & Moritz, 2006; Boy & Chao, 2005):

$$\left.\begin{array}{c}\Delta C_n^m(t)\\ \Delta S_n^m(t)\end{array}\right\} = \frac{(1+k_n')a^2}{(2n+1)M_e}\int_0^{2\pi}\int_0^{\pi}\Delta I_n(\theta,\lambda,t)\tilde{P}_{nm}(\cos\theta)\left\{\begin{array}{c}\cos(m\lambda)\\ \sin(m\lambda)\end{array}\right\}\sin\theta d\theta d\lambda, \quad \text{(B1)}$$

where (θ,λ) denote co-latitude and longitude of a given point in spherical coordinates, $\tilde{P}_{nm}$ are normalized associated Legendre Functions, M_e is the average mass of the Earth, a is a scaling factor that is typically chosen as the semi-major axis of the reference ellipsoid (here the WGS84), and k_n' are the load Love numbers (Farrell, 1972; Dong et al., 1996). The factor $1+k_n'$ takes into account indirect elastic loading effects, additionally to direct gravity effects due to mass changes. The vertical degree-dependent so-called "inner integral" ΔI_n represents the changes over all masses in the Earth system in radial direction

$$\begin{aligned}\Delta I_n(\theta,\lambda,t) &= \left(\int_0^{\infty}\left(\frac{r}{a}\right)^{(n+2)}\rho(\theta,\lambda,r,t)dr\right) - \overline{I_n}(\theta,\lambda)\\ &= I_n(\theta,\lambda,t) - \overline{I_n}(\theta,\lambda),\end{aligned} \quad \text{(B2)}$$

where r is the geometric distance to the Earth's center of mass, $\rho(\theta,\lambda,r,t)$ are time variable density anomalies at a certain radius r, and $\overline{I_n}(\theta,\lambda)$ represents the monthly mean of VIM. As water storage variations occur within a thin layer (10-15 km) at the Earth's surface, the inner integral is reduced to representing changes in surface density, which then simplifies Equation B1 to a simple surface integral when we apply it to hydrological model output (Wahr et al., 1998).

In the case of the atmosphere, Boy and Chao (2005) showed that the impact from 3-D mass redistribution is non-negligible. Thus, for current AOD products the full contribution of atmospheric mass distribution is computed, including surface pressure effects and contributions of density anomalies above ground. For global atmospheric models and the CERRA reanalysis the hydrostatic assumption allows to introduce the relationship $\rho dz = -dp/g$ into Equation B2. For the official AOD products of RL06 and RL07, atmospheric mass distribution is then computed at each time step (time indexing dropped in the following) according to Dobslaw, Bergmann-Wolf, Dill, Poropat, and Flechtner (2017) as

$$I_n(\theta,\lambda) = \int_0^{\infty}\left(\frac{r_e(\theta)+z(\theta,\lambda)}{a_{45}}\right)^{n+2}\frac{dp(\theta,\lambda,z)}{g_{45}}, \quad \text{(B3)}$$

where a_{45} is the mean radius of the Earth computed at 45° latitude from semi-major axis of the reference ellipsoid and g_{45} is the standard gravity defined by the World Meteorological Organzation (WMO). The ellipsoidal latitude-dependent radius $r_e(\theta) = a\sqrt{(1-e^2 sin(\theta)^2)}$

is computed from the eccentricity e of the reference ellipsoid. The orthometric heights $z(\theta, \lambda)$ were derived from the reference orography by a transformation of the geopotential heights that the model levels refer to (Dobslaw, Bergmann-Wolf, Dill, Poropat, & Flechtner, 2017). In discrete format, the vertical integral in Equation B3 is approximated by a summation over N vertical layers from the bottom level $k = N$ to the top of the atmosphere (top-most layer) $k = 1$:

$$I_n(\theta, \lambda) = \sum_{k=1}^{N} \left(\frac{r_e(\theta) + z_k}{a_{45}} \right)^{n+2} \frac{\Delta p_k}{g_{45}}, \tag{B4}$$

Here, the pressure difference $\Delta p_k = \Delta p_k(\theta, \lambda)$ related to model level k at height $z_k = z_k(\theta, \lambda)$ is computed between the two adjacent interfaces $k-1/2$ and $k+1/2$ using air pressure derived at the model boundaries according to

$$p_{k+1/2} = a_{k+1/2} + b_{k+1/2} p_S, \tag{B5}$$

with p_S being surface pressure, and $a_{k+1/2}$ and $b_{k+1/2}$ being model constants which define the vertical model grid at hybrid sigma levels.

For our study, we now have to distinguish between two cases:

(i) For global atmospheric models and the CERRA reanalysis, where the hydrostatic assumption applies, we follow Forootan et al. (2013) and compute the – in comparison to Equation B4 – refined inner integral of atmospheric contributions

$$I_n(\theta, \lambda) = \sum_{k=1}^{N} \left(\frac{r_e(\theta) + \xi + z_k}{a} \right)^{n+2} \frac{\Delta p_k}{g(\theta, z_k)}, \tag{B6}$$

where a is the semi-major axis of the reference ellipsoid. Here, in contrast to the vertical integral computed for the official AOD product (Equation B4), the time-invariant height contribution from the geoid ξ=$\xi(\theta, \lambda)$, which is given as height in meter above an ellipsoid of revolution, is taken into account and latitude- and altitude-dependent gravity acceleration $g(\theta, z_k)$ instead of standard gravity is applied. Geometric height z_k is computed at each model level from geopotential height Φ_k^g following the conventions of the Office of the Federal Coordinator for Meteorology (OFCM, 1997),

$$z_k = \frac{r_e(\theta) \Phi_k^g}{\frac{g(\theta) r_e(\theta)}{g_{45}} - \Phi_k^g}, \tag{B7}$$

and refers to the geoid ξ.

(ii) For non-hydrostatic models, such as the regional COSMO-REA6 model applied in this study, we write the inner integral as

$$I_n(\theta, \lambda) = \int_0^{\infty} \left(\frac{r_e(\theta) + \xi + h + z}{a} \right)^{n+2} \rho(\theta, \lambda, z) dz. \tag{B8}$$

Here, the model height level z is referred to the orography $h = h(\theta, \lambda)$, and not to the geoid like in case (i), since COSMO-REA6 makes use of terrain-following coordinates (see Section A1). In discrete format, we sum again over N vertical layers according to

$$I_n(\theta, \lambda) = \left(\frac{r_e(\theta) + \xi + h + z}{a} \right)^{n+2} \left[\frac{\rho_1}{g(\theta)} + \sum_{k=2}^{N} \rho_k (z_{k-1/2} - z_{k+1/2}) \right]. \tag{B9}$$

The interface heights $z_{k+1/2}$ represent the height between model levels and $z_{N+1/2}$ equals to the surface height. The density ρ_k at each model level ($k = 2, \ldots, N$) is multiplied with the vertical distance of the two adjacent interfaces $z_{k-1/2} - z_{k+1/2}$. Additionally, the mass between z_1 and $z_{1+1/2}$ and the mass above the uppermost level need to be added

(described by the first summand in Equation B9). In order to estimate this term, we again assume a hydrostatic equilibrium state in the top atmosphere:

$$\int_{z_1}^{\infty} \rho dz = \int_{0}^{p_1} \frac{dp}{g(\theta)} = \frac{p_1}{g(\theta)} \tag{B10}$$

Here, p_1 represents the mass above the center of the upper most level and is prescribed by ERA-Interim top level pressure. In order to avoid computing the vertical integral repeatedly for each spherical harmonic degree, we can approximate Equation B8 by a Taylor expansion described in the supplementary material (not applied for the results shown here).

For the dry atmosphere we use $\rho = \rho_{dry}$ of dry air, whereas the wet atmosphere density ρ_{wet} includes density variations from specific humidity q, specific rain water content q_r, specific cloud water content q_c, specific cloud ice content q_i and specific snow content q_s as

$$\rho_{wet} = \rho_{dry} \frac{1}{1 - (q + q_c + q_r + q_i + q_s)}. \tag{B11}$$

The computation of VIM makes use of a number of physical constants and parameters. These are summarized in Table B2.

Table B1. Summary of physical constants and models used here

Constant	Value / Unit	Description	Source / Ref.
a	6378137.0 m	Semi major axis	WGS84 (NIMA, 2000)
$1/f$	298.257223563	Reciprocal of flattening	WGS84 (NIMA, 2000)
ω	$7.292115{\cdot}10^{-5}$ rad/s	Angular rotation rate	WGS84 (NIMA, 2000)
GM_e	$3.986004418{\cdot}10^{14}$ m^3/s^2	Geocentric gravitational constant	WGS84 (NIMA, 2000)
G_e	$6.6743{\cdot}10^{-11}$ m^2/(kg s^2)	Gravitational constant	Tiesinga et al. (2021)
g_{45}	9.80665 m/s^2	Standard gravity	WMO (2021)
M_e	kg	Mass of Earth	derived from GM_e and G_e
k'_n	dimensionless	Load Love Number	H. Wang et al. (2012)
ξ	m	Geoid height	GOCO06s (Kvas, Mayer-Gürr, et al., 2019)
h	m	Mean orography	COSMO-REA6 (Doms, 2011)
$\Phi^g_{k+1/2}$	m	Altitude-dependent geopotential height	ERA-I / ERA5 (Hersbach et al., 2020) & Forootan et al. (2013, Eq. 10)
$g(\theta)$	m/s^2	Latitude-dependent gravity	Forootan et al. (2013, Eq. 17)
$g(\theta, z_{k+1/2})$	m/s^2	Latitude- and altitude-dependent gravity	Forootan et al. (2013, Eq. 18)

B3 Overview on de-aliasing products

The computation of atmospheric de-aliasing products has been refined and extended during the last few years regarding the applied NWP model and its temporal and spa-

tial resolution, the treatment of tides, the consideration of the inverse barometer effect, the temporal coverage, and the vertical integration procedure. Table B2 provides an overview on AOD products of the last decade. The refined vertical integration method, which is also applied in this paper, differs from the classical one applied in the official AOD products by considering the geoid undulation as component of the radial distance and by taking into account latitude-dependency of gravity acceleration (Yang et al., 2021).

B4 Nesting of regional models into global models

Regional refinement of global atmospheric or hydrological models involves (i) re-gridding or coarse-graining to obtain homogeneous grids for the computation of spherical harmonic coefficients and (ii) tapering of the boundary between the global and regional model to avoid jumps which would translate to the so-called "Gibbs" phenomenon in spectral space characterized by ring patterns.

Before nesting, the temporal resolution of regional and global data sets needs to be unified. Common de-aliasing products used in the gravity field estimation process consist of 3-hourly fields of mass variations. Consequently, we temporally averaged hourly fields and applied temporal interpolation to the 6-hourly fields. Nesting of the regional model into the global model is performed for the hydrological models using TWS output of each model. For the atmospheric models, the inner integrals (Equation B2) are nested for each degree n separately. The monthly mean is removed for each data set before nesting.

Then, in the first step, the model grids are homogenized by re-gridding them to a regular geographical grid of similar resolution like the rotated grid of the regional (high resolution) model, i.e., 0.1°. In the second step, the transition area (Figure B1) is defined where regional and global models are smoothed to avoid data jumps. A width of 1.5° for the transition area and a filter half width increasing from 0° at the borders of the transition area to 0.5° at the middle of the transition area for Gaussian filter Kernel leads to a satisfying smoothing effect at rather small differences between original and filtered data sets. In a final step, global, regional, and filtered data sets are put together (Figure B1) and converted into SH coefficients. As the nested gridded data sets are given

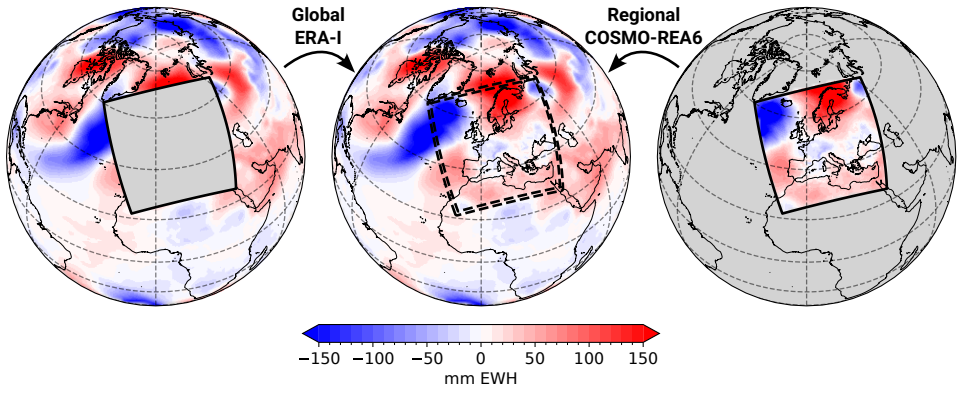

Figure B1. Nesting Procedure – Global model (ERA-I) without European CORDEX area (left), regional model (COSMO-REA6) given within the European CORDEX (right), both models and spatially filtered data in transition area (center) shown exemplarily for one snapshot of sub-monthly atmospheric mass.

on equally spaced geographical grids they satisfy the Driscoll and Healy sampling theorem (Driscoll & Healy, 1994). Thus, they can be converted into spherical harmonic co-

Table B2. Comparison of key attributes of available de-aliasing data sets.

Data set	**AOD-RL05**	**AOD-RL06**	**AOD-RL07**	**ITG3D**	**HUST-ERA5**	**AHD-UB**
Reference	Dobslaw et al. (2013)	Dobslaw, Bergmann-Wolf, Dill, Poropat, Thomas, et al. (2017)	Shihora et al. (2022)	Forootan et al. (2013)	Yang et al. (2021)	
NWP model	IFS	ERA-40/ERA-I/IFS	ERA5/IFS	ERA-I	ERA5	ERA-I/COSMO-REA6
lat. res.	∼0.5°	∼0.5°	∼0.31°	∼0.5°	∼0.31°	∼0.5° / ∼0.055°
degree/order	100	180	180	100	100	180 / 360
temp. res.	6-hourly	3-hourly	3-hourly	6-hourly	1-hourly	3-hourly
coverage	1989 - 2017	1976 - today	1975 - today	2002 - 2020	2002 - today	2007
tides	included	removed (12 frequencies)	removed (16 frequencies)	included	removed (12 frequencies)	included
temp. mean	2001 - 2002	2003 - 2014	2003 - 2014	2001 - 2002, monthly	2007 - 2014	monthly
IB effect	model	model	model	not corr.	model	not corr.
Vertical Integration Method	classic	classic	classic	refined	refined	refined

efficients using the Python toolbox pyshtools 4.1 (Wieczorek & Meschede, 2018), which implements the efficient Legendre transform algorithm described by Driscoll and Healy (1994).

Open Research Section

The de-aliasing data sets evaluated within this study are published as spherical harmonic coefficients at the German Research Centre For Geosciences (GFZ) data services repository via Mielke et al. (2023) with CC BY 4.0 licence. Please note that this paper refers to the updated data set version 2.0.

Acknowledgments

A.S., C.M., S.D., and L.Z. were funded by the Deutsche Forschungsgemeinschaft (DFG, German Research Foundation) as part of the Research Unit 2736 NEROGRAV. A.S. was funded as part of the DFG - SFB 1502/1-2022 - Projektnummer: 450058266. The authors would like to thank Michael Murböck and Christoph Dahle for first tests with the provided data sets. Furthermore, the authors thank Andreas Hense for fruitful methodological discussions.

References

Abrykosov, P., Sulzbach, R., Pail, R., Dobslaw, H., & Thomas, M. (2021, December). Treatment of ocean tide background model errors in the context of GRACE/GRACE-FO data processing. *Geophysical Journal International*, *228*(3), 1850–1865. Retrieved 2023-09-01, from `https://academic.oup.com/gji/article/228/3/1850/6396752` doi: 10.1093/gji/ggab421

Andersen, O. B., Nielsen, K., Knudsen, P., Hughes, C. W., Bingham, R., Fenoglio-Marc, L., ... Polo, S. P. (2018, November). Improving the Coastal Mean Dynamic Topography by Geodetic Combination of Tide Gauge and Satellite Altimetry. *Marine Geodesy*, *41*(6), 517–545. Retrieved 2023-08-04, from `https://www.tandfonline.com/doi/full/10.1080/01490419.2018.1530320` doi: 10.1080/01490419.2018.1530320

Arakawa, A., & Lamb, V. R. (1981). A potential enstrophy and energy conserving scheme for the shallow water equations. *Mon. Weather Rev.*, *109*, 18–36.

Asensio, H., Messmer, M., Lüthi, D., Osterried, K., & Jucker, J. (2020, May 28). *External parameters for numerical weather prediction and climate application: Extpar v5_4* (User and Implementation Guide). Retrieved from `http://www.cosmo-model.org/content/support/software/ethz/EXTPAR_user_and_implementation_manual.pdf`

Behzadpour, S., Mayer-Gürr, T., Flury, J., Klinger, B., & Goswami, S. (2019, August). Multiresolution wavelet analysis applied to GRACE range-rate residuals. *Geoscientific Instrumentation, Methods and Data Systems*, *8*(2), 197–207. Retrieved 2022-12-31, from `https://gi.copernicus.org/articles/8/197/2019/` (Publisher: Copernicus GmbH) doi: 10.5194/gi-8-197-2019

Bengtsson, L., Andrae, U., Aspelien, T., Batrak, Y., Calvo, J., de Rooy, W., ... Ødegaard Køltzow, M. (2017). The harmonie–arome model configuration in the aladin–hirlam nwp system. *Mon. Weather. Rev.*, *145*(5), 1919–1935. doi: 10.1175/MWR-D-16-0417.1

Bollmeyer, C., Keller, J. D., Ohlwein, C., Wahl, S., Crewell, S., Friederichs, P., ... Steinke, S. (2015, January). Towards a high-resolution regional reanalysis for the European CORDEX domain. *Quarterly Journal of the Royal Meteorological Society*, *141*(686), 1–15. Retrieved 2023-01-02, from `https://rmets.onlinelibrary.wiley.com/doi/10.1002/qj.2486` (Publisher: John Wiley & Sons, Ltd) doi: 10.1002/qj.2486

Bonin, J. A., & Chambers, D. P. (2011, September). Evaluation of high-frequency oceanographic signal in GRACE data: Implications for de-aliasing: HIGH-FREQUENCY SIGNALS IN GRACE DATA. *Geophysical Research Letters*, *38*(17), n/a–n/a. Retrieved 2023-08-28, from http://doi.wiley.com/10.1029/2011GL048881 doi: 10.1029/2011GL048881

Boy, J.-P., & Chao, B. F. (2005). Precise evaluation of atmospheric loading effects on Earth's time-variable gravity field. *Journal of Geophysical Research: Solid Earth*, *110*(B8). doi: 10.1029/2002JB002333

Cerri, L., Berthias, J. P., Bertiger, W. I., Haines, B. J., Lemoine, F. G., Mercier, F., ... Ziebart, M. (2010, August). Precision Orbit Determination Standards for the Jason Series of Altimeter Missions. *Marine Geodesy*, *33*(sup1), 379–418. Retrieved 2023-08-18, from http://www.tandfonline.com/doi/abs/10.1080/01490419.2010.488966 doi: 10.1080/01490419.2010.488966

Dahle, C., Murböck, M., Flechtner, F., Dobslaw, H., Michalak, G., Neumayer, K. H., ... Förste, C. (2019, January). The GFZ GRACE RL06 Monthly Gravity Field Time Series: Processing Details and Quality Assessment. *Remote Sensing*, *11*(18), 2116. Retrieved 2023-08-04, from https://www.mdpi.com/2072-4292/11/18/2116 doi: 10.3390/rs11182116

Dill, R. (2008). *Hydrological model LSDM for operational Earth rotation and gravity field variations* (Tech. Rep.). Deutsches GeoForschungsZentrum GFZ. Retrieved 2023-08-04, from https://gfzpublic.gfz-potsdam.de/pubman/item/item_8770 doi: 10.2312/GFZ.B103-08095

Dobslaw, H. (2016, July). Homogenizing surface pressure time-series from operational numerical weather prediction models for geodetic applications. *Journal of Geodetic Science*, *6*(1). Retrieved 2023-01-02, from https://www.degruyter.com/document/doi/10.1515/jogs-2016-0004/html (Publisher: De Gruyter Open Access Section: Journal of Geodetic Science) doi: 10.1515/jogs-2016-0004

Dobslaw, H., Bergmann-Wolf, I., Dill, R., Forootan, R., Klemann, V., Kusche, J., & Sasgen, I. (2015). The updated esa earth system model for future gravity mission simulation studies. *Journal of Geodesy*, *89*, 505–513.

Dobslaw, H., Bergmann-Wolf, I., Dill, R., Poropat, L., & Flechtner, F. (2017). *Product description document for aod1b release 06, rev.6.1.* (Technical Report). Potsdam, Germany: GFZ Potsdam. https://podaac.jpl.nasa.gov/dataset/GRACE_AOD1B_GRAV_GFZ_RL06.

Dobslaw, H., Bergmann-Wolf, I., Dill, R., Poropat, L., Thomas, M., Dahle, C., ... Flechtner, F. (2017, October). A new high-resolution model of non-tidal atmosphere and ocean mass variability for de-aliasing of satellite gravity observations: AOD1B RL06. *Geophysical Journal International*, *211*(1), 263–269. Retrieved 2023-08-21, from http://academic.oup.com/gji/article/211/1/263/3979461/A-new-highresolution-model-of-nontidal-atmosphere doi: 10.1093/gji/ggx302

Dobslaw, H., Bergmann-Wolf, I., Forootan, E., Dahle, C., Mayer-Gürr, T., Kusche, J., & Flechtner, F. (2016, May). Modeling of present-day atmosphere and ocean non-tidal de-aliasing errors for future gravity mission simulations. *Journal of Geodesy*, *90*(5), 423–436. Retrieved 2023-01-01, from https://link.springer.com/article/10.1007/s00190-015-0884-3 (Company: Springer Distributor: Springer Institution: Springer Label: Springer Number: 5 Publisher: Springer Berlin Heidelberg) doi: 10.1007/s00190-015-0884-3

Dobslaw, H., Flechtner, F., Bergmann-Wolf, I., Dahle, C., Dill, R., Esselborn, S., ... Thomas, M. (2013, July). Simulating high-frequency atmosphere-ocean mass variability for dealiasing of satellite gravity observations: AOD1B RL05: ATMOSPHERE-OCEAN MASS VARIABILITY: AOD1B. *Journal of Geophysical Research: Oceans*, *118*(7), 3704–3711. Retrieved 2023-08-09, from http://doi.wiley.com/10.1002/jgrc.20271 doi: 10.1002/jgrc.20271

Doms, G. (2011). *A description of the non-hydrostatic regional COSMO-Model - Part I: Dynamics and numerics* (Technical Report). Offenbach, Germany: Deutscher Wetterdienst.

Dong, D., Gross, R. S., & Dickey, J. O. (1996, April). Seasonal variations of the Earth's gravitational field: An analysis of atmospheric pressure, ocean tidal, and surface water excitation. *Geophysical Research Letters*, *23*(7), 725–728. Retrieved 2023-08-21, from http://doi.wiley.com/10.1029/96GL00740 doi: 10.1029/96GL00740

Driscoll, J., & Healy, D. (1994). Computing fourier transforms and convolutions on the 2-sphere. *Advances in Applied Mathematics*, *15*(2), 202-250. Retrieved from https://www.sciencedirect.com/science/article/pii/S0196885884710086 doi: https://doi.org/10.1006/aama.1994.1008

Döll, P., Hoffmann-Dobrev, H., Portmann, F., Siebert, S., Eicker, A., Rodell, M., ... Scanlon, B. (2012). Impact of water withdrawals from groundwater and surface water on continental water storage variations. *Journal of Geodynamics*, *59-60*, 143-156. Retrieved from https://www.sciencedirect.com/science/article/pii/S0264370711000597 (Mass Transport and Mass Distribution in the System Earth) doi: https://doi.org/10.1016/j.jog.2011.05.001

Döll, P., Müller Schmied, H., Schuh, C., Portmann, F. T., & Eicker, A. (2014). Global-scale assessment of groundwater depletion and related groundwater abstractions: Combining hydrological modeling with information from well observations and grace satellites. *Water Resources Research*, *50*(7), 5698-5720. Retrieved from https://agupubs.onlinelibrary.wiley.com/doi/abs/10.1002/2014WR015595 doi: https://doi.org/10.1002/2014WR015595

Eicker, A., & Springer, A. (2016, June). Monthly and sub-monthly hydrological variability: in-orbit validation by GRACE level 1B observations. *Journal of Geodesy*, *90*(6), 573–584. Retrieved 2022-05-19, from https://doi.org/10.1007/s00190-016-0895-8 doi: 10.1007/s00190-016-0895-8

Ek, M. B., Mitchell, K. E., Lin, Y., Rogers, E., Grunmann, P., Koren, V., ... Tarpley, J. D. (2003, November). Implementation of Noah land surface model advances in the National Centers for Environmental Prediction operational mesoscale Eta model. *Journal of Geophysical Research: Atmospheres*, *108*(D22), 2002JD003296. Retrieved 2023-08-31, from https://onlinelibrary.wiley.com/doi/abs/10.1029/2002JD003296 doi: 10.1029/2002JD003296

El-Said, A., Brousseau, P., Ridal, M., & Randriamampianina, R. (2021, June 03). A new temporally flow-dependent EDA estimating background errors in the new Copernicus European Regional Re-Analysis (CERRA). *ESS Open Archive*. doi: 10.1002/essoar.10507207.1

Elsaka, B., Raimondo, J.-C., Brieden, P., Reubelt, T., Kusche, J., Flechtner, F., ... Müller, J. (2014, January). Comparing seven candidate mission configurations for temporal gravity field retrieval through full-scale numerical simulation. *Journal of Geodesy*, *88*(1), 31–43. Retrieved 2022-12-31, from https://link.springer.com/article/10.1007/s00190-013-0665-9 (Company: Springer Distributor: Springer Institution: Springer Label: Springer Number: 1 Publisher: Springer Berlin Heidelberg) doi: 10.1007/s00190-013-0665-9

Farrell, W. E. (1972). Deformation of the Earth by surface loads. *Reviews of Geophysics*, *10*(3), 761. Retrieved 2023-08-21, from http://doi.wiley.com/10.1029/RG010i003p00761 doi: 10.1029/RG010i003p00761

Flechtner, F. (2020, October). *Realization of a satellite mission “GRACE-I” for parallel observation of changing global water resources and biodiversity* (Tech. Rep. No. GSTM2020-6). Copernicus Meetings. Retrieved 2023-08-28, from https://meetingorganizer.copernicus.org/GSTM2020/GSTM2020-6.html doi: 10.5194/gstm2020-6

Flechtner, F., Neumayer, K.-H., Dahle, C., Dobslaw, H., Fagiolini, E., Raimondo,

J.-C., & Güntner, A. (2016, March). What Can be Expected from the GRACE-FO Laser Ranging Interferometer for Earth Science Applications? *Surveys in Geophysics*, *37*(2), 453–470. Retrieved 2022-12-31, from https://link.springer.com/article/10.1007/s10712-015-9338-y (Company: Springer Distributor: Springer Institution: Springer Label: Springer Number: 2 Publisher: Springer Netherlands) doi: 10.1007/s10712-015-9338-y

Forootan, E., Didova, O., Kusche, J., & Löcher, A. (2013, May). Comparisons of atmospheric data and reduction methods for the analysis of satellite gravimetry observations. *Journal of Geophysical Research: Solid Earth*, *118*(5), 2382–2396. Retrieved 2022-12-31, from https://agupubs.onlinelibrary.wiley.com/doi/10.1002/jgrb.50160 (Publisher: John Wiley & Sons, Ltd) doi: 10.1002/jgrb.50160

Gal-Chen, T., & Somerville, R. C. (1975). On the use of a coordinate transformation for the solution of the navier–stokes equations. *J. Comput. Phys.*, *17*, 209–228.

Gerdener, H., Engels, O., & Kusche, J. (2020, January). A framework for deriving drought indicators from the Gravity Recovery and Climate Experiment (GRACE). *Hydrology and Earth System Sciences*, *24*(1), 227–248. Retrieved 2022-10-01, from https://hess.copernicus.org/articles/24/227/2020/ doi: 10.5194/hess-24-227-2020

Ghobadi-Far, K., Han, S., McCullough, C. M., Wiese, D. N., Ray, R. D., Sauber, J., ... Dobslaw, H. (2022, February). Along-Orbit Analysis of GRACE Follow-On Inter-Satellite Laser Ranging Measurements for Sub-Monthly Surface Mass Variations. *Journal of Geophysical Research: Solid Earth*, *127*(2). Retrieved 2023-08-04, from https://onlinelibrary.wiley.com/doi/10.1029/2021JB022983 doi: 10.1029/2021JB022983

Han, S.-C., Ghobadi-Far, K., Yeo, I.-Y., McCullough, C. M., Lee, E., & Sauber, J. (2021, November). GRACE Follow-On revealed Bangladesh was flooded early in the 2020 monsoon season due to premature soil saturation. *Proceedings of the National Academy of Sciences*, *118*(47), e2109086118. Retrieved 2023-08-16, from https://pnas.org/doi/full/10.1073/pnas.2109086118 doi: 10.1073/pnas.2109086118

Han, S.-C., Jekeli, C., & Shum, C. K. (2004, April). Time-variable aliasing effects of ocean tides, atmosphere, and continental water mass on monthly mean GRACE gravity field: TEMPORAL ALIASING ON GRACE GRAVITY FIELD. *Journal of Geophysical Research: Solid Earth*, *109*(B4). Retrieved 2023-08-28, from http://doi.wiley.com/10.1029/2003JB002501 doi: 10.1029/2003JB002501

Hastings, D. A., & Dunbar, P. K. (1999). *Global land one-kilometer base elevation (globe) digital elevation model, documentation, volume 1.0* (Key to Geophysical Records Documentation (KGRD) No. 34). 325 Broadway, Boulder, Colorado 80303, U.S.A.: National Oceanic and Atmospheric Administration, National Geophysical Data Center.

Hechler, P., & Bissolli, P. (2011). *Annual bulletin on the climate in wmo region vi - europe and middle east - 2007* (Technical Report). Offenbach, Germany: Deutscher Wetterdienst. Available at http://www.dwd.de/ravi.

Heller-Kaikov, B., Pail, R., & Daras, I. (2023, May). Mission design aspects for the mass change and geoscience international constellation (MAGIC). *Geophysical Journal International*, *235*(1), 718–735. Retrieved 2023-08-30, from https://academic.oup.com/gji/article/235/1/718/7218566 doi: 10.1093/gji/ggad266

Hersbach, H., Bell, B., Berrisford, P., Hirahara, S., Horányi, A., Muñoz-Sabater, J., ... Thépaut, J.-N. (2020). The era5 global reanalysis. *Q. J. R. Meteorol. Soc.*, *146*(730), 1999-2049.

Hoffmann, L., Günther, G., Li, D., Stein, O., Wu, X., Griessbach, S., ... Wright,

J. S. (2019). From era-interim to era5: the considerable impact of ecmwf's next-generation reanalysis on lagrangian transport simulations. *Atmospheric Chemistry and Physics*, *19*(5), 3097–3124.

Hofmann-Wellenhof, B., & Moritz, H. (2006). *Physical geodesy* (2nd, corrected ed ed.). Wien ; New York: SpringerWienNewYork.

Hunter, C., Moore, R., & McKendry, I. (2020, April). Evaluation of the North American Regional Reanalysis (NARR) precipitation fields in a topographically complex domain. *Hydrological Sciences Journal*, *65*(5), 786–799. Retrieved 2023-08-18, from https://www.tandfonline.com/doi/full/10.1080/02626667.2019.1591624 doi: 10.1080/02626667.2019.1591624

Kusche, J., Eicker, A., Forootan, E., Springer, A., & Longuevergne, L. (2016, August). Mapping probabilities of extreme continental water storage changes from space gravimetry. *Geophysical Research Letters*, *43*(15), 8026–8034. Retrieved 2022-09-25, from https://agupubs.onlinelibrary.wiley.com/doi/10.1002/2016GL069538 (Publisher: John Wiley & Sons, Ltd) doi: 10.1002/2016GL069538

Kvas, A., Behzadpour, S., Ellmer, M., Klinger, B., Strasser, S., Zehentner, N., & Mayer-Gürr, T. (2019a). Itsg-grace2018: Overview and evaluation of a new grace-only gravity field time series. *Journal of Geophysical Research: Solid Earth*, *124*(8), 9332-9344. Retrieved from https://agupubs.onlinelibrary.wiley.com/doi/abs/10.1029/2019JB017415 doi: https://doi.org/10.1029/2019JB017415

Kvas, A., Behzadpour, S., Ellmer, M., Klinger, B., Strasser, S., Zehentner, N., & Mayer-Gürr, T. (2019b, August). ITSG-Grace2018: Overview and Evaluation of a New GRACE-Only Gravity Field Time Series. *Journal of Geophysical Research: Solid Earth*, *124*(8), 9332–9344. Retrieved 2022-05-11, from https://onlinelibrary.wiley.com/doi/10.1029/2019JB017415 doi: 10.1029/2019JB017415

Kvas, A., & Mayer-Gürr, T. (2019, December). GRACE gravity field recovery with background model uncertainties. *Journal of Geodesy*, *93*(12), 2543–2552. Retrieved 2023-08-04, from https://doi.org/10.1007/s00190-019-01314-1 doi: 10.1007/s00190-019-01314-1

Kvas, A., Mayer-Gürr, T., Krauss, S., Brockmann, J. M., Schubert, T., Schuh, W.-D., ... Meyer, U. (2019). *The satellite-only gravity field model GOCO06s.* (GFZ Data Services) doi: https://doi.org/10.5880/ICGEM.2019.002

König, R., Reinhold, A., Dobslaw, H., Esselborn, S., Neumayer, K. H., Dill, R., & Michalak, A. (2021). On the effect of non-tidal atmospheric and oceanic loading on the orbits of the altimetry satellites ENVISAT, Jason-1 and Jason-2. *Advances in Space Research*, *68*(2), 1048–1058. Retrieved from https://www.sciencedirect.com/science/article/pii/S0273117720303963 doi: https://doi.org/10.1016/j.asr.2020.05.047

Li, H., Yi, S., Luo, Z., & Xu, P. (2023, January). *Contrasting behavior of July 2021 floods in Western Europe and Central China revealed by GRACE Follow-On ranging data* (preprint). Preprints. Retrieved 2023-08-16, from https://essopenarchive.org/users/572752/articles/617463-contrasting-behavior-of-july-2021-floods-in-western-europe-and-central-china-revealed-by-grace-follow-on-ranging-data?commit=e26f2e4e756a3651e4708804fdd3c034d2084895 doi: 10.22541/essoar.167397475.59864605/v1

Luthcke, S. B., Sabaka, T., Loomis, B., Arendt, A., McCarthy, J., & Camp, J. (2013). Antarctica, greenland and gulf of alaska land-ice evolution from an iterated grace global mascon solution. *Journal of Glaciology*, *59*(216), 613–631. doi: 10.3189/2013JoG12J147

Massotti, L., Siemes, C., March, G., Haagmans, R., & Silvestrin, P. (2021, January). Next Generation Gravity Mission Elements of the Mass Change and Geo-

science International Constellation: From Orbit Selection to Instrument and Mission Design. *Remote Sensing*, *13*(19), 3935. Retrieved 2023-08-04, from https://www.mdpi.com/2072-4292/13/19/3935 doi: 10.3390/rs13193935

Mielke, C., Springer, A., Dixit, S., Friederichs, P., Kusche, J., & Schindelegger, M. (2023). *Regionally refined high-resolution and mass-consistent AH+O de-aliasing coefficients for GRACE/-FO [Dataset].* GFZ Data Services. Retrieved 2023-09-18, from https://dataservices.gfz-potsdam.de/panmetaworks/showshort.php?id=c5848a57-af0b-11ed-95b8-f851ad6d1e4b doi: 10.5880/NEROGRAV.2023.002

Müller Schmied, H., Caceres, D., Eisner, S., Flörke, M., Herbert, C., Niemann, C., ... Döll, P. (2021). The global water resources and use model watergap v2.2d: Model description and evaluation. *Geoscientific Model Development*, *14*, 1037-1079.

Mémin, A., Boy, J.-P., & Santamaría-Gómez, A. (2020, April). Correcting GPS measurements for non-tidal loading. *GPS Solutions*, *24*(2), 1–13. Retrieved 2022-09-30, from https://link.springer.com/article/10.1007/s10291-020-0959-3 doi: 10.1007/s10291-020-0959-3

Müller Schmied, H., Cáceres, D., Eisner, S., Flörke, M., Herbert, C., Niemann, C., ... Döll, P. (2021, February). The global water resources and use model WaterGAP v2.2d: model description and evaluation. *Geoscientific Model Development*, *14*(2), 1037–1079. Retrieved 2023-08-04, from https://gmd.copernicus.org/articles/14/1037/2021/ doi: 10.5194/gmd-14-1037-2021

Neumeyer, J., Hagedoorn, J., Leitloff, J., & Schmidt, T. (2004). Gravity reduction with three-dimensional atmospheric pressure data for precise ground gravity measurements. *Journal of Geodynamics*, *38*(3), 437–450. Retrieved from https://www.sciencedirect.com/science/article/pii/S0264370704000821 doi: https://doi.org/10.1016/j.jog.2004.07.006

Nie, S., Zheng, W., Yin, W., Zhong, Y., Shen, Y., & Li, K. (2023, January). Improved the Characterization of Flood Monitoring Based on Reconstructed Daily GRACE Solutions over the Haihe River Basin. *Remote Sensing*, *15*(6), 1564. Retrieved 2023-08-16, from https://www.mdpi.com/2072-4292/15/6/1564 doi: 10.3390/rs15061564

NIMA. (2000). *Department of Defense World Geodetic System 1984: Its Definition and Relationship with Local Geodetic Systems* (TR8350.2). St. Louis, MO: National Imagery and Mapping Agency.

OFCM. (1997). *Federal Meteorological Handbook No. 3: Rawinsonde and Pibal Observations.* Silver Spring, Maryland. (available online at https://www.icams-portal.gov/resources/ofcm/fmh/FMH3/00-entire-FMH3.pdf)

Oleson, K. W., Niu, G.-Y., Yang, Z.-L., Lawrence, D. M., Thornton, P. E., Lawrence, P. J., ... Qian, T. (2008). Improvements to the community land model and their impact on the hydrological cycle. *Journal of Geophysical Research: Biogeosciences*, *113*(G1). Retrieved from https://agupubs.onlinelibrary.wiley.com/doi/abs/10.1029/2007JG000563 doi: https://doi.org/10.1029/2007JG000563

Pail, R., Bingham, R., Braitenberg, C., Dobslaw, H., Eicker, A., Güntner, A., ... Wouters, B. (2015, November). Science and User Needs for Observing Global Mass Transport to Understand Global Change and to Benefit Society. *Surveys in Geophysics*, *36*(6), 743–772. Retrieved 2022-09-30, from https://link.springer.com/article/10.1007/s10712-015-9348-9 doi: 10.1007/s10712-015-9348-9

Ray, R., & Ponte, R. (2003). Barometric tides from ecmwf operational analyses. *Annales Geophysicae*, *21*, 1897–1910.

Rienecker, M. M., Suarez, M. J., Gelaro, R., Todling, R., Bacmeister, J., Liu, E., ... Woollen, J. (2011, July). MERRA: NASA's Modern-Era Retrospective Anal-

ysis for Research and Applications. *Journal of Climate*, *24*(14), 3624–3648. Retrieved 2023-08-04, from http://journals.ametsoc.org/doi/10.1175/JCLI-D-11-00015.1 doi: 10.1175/JCLI-D-11-00015.1

Rodell, M., Famiglietti, J., Wiese, D., Reager, J., Beaudoing, H., Landerer, F., & Lo, H.-M. (2018). Emerging trends in global freshwater availability. *Nature*, *557*, 651–659.

Rodell, M., Houser, P. R., Jambor, U., Gottschalck, J., Mitchell, K., Meng, C.-J., ... Toll, D. (2004, March). The Global Land Data Assimilation System. *Bulletin of the American Meteorological Society*, *85*(3), 381–394. Retrieved 2023-08-31, from https://journals.ametsoc.org/doi/10.1175/BAMS-85-3-381 doi: 10.1175/BAMS-85-3-381

Rossi, L., Reguzzoni, M., Koç, Ö., Rosi, G., & Migliaccio, F. (2023, January). Assessment of gravity field recovery from a quantum satellite mission with atomic clocks and cold atom gradiometers. *Quantum Science and Technology*, *8*(1), 014009. Retrieved 2023-08-04, from https://iopscience.iop.org/article/10.1088/2058-9565/aca8cc doi: 10.1088/2058-9565/aca8cc

Saha, S., Moorthi, S., Pan, H.-L., Wu, X., Wang, J., Nadiga, S., ... Goldberg, M. (2010, August). The NCEP Climate Forecast System Reanalysis. *Bulletin of the American Meteorological Society*, *91*(8), 1015–1058. Retrieved 2023-08-04, from https://journals.ametsoc.org/view/journals/bams/91/8/2010bams3001_1.xml doi: 10.1175/2010BAMS3001.1

Save, H., Bettadpur, S., & Tapley, B. D. (2016, October). High-resolution CSR GRACE RL05 mascons: HIGH-RESOLUTION CSR GRACE RL05 MASCONS. *Journal of Geophysical Research: Solid Earth*, *121*(10), 7547–7569. Retrieved 2023-08-16, from http://doi.wiley.com/10.1002/2016JB013007 doi: 10.1002/2016JB013007

Schimanke, S., Ridal, M., Le Moigne, P., Berggren, L., Undén, P., Randriamampianina, R., ... Wang, Z. Q. (2021). *Cerra sub-daily regional reanalysis data for europe on model levels from 1984 to present.* Copernicus Climate Change Service (C3S) Climate Data Store (CDS). (Accessed on DD-MMM-YYYY) doi: 10.24381/cds.7c27fd20

Schindelegger, M., Harker, A. A., Ponte, R. M., Dobslaw, H., & Salstein, D. A. (2021, February). Convergence of Daily GRACE Solutions and Models of Submonthly Ocean Bottom Pressure Variability. *Journal of Geophysical Research: Oceans*, *126*(2), e2020JC017031. Retrieved 2023-01-02, from https://agupubs.onlinelibrary.wiley.com/doi/10.1029/2020JC017031 (Publisher: John Wiley & Sons, Ltd) doi: 10.1029/2020JC017031

Schraff, C., & Hess, R. (2003). *A description of the non-hydrostatic regional cosmo-model - part III: Data assimilation* (Technical Report). Offenbach, Germany: Deutscher Wetterdienst.

Seo, K.-W., Wilson, C. R., Chen, J., & Waliser, D. E. (2008, January). GRACE's spatial aliasing error. *Geophysical Journal International*, *172*(1), 41–48. Retrieved 2023-08-28, from https://academic.oup.com/gji/article-lookup/doi/10.1111/j.1365-246X.2007.03611.x doi: 10.1111/j.1365-246X.2007.03611.x

Shihora, L., Balidakis, K., Dill, R., Dahle, C., Ghobadi-Far, K., Bonin, J., & Dobslaw, H. (2022, August). Non-Tidal Background Modeling for Satellite Gravimetry Based on Operational ECWMF and ERA5 Reanalysis Data: AOD1B RL07. *Journal of Geophysical Research: Solid Earth*, *127*(8), e2022JB024360. Retrieved 2023-01-01, from https://agupubs.onlinelibrary.wiley.com/doi/10.1029/2022JB024360 (Publisher: John Wiley & Sons, Ltd) doi: 10.1029/2022JB024360

Springer, A., Eicker, A., Bettge, A., Kusche, J., & Hense, A. (2017, April). Evaluation of the Water Cycle in the European COSMO-REA6 Reanalysis Using GRACE. *Water*, *9*(4), 289. Retrieved 2023-01-02, from

https://www.mdpi.com/2073-4441/9/4/289 (Number: 4 Publisher: Multidisciplinary Digital Publishing Institute) doi: 10.3390/w9040289

Springer, A., Karegar, M. A., Kusche, J., Keune, J., Kurtz, W., & Kollet, S. (2019, October). Evidence of daily hydrological loading in GPS time series over Europe. *Journal of Geodesy*, *93*(10), 2145–2153. Retrieved 2023-08-21, from https://doi.org/10.1007/s00190-019-01295-1 doi: 10.1007/s00190-019-01295-1

Swenson, S., & Wahr, J. (2002). Estimated effects of the vertical structure of atmospheric mass on the time-variable geoid. *Journal of Geophysical research (Solid Earth)*, *107*, 2194.

Tapley, B. D., Watkins, M. M., Flechtner, F., Reigber, C., Bettadpur, S., Rodell, M., ... Velicogna, I. (2019, May). Contributions of GRACE to understanding climate change. *Nature Climate Change*, *9*(5), 358–369. Retrieved 2022-09-30, from https://www.nature.com/articles/s41558-019-0456-2 doi: 10.1038/s41558-019-0456-2

Termonia, P., Fischer, C., Bazile, E., Bouyssel, F., Brožková, R., Bénard, P., ... Joly, A. (2018). The ALADIN System and its canonical model configurations AROME CY41T1 and ALARO CY40T1. *Geosci. Model Dev.*, *11*, 257–281. doi: 10.5194/gmd-11-257-2018

Thompson, P. F., Bettadpur, S. V., & Tapley, B. D. (2004). Impact of short period, non-tidal, temporal mass variability on grace gravity estimates. *Geophysical Research Letters*, *31*(6). Retrieved from https://agupubs.onlinelibrary.wiley.com/doi/abs/10.1029/2003GL019285 doi: https://doi.org/10.1029/2003GL019285

Tiesinga, E., Mohr, P., Newell, D., & Taylor, B. (2021, 2021-06-30 04:06:00). CODATA Recommended Values of the Fundamental Physical Constants: 2018. *Reviews of Modern Physics*, *93*(93). Retrieved from https://tsapps.nist.gov/publication/get_pdf.cfm?pub_id=931443 doi: https://doi.org/10.1103/RevModPhys.93.025010

Uebbing, B., Kusche, J., Rietbroek, R., & Landerer, F. W. (2019, February). Processing Choices Affect Ocean Mass Estimates From GRACE. *Journal of Geophysical Research: Oceans*, *124*(2), 1029–1044. Retrieved 2022-10-31, from https://agupubs.onlinelibrary.wiley.com/doi/10.1029/2018JC014341 (Publisher: John Wiley & Sons, Ltd) doi: 10.1029/2018JC014341

Velicogna, I., Wahr, J., & Van Den Dool, H. (2001, August). Can surface pressure be used to remove atmospheric contributions from GRACE data with sufficient accuracy to recover hydrological signals? *Journal of Geophysical Research: Solid Earth*, *106*(B8), 16415–16434. Retrieved 2023-08-28, from http://doi.wiley.com/10.1029/2001JB000228 doi: 10.1029/2001JB000228

Wahr, J., Molenaar, M., & Bryan, F. (1998). Time variability of the Earth's gravity field: Hydrological and oceanic effects and their possible detection using GRACE. *Journal of Geophysical Research: Solid Earth*, *103*(B12), 30205–30229. Retrieved 2021-04-29, from http://doi.wiley.com/10.1029/98JB02844 doi: 10.1029/98JB02844

Wahr, J., Swenson, S., & Velicogna, I. (2006). Accuracy of GRACE mass estimates. *Geophysical Research Letters*, *33*(6), L06401. Retrieved 2023-08-28, from http://doi.wiley.com/10.1029/2005GL025305 doi: 10.1029/2005GL025305

Wang, H., Xiang, L., Jia, L., Jiang, L., Wang, Z., Hu, B., & Gao, P. (2012). Load Love numbers and Green's functions for elastic Earth models PREM, iasp91, ak135, and modified models with refined crustal structure from Crust 2.0. *Computers & Geosciences*, *49*, 190-199. Retrieved from https://www.sciencedirect.com/science/article/pii/S0098300412002245 doi: https://doi.org/10.1016/j.cageo.2012.06.022

Wang, Z. Q., & Randriamampianina, R. (2021). The Impact of Assimilating Satel-

lite Radiance Observations in the Copernicus European Regional Reanalysis (CERRA). *Remote Sens.*, *13*, 426. doi: 10.3390/rs13030426

WCRP Global Sea Level Budget Group. (2018). Global sea-level budget 1993–present. *Earth System Science Data*, *10*(3), 1551–1590. Retrieved from https://essd.copernicus.org/articles/10/1551/2018/ doi: 10.5194/essd-10-1551-2018

Weedon, G. P., Balsamo, G., Bellouin, N., Gomes, S., Best, M. J., & Viterbo, P. (2014, September). The WFDEI meteorological forcing data set: WATCH Forcing Data methodology applied to ERA-Interim reanalysis data. *Water Resources Research*, *50*(9), 7505–7514. Retrieved 2023-01-17, from http://doi.wiley.com/10.1002/2014WR015638 doi: 10.1002/2014WR015638

White, A. A., Hoskins, B. J., Roulstone, I., & Staniforth, A. (2005). Consistent approximate models of the global atmosphere: shallow, deep, hydrostatic, quasi-hydrostatic and non-hydrostatic. *Q. J. R. Meteorol. Soc.*, *131*(609), 2081-2107.

Wieczorek, M. A., & Meschede, M. (2018). Shtools: Tools for working with spherical harmonics. *Geochemistry, Geophysics, Geosystems*, *19*(8), 2574-2592. Retrieved from https://agupubs.onlinelibrary.wiley.com/doi/abs/10.1029/2018GC007529 doi: https://doi.org/10.1029/2018GC007529

Wiese, D. N., Bienstock, B., Blackwood, C., Chrone, J., Loomis, B. D., Sauber, J., ... Zlotnicki, V. (2022, August). The Mass Change Designated Observable Study: Overview and Results. *Earth and Space Science*, *9*(8), e2022EA002311. Retrieved 2022-09-30, from https://agupubs.onlinelibrary.wiley.com/doi/10.1029/2022EA002311 doi: 10.1029/2022EA002311

WMO. (2021). *Guide to Instruments and Methods of Observation* (WMO-No.8 Rep.) World Meteorological Organization. Retrieved from https://library.wmo.int/doc_num.php?explnum_id=11612

Wouters, B., Gardner, A. S., & Moholdt, G. (2019). Global Glacier Mass Loss During the GRACE Satellite Mission (2002-2016). *Frontiers in Earth Science*, *7*. Retrieved from https://www.frontiersin.org/articles/10.3389/feart.2019.00096 doi: 10.3389/feart.2019.00096

Wunsch, C., & Stammer, D. (1997). Atmospheric loading and the oceanic "inverted barometer" effect. *Reviews of Geophysics*, *35*, 79-107.

Yang, F., Forootan, E., Schumacher, M., Shum, C., & Zhong, M. (2018, November). Evaluating non-tidal atmospheric products by measuring GRACE K-band range rate residuals. *Geophysical Journal International*, *215*(2), 1132–1147. Retrieved 2023-08-16, from https://academic.oup.com/gji/article/215/2/1132/5075586 doi: 10.1093/gji/ggy340

Yang, F., Forootan, E., Wang, C., Kusche, J., & Luo, Z. (2021). A new 1-hourly era5-based atmosphere dealiasing product for grace, grace-fo, and future gravity missions. *Journal of Geophysical research (Solid Earth)*, *126*, e2021JB021926.

Yin, J., Liang, X., Xie, Y., Li, F., Hu, K., Cao, L., ... Liu, J. (2023, June). East Asia Reanalysis System (EARS). *Earth System Science Data*, *15*(6), 2329–2346. Retrieved 2023-09-04, from https://essd.copernicus.org/articles/15/2329/2023/ doi: 10.5194/essd-15-2329-2023

Zenner, L., Bergmann-Wolf, I., Dobslaw, H., Gruber, T., Güntner, A., Wattenbach, M., ... Dill, R. (2014, November). Comparison of Daily GRACE Gravity Field and Numerical Water Storage Models for De-aliasing of Satellite Gravimetry Observations. *Surveys in Geophysics*, *35*(6), 1251–1266. Retrieved 2022-05-19, from https://doi.org/10.1007/s10712-014-9295-x doi: 10.1007/s10712-014-9295-x

Zenner, L., Gruber, T., Beutler, G., & Jaeggi, A. (2010). Propagation of atmospheric model errors to gravity potential harmonics — impact on grace dealiasing. *Geophysical Journal International*, *182*, 797-807.

Zhan, W., Heki, K., Arief, S., & Yoshida, M. (2021, June). Topographic Amplification of Crustal Subsidence by the Rainwater Load of the 2019 Typhoon Hagibis in Japan. *Journal of Geophysical Research: Solid Earth*, *126*(6), e2021JB021845. Retrieved 2023-08-31, from https://agupubs.onlinelibrary.wiley.com/doi/10.1029/2021JB021845 doi: 10.1029/2021JB021845

Zhang, J., Liu, K., & Wang, M. (2023, February). Flood detection using Gravity Recovery and Climate Experiment (GRACE) terrestrial water storage and extreme precipitation data. *Earth System Science Data*, *15*(2), 521–540. Retrieved 2023-08-16, from https://essd.copernicus.org/articles/15/521/2023/ doi: 10.5194/essd-15-521-2023

Zhao, M., A, G., Velicogna, I., & Kimball, J. S. (2017, August). A Global Gridded Dataset of GRACE Drought Severity Index for 2002–14: Comparison with PDSI and SPEI and a Case Study of the Australia Millennium Drought. *Journal of Hydrometeorology*, *18*(8), 2117–2129. Retrieved 2022-09-30, from https://journals.ametsoc.org/view/journals/hydr/18/8/jhm-d-16-0182_1.xml doi: 10.1175/JHM-D-16-0182.1

Zhou, H., Zheng, L., Pail, R., Liu, S., Qing, T., Yang, F., ... Luo, Z. (2023, February). The impacts of reducing atmospheric and oceanic de-aliasing model error on temporal gravity field model determination. *Geophysical Journal International*, *234*(1), 210–227. Retrieved 2023-08-04, from https://academic.oup.com/gji/article/234/1/210/7036770 doi: 10.1093/gji/ggad064

Figure 1.

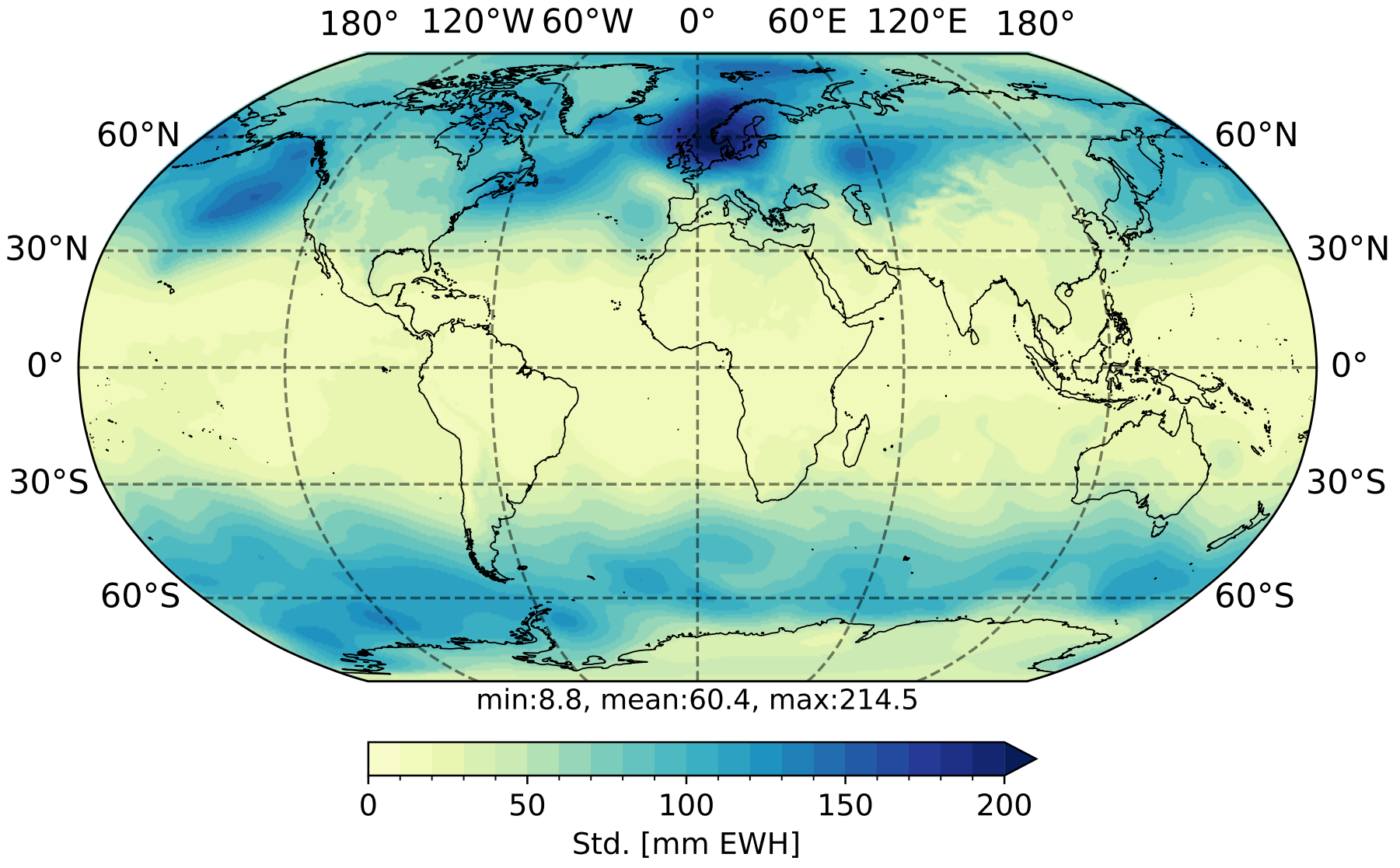
180° 120°W 60°W 0° 60°E 120°E 180°
60°N
30°N
0°
30°S
60°S
min:8.8, mean:60.4, max:214.5
0
50
100
150
200
Std. [mm EWH]

Figure 2.

(a) ERA5 - ERA-I

(b) ERA5 - COSMO-REA6

(c) CERRA - COSMO-REA6

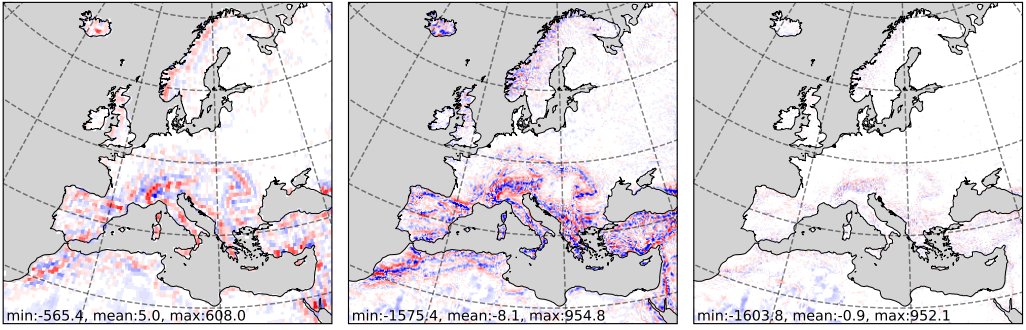

Figure 3.

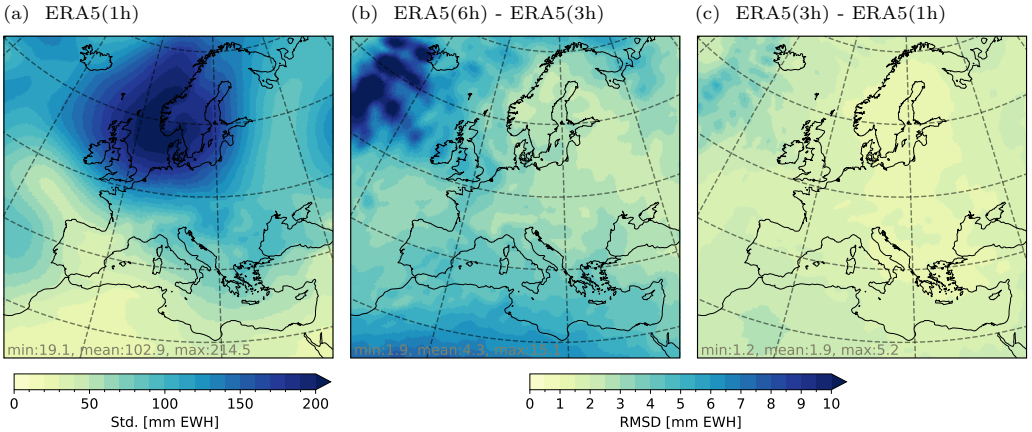
(a) ERA5(1h)
(b) ERA5(6h) - ERA5(3h)
(c) ERA5(3h) - ERA5(1h)
min:19.1, mean:102.9, max:214.5
min:1.9, mean:4.3, max:13.1
min:1.2, mean:1.9, max:5.2
0
50
100
150
200
Std. [mm EWH]
0
1
2
3
4
5
6
7
8
9
10
RMSD [mm EWH]

Figure 4.

(a) ERA5 - ERA-I

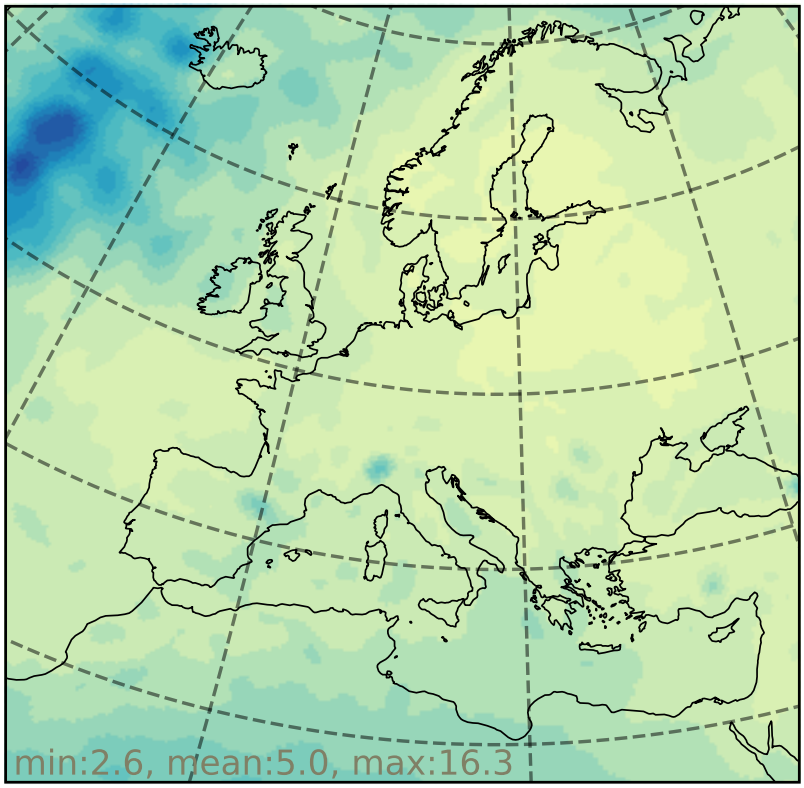

(b) ERA5 - CERRA

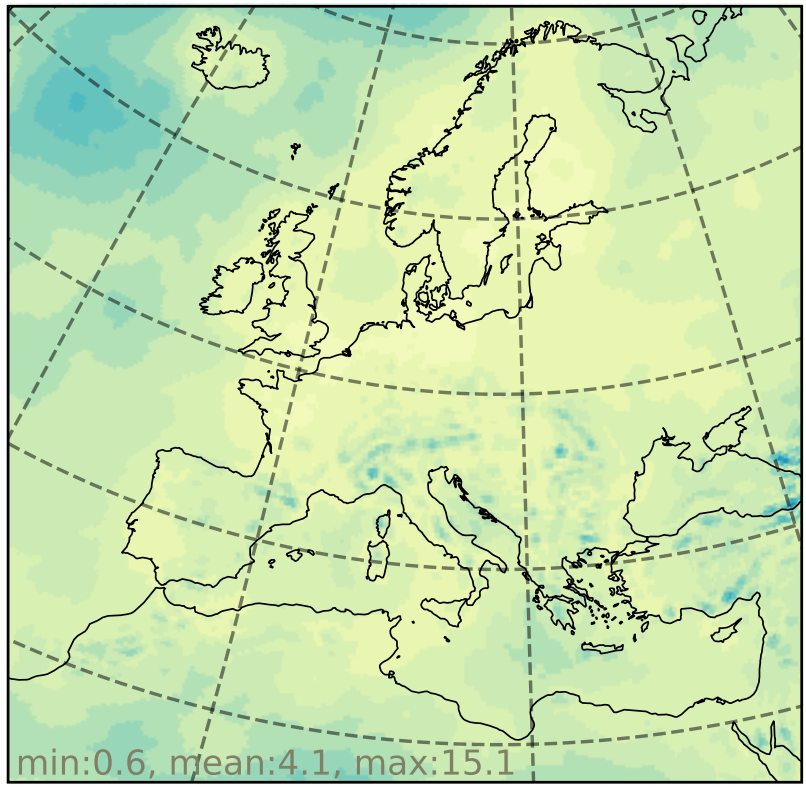

(c) ERA5 - COSMO-REA6

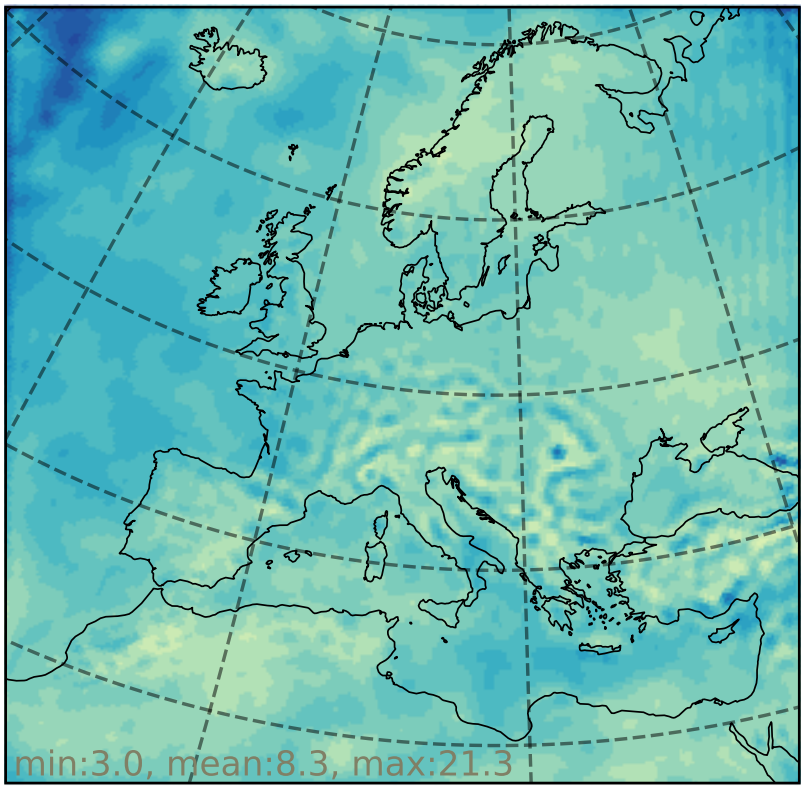

(d) CERRA - COSMO-REA6

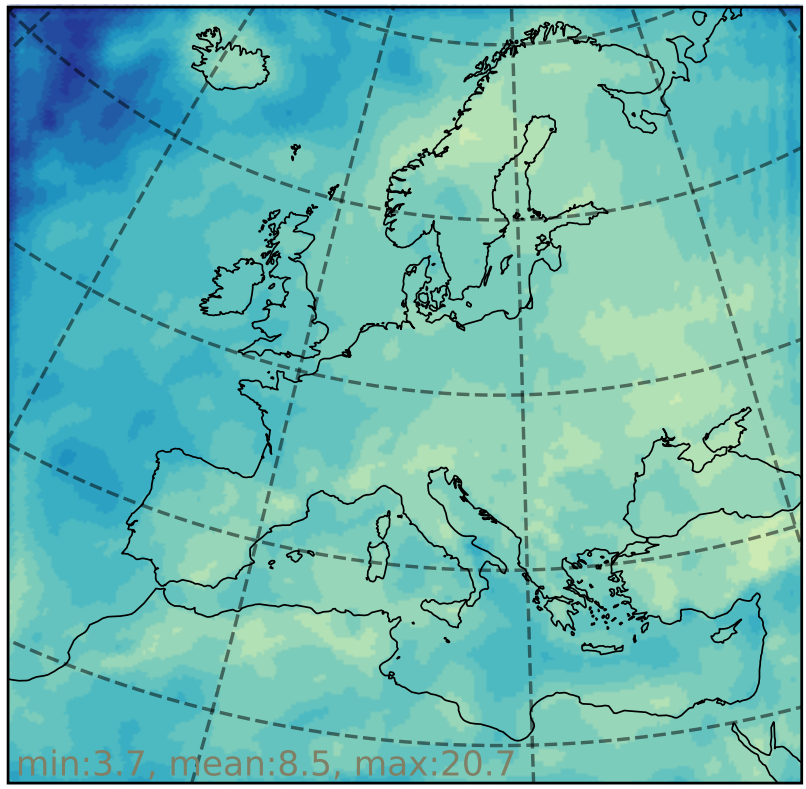

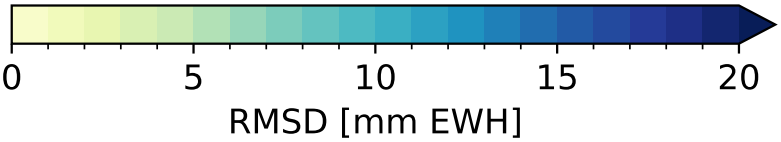

Figure 5.

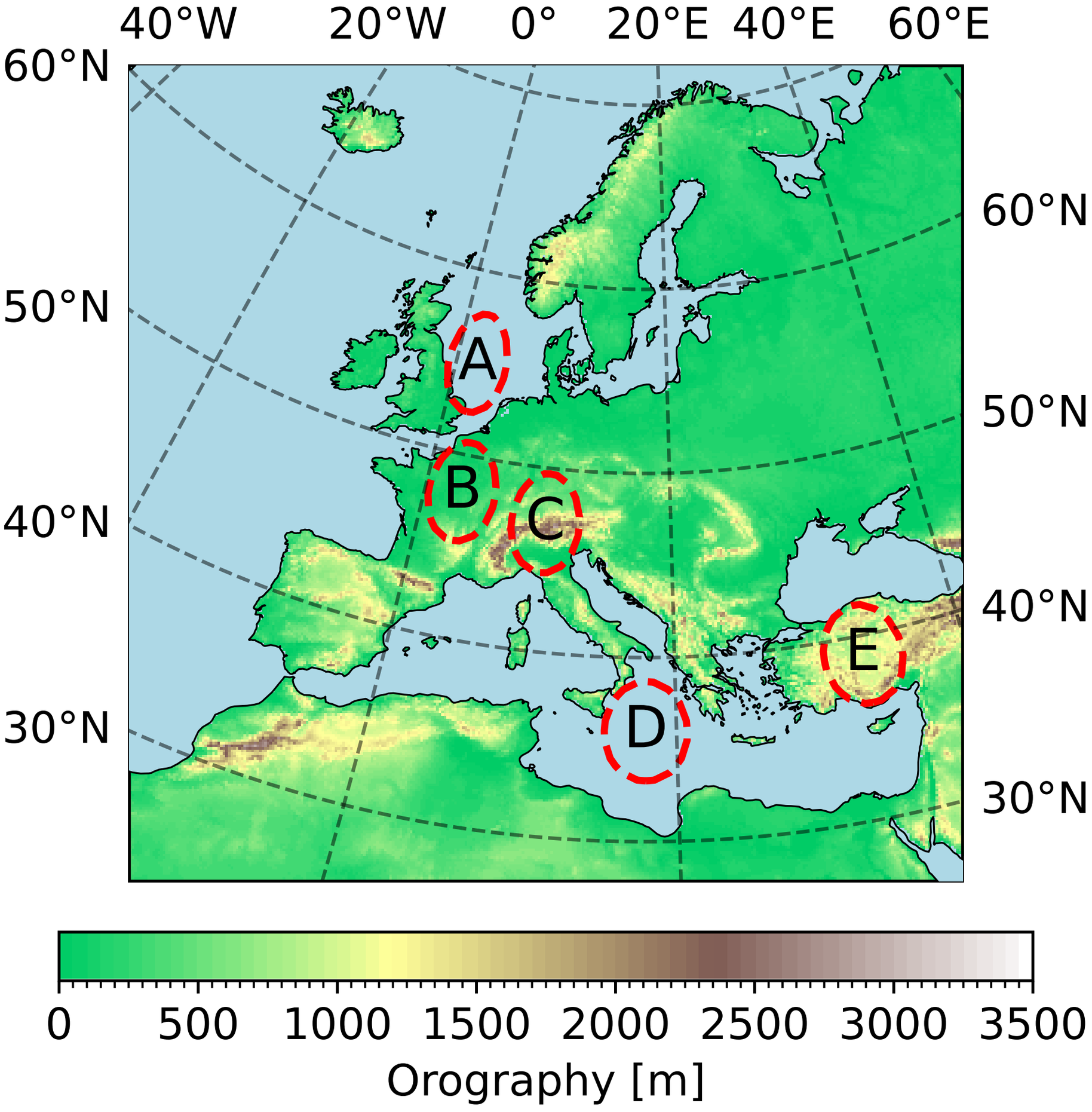
40°W
20°W
0°
20°E
40°E
60°E
60°N
50°N
40°N
30°N
A
B
C
D
E
0
500
1000
1500
2000
2500
3000
3500
Orography [m]

Figure 6.

(a) Absolute values

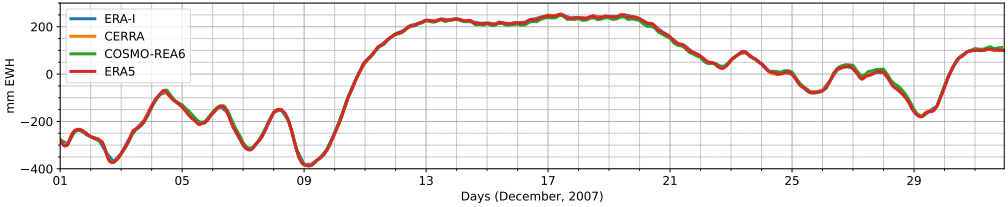

(b) Differences

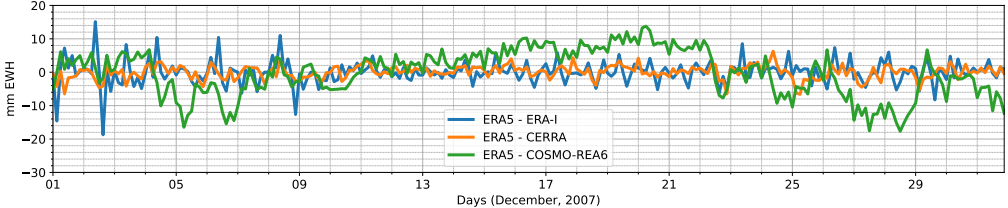

Figure 7.

(a) VIM_{wet}, Dec.

(b) VIM_{hum} - VIM_{dry}, Dec.

(c) VIM_{wet} - VIM_{hum}, Dec.

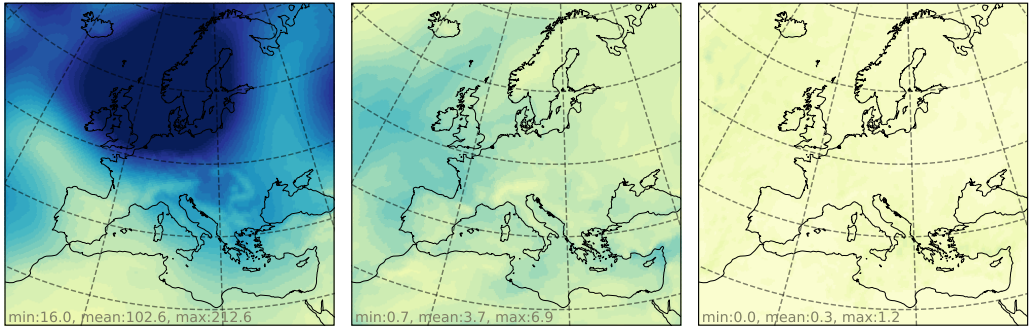

(d) VIM_{wet}, 5 Dec.

(e) VIM_{hum} - VIM_{dry}, 5 Dec.

(f) VIM_{wet} - VIM_{hum}, 5 Dec.

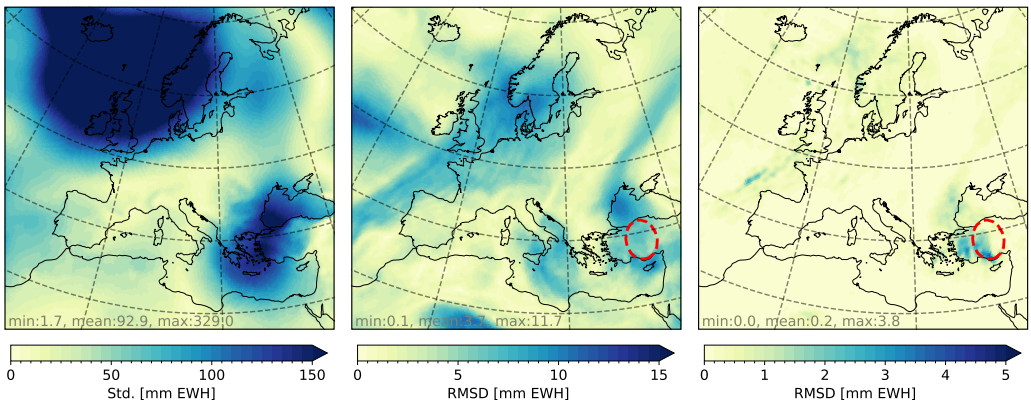

(g) Differences of VIM products for footprint E (Turkey)

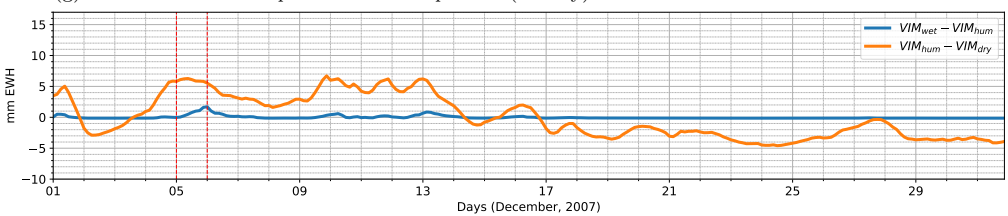

Figure 8.

(a) WGHM

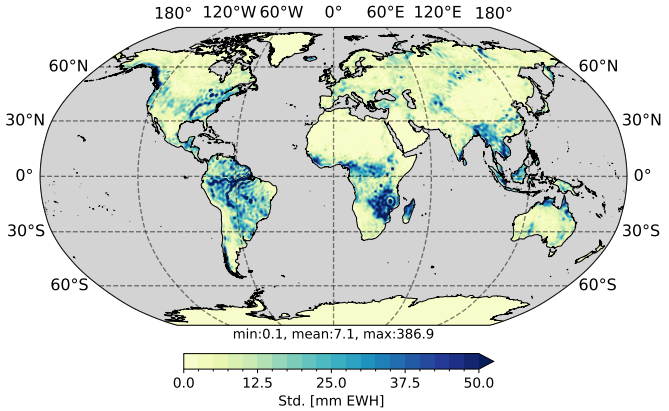

(b) CLM

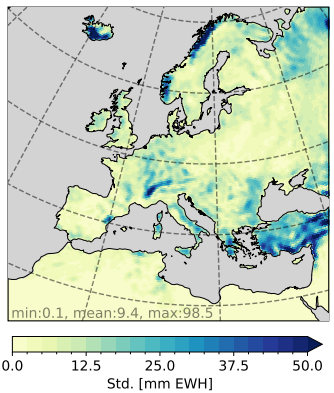

(c) WGHM - CLM

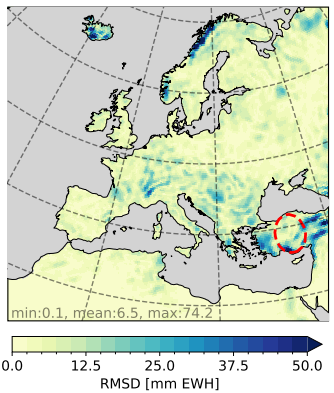

(d) Differences of hydrology for footprint E (Turkey)

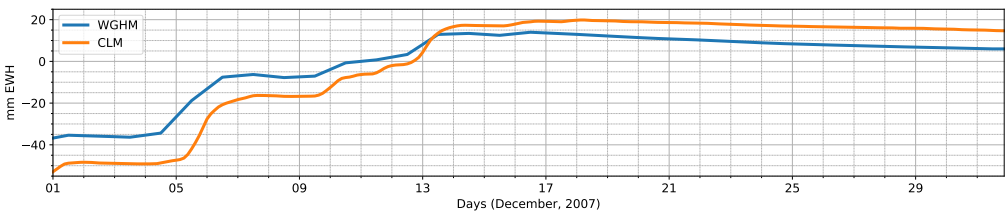

Figure B1.

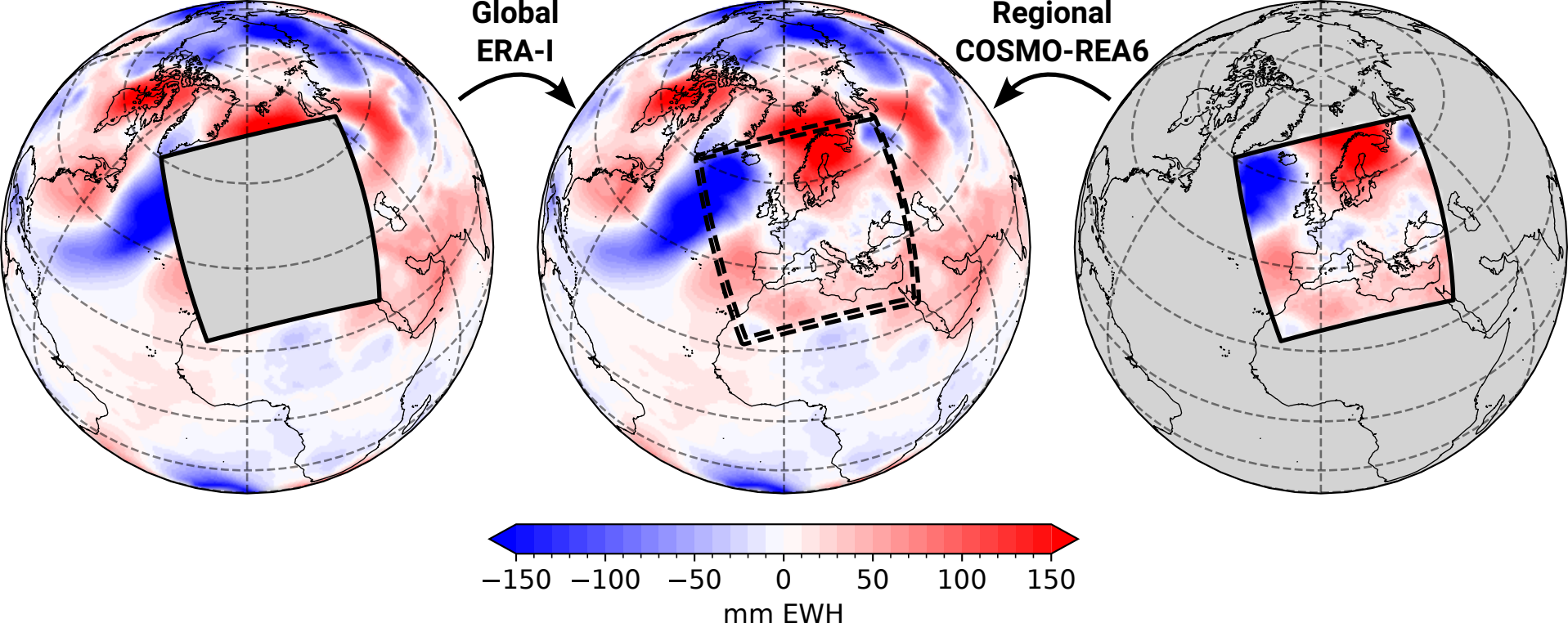
Global
ERA-I
Regional
COSMO-REA6
−150
−100
−50
0
50
100
150
mm EWH

Supporting Information for "A regionally refined and mass-consistent atmospheric and hydrological de-aliasing product for GRACE, GRACE-FO and future gravity missions"

Anne Springer[1], Christian A. Mielke[1], Ziyu Liu[2], Shashi Dixit[2], Petra Friederichs[2], Jürgen Kusche[1]

[1]Institute of Geodesy and Geoinformation, University of Bonn, Bonn, Germany

[2]Institute of Geosciences, University of Bonn, Bonn, Germany

Contents of this file

Text S1: Resource-saving approximate computation of vertically integrated mass for non-hydrostatic models

For non-hydrostatic models, such as the regional COSMO-REA6 model applied in this study, the inner integral described by Eq. B8 of the main document can be rewritten as

$$\begin{aligned} I_n(\theta,\lambda) &= \int_0^\infty \left(\frac{r_e(\theta)+\xi+h+z}{a}\right)^{n+2} \rho(\theta,\lambda,z)dz \\ &= \left(\frac{r_e(\theta)+\xi+h}{a}\right)^{n+2} \int_0^\infty \left(1+\frac{z}{r_e(\theta)+\xi+h}\right)^{n+2} \rho(\theta,\lambda,z)dz. \end{aligned} \tag{1}$$

Here, the model height level z is referred to the orography $h = h(\theta,\lambda)$, and not to the geoid like in the case of the hydrostatic models, since COSMO-REA6 makes use of terrain-following coordinates (see Section A1 of the Appendix in the main publication). The integrated term involving z to the power of $(n+2)$ is approximated to the first order using Taylor expansion, and can be dissected to the integration of ρdz and $\rho z dz$:

$$I_n(\theta,\lambda) \approx \left(\frac{r_e(\theta)+\xi+h}{a}\right)^{n+2} \left(\int_0^\infty \rho(\theta,\lambda,z)dz + \frac{(n+2)}{(r_e(\theta)+\xi+h)} \int_0^\infty \rho(\theta,\lambda,z)z dz\right). \tag{2}$$

As the degree n of the spherical harmonics is pulled out of the integral, the vertical integration now has to be performed only once and not for each degree separately. This means, all computations involving pressure and density fields can be prepared independent of the terms containing surface height and degree information. The first integral of Equation (2) is approximated in discrete form as

$$\int_0^\infty \rho dz \approx \frac{p_1}{g} + \rho_1(z_1 - z_{1+1/2}) + \sum_{k=2}^{N} \rho_k(z_{k-1/2} - z_{k+1/2}). \tag{3}$$

The vertical integral is approximated by a summation over N vertical layers from top to the surface. The density at each model level $(k = 2,\ldots,N)$ is multiplied with the vertical distance of two adjacent interface $z_{k-1/2} - z_{k+1/2}$. The second integral is approximated

accordingly as

$$\int_0^\infty \rho z dz = \int_0^\infty \rho d\frac{z^2}{2} \approx \frac{p_1 z_1}{g} + \frac{p_1^2}{\rho_1 g^2} + \rho_1 \frac{z_1^2 - z_{1+1/2}^2}{2} + \sum_{k=2}^{N} \rho_k \frac{z_{k-1/2}^2 - z_{k+1/2}^2}{2}. \tag{4}$$

Finally, the inner integral is computed according to

$$\begin{aligned} I_n(\theta,\lambda) \approx \left(\frac{r_e(\theta)+\xi+h}{a}\right)^{n+2} \Bigg[\left(\frac{p_1}{g} + \rho_1(z_1 - z_{1+1/2}) + \sum_{k=2}^{N} \rho_k (z_{k-1/2} - z_{k+1/2})\right) \\ + \frac{(n+2)}{(r_e(\theta)+\xi+h)} \left(\frac{p_1 z_1}{g} + \frac{p_1^2}{\rho_1 g^2} + \rho_1 \frac{z_1^2 - z_{1+1/2}^2}{2} + \sum_{k=2}^{N} \rho_k \frac{z_{k-1/2}^2 - z_{k+1/2}^2}{2}\right)\Bigg]. \end{aligned} \tag{5}$$

To estimate the mass and inner product above the uppermost layer of COSMO-REA6 (first term on the right side of Equation 3 and first two terms on the right side of Equation 4), we again assume a hydrostatic equilibrium state in the top atmosphere:

$$\int_{z_1}^\infty \rho dz = \int_0^{p_1} \frac{dp}{g} = \frac{p_1}{g} \tag{6}$$

$$\begin{aligned} \int_{z_1}^\infty \rho z dz &= \int_0^{p_1} z \frac{dp}{g} \\ &= \frac{1}{g}\left(p_1 z_1 - \int_{z_1}^\infty p dz\right) \\ &= \frac{p_1 z_1}{g} + \frac{R_L}{g^2}\int_0^{p_1} T dp \\ &\approx \frac{p_1 z_1}{g} + \frac{R_L T_1 p_1}{g^2} = \frac{p_1 z_1}{g} + \frac{p_1^2}{\rho_1 g^2}. \end{aligned} \tag{7}$$

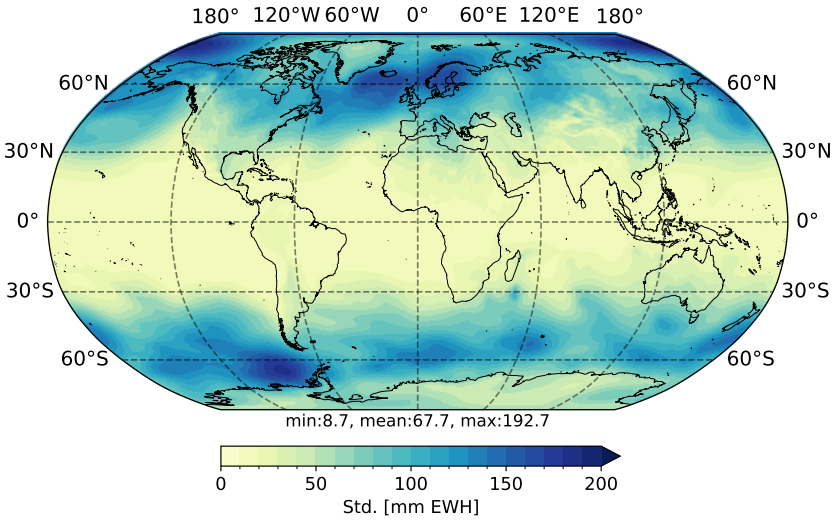

Figure S1. Standard deviation of ERA5-based sub-monthly vertically integrated atmospheric mass in March 2007.

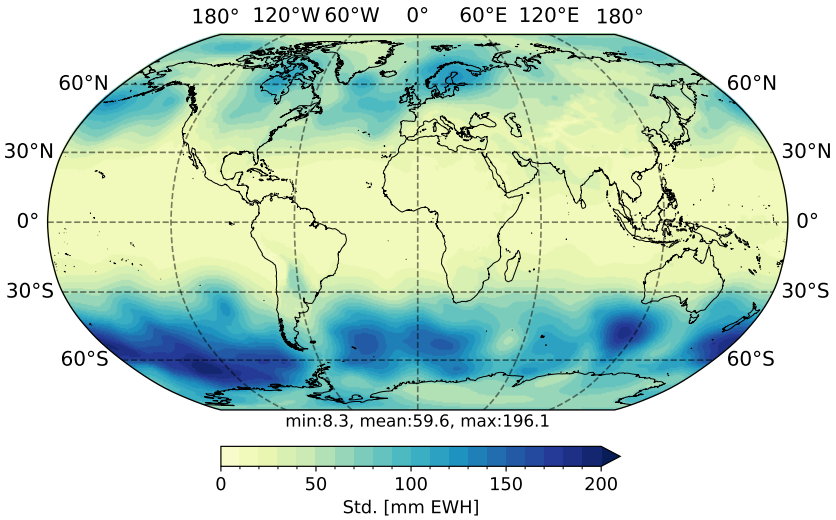

Figure S2. Standard deviation of ERA5-based sub-monthly vertically integrated atmospheric mass in June 2007.

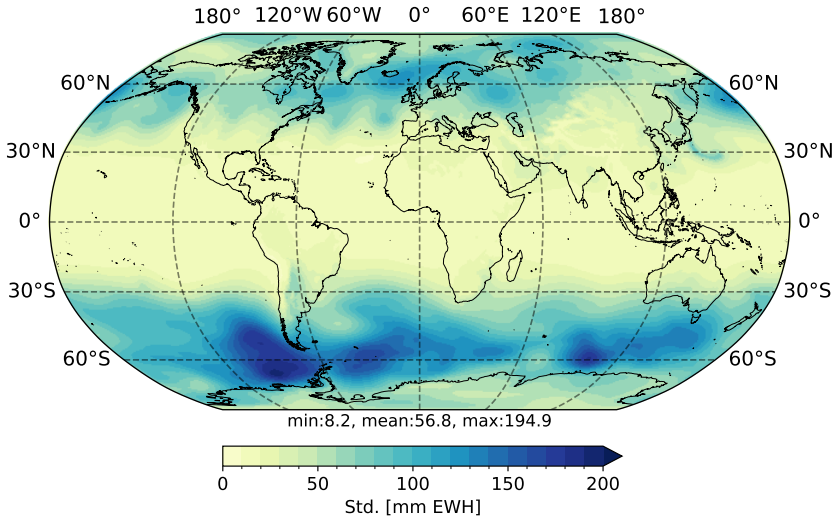

Figure S3. Standard deviation of ERA5-based sub-monthly vertically integrated atmospheric mass in September 2007.

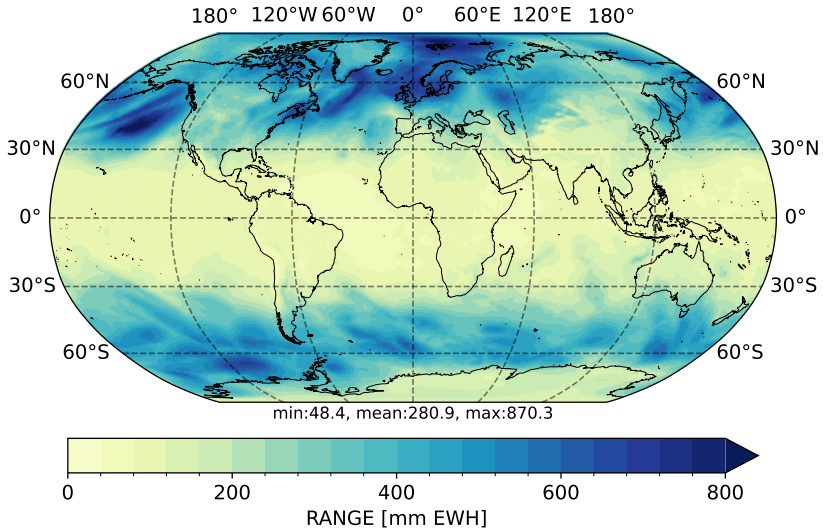

Figure S4. Range between minimum and maximum of ERA5-based sub-monthly vertically integrated atmospheric mass in December 2007.

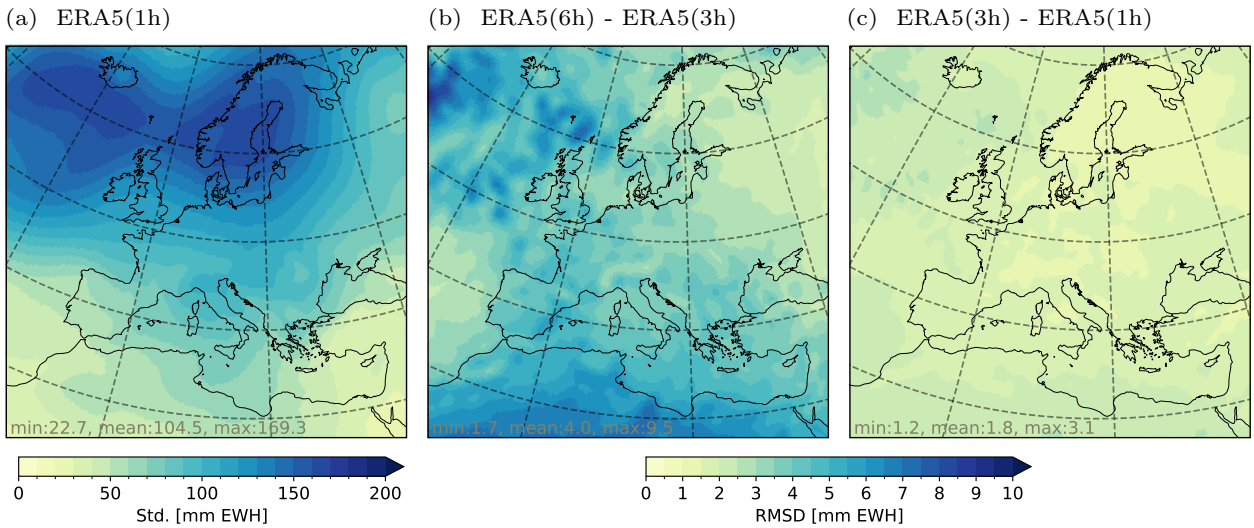

Figure S5. Root mean square deviation (RMSD) of sub-monthly atmospheric mass in March 2007 over the EURO-CORDEX region for (a) 1-hourly ERA5, (b) 6-hourly (linearly interpolated) ERA5 minus 3-hourly ERA5, and (c) 3-hourly (linearly interpolated) ERA5 minus 1-hourly ERA5. In order to compute differences between time series with different temporal resolution, the lower-resolution time series is linearly interpolated to the higher-resolution time steps.

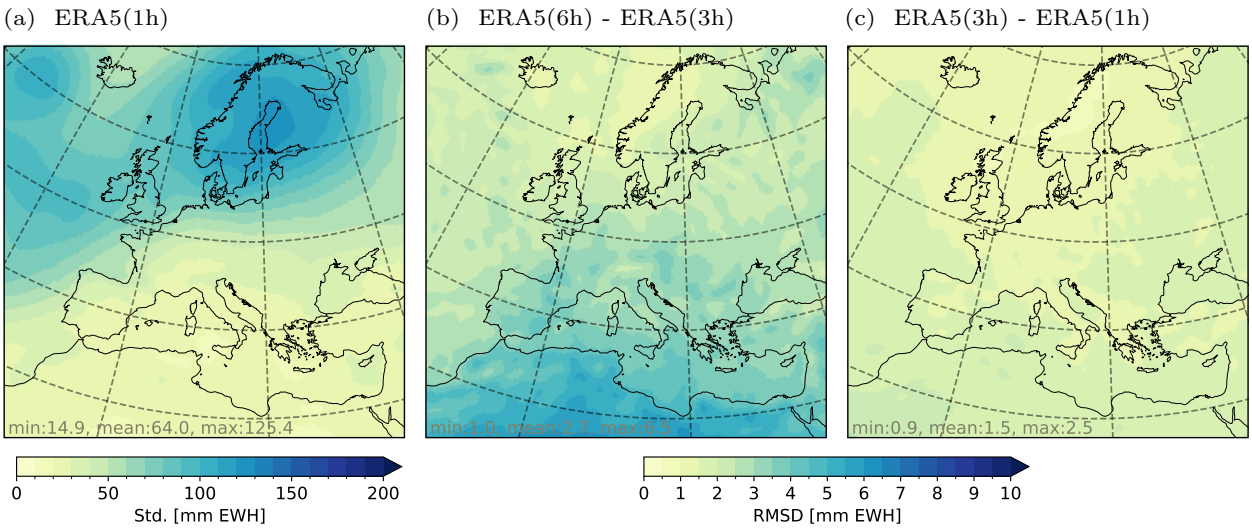

Figure S6. Root mean square deviation (RMSD) of sub-monthly atmospheric mass in June 2007 over the EURO-CORDEX region for (a) 1-hourly ERA5, (b) 6-hourly (linearly interpolated) ERA5 minus 3-hourly ERA5, and (c) 3-hourly (linearly interpolated) ERA5 minus 1-hourly ERA5. In order to compute differences between time series with different temporal resolution, the lower-resolution time series is linearly interpolated to the higher-resolution time steps.

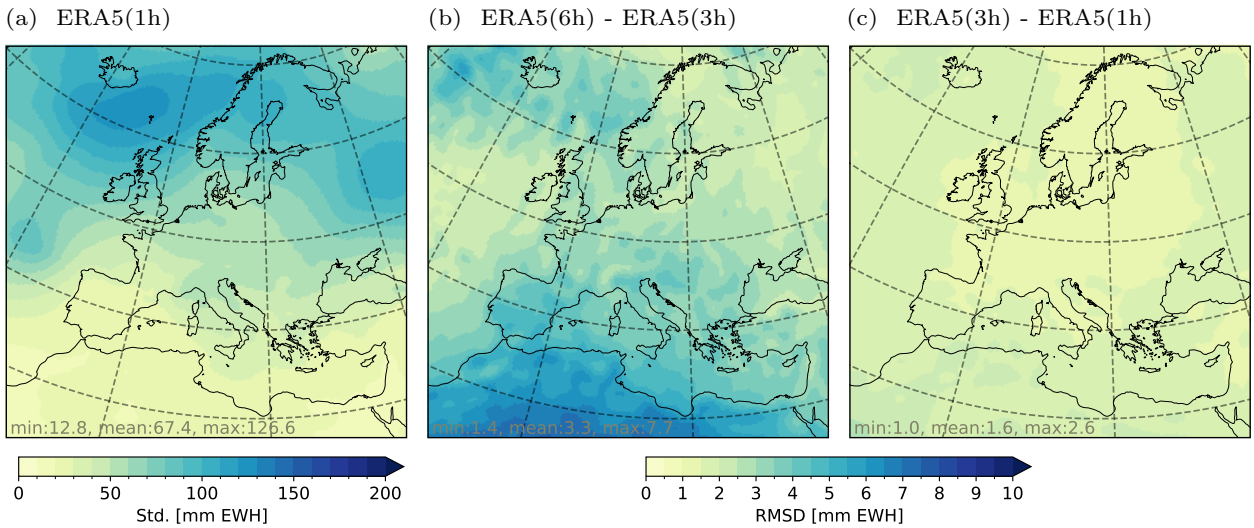

Figure S7. Root mean square deviation (RMSD) of sub-monthly atmospheric mass in September 2007 over the EURO-CORDEX region for (a) 1-hourly ERA5, (b) 6-hourly (linearly interpolated) ERA5 minus 3-hourly ERA5, and (c) 3-hourly (linearly interpolated) ERA5 minus 1-hourly ERA5. In order to compute differences between time series with different temporal resolution, the lower-resolution time series is linearly interpolated to the higher-resolution time steps.

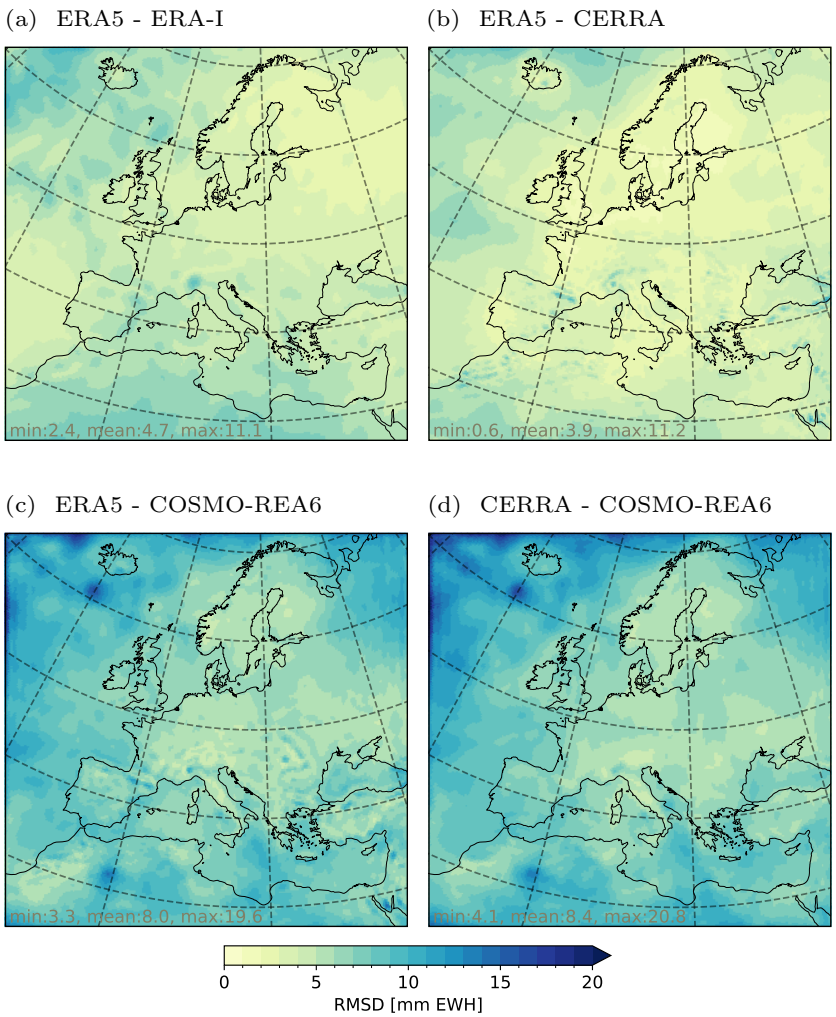

Figure S8. Root mean square deviation (RMSD) of vertically integrated atmospheric mass in March 2007 over the EURO-CORDEX domain between (a) 3-hourly ERA5 and 3-hourly ERA-I data (interpolated from 6-hourly fields), (b) 3-hourly ERA5 and 3-hourly CERRA data, (c) 3-hourly ERA5 and 3-hourly COSMO-REA6 data, and (d) 3-hourly CERRA and 3-hourly COSMO-REA6 data.

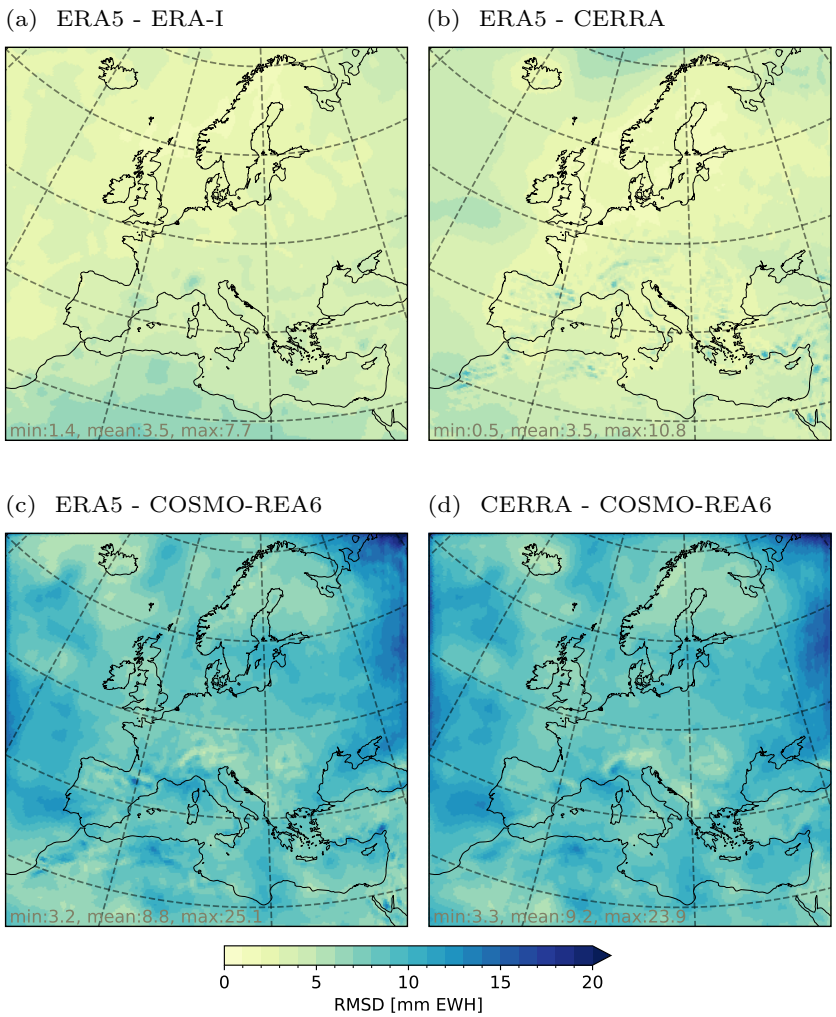

Figure S9. Root mean square deviation (RMSD) of vertically integrated atmospheric mass in June 2007 over the EURO-CORDEX domain between (a) 3-hourly ERA5 and 3-hourly ERA-I data (interpolated from 6-hourly fields), (b) 3-hourly ERA5 and 3-hourly CERRA data, (c) 3-hourly ERA5 and 3-hourly COSMO-REA6 data, and (d) 3-hourly CERRA and 3-hourly COSMO-REA6 data.

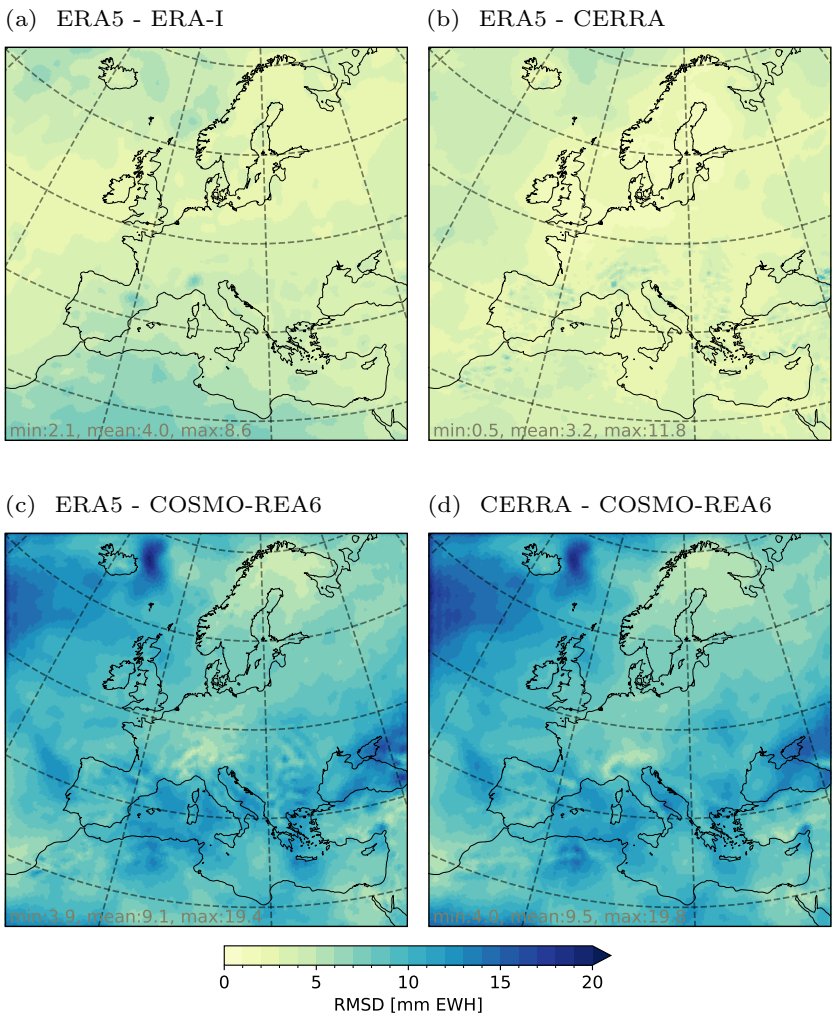

Figure S10. Root mean square deviation (RMSD) of vertically integrated atmospheric mass in September 2007 over the EURO-CORDEX domain between (a) 3-hourly ERA5 and 3-hourly ERA-I data (interpolated from 6-hourly fields), (b) 3-hourly ERA5 and 3-hourly CERRA data, (c) 3-hourly ERA5 and 3-hourly COSMO-REA6 data, and (d) 3-hourly CERRA and 3-hourly COSMO-REA6 data.

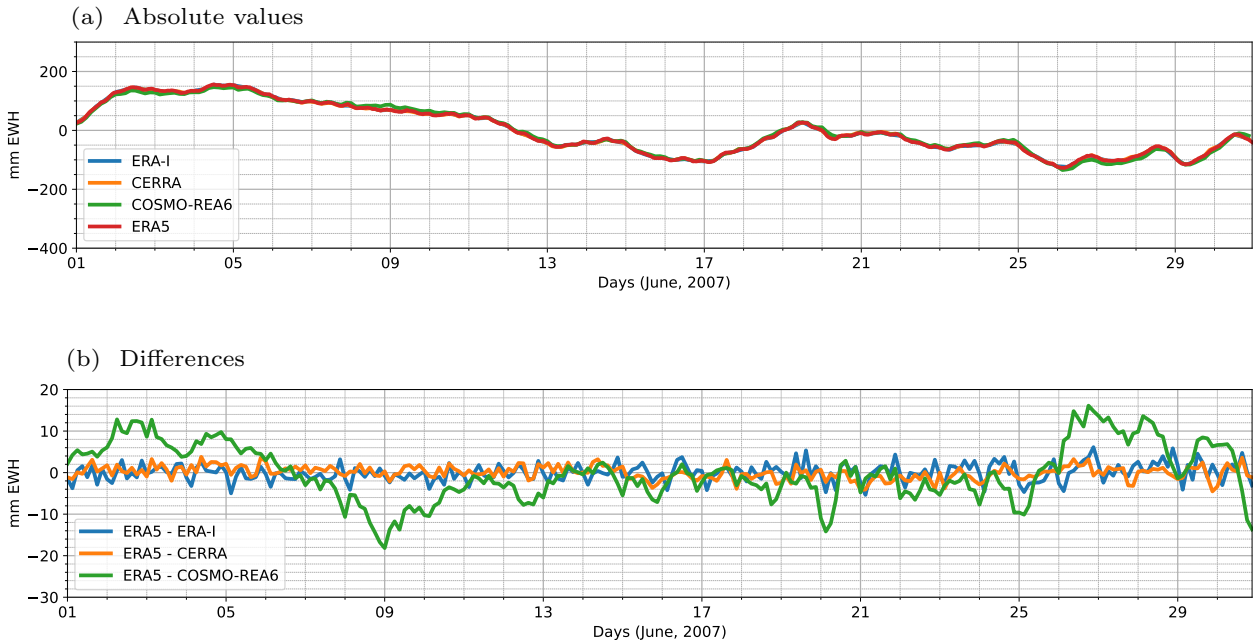

Figure S11. (a) Area-averaged sub-monthly vertically integrated atmospheric mass of all models within the investigated footprint A (North Sea at the British coast) and (b) the respective differences in comparison to ERA5 in June 2007.

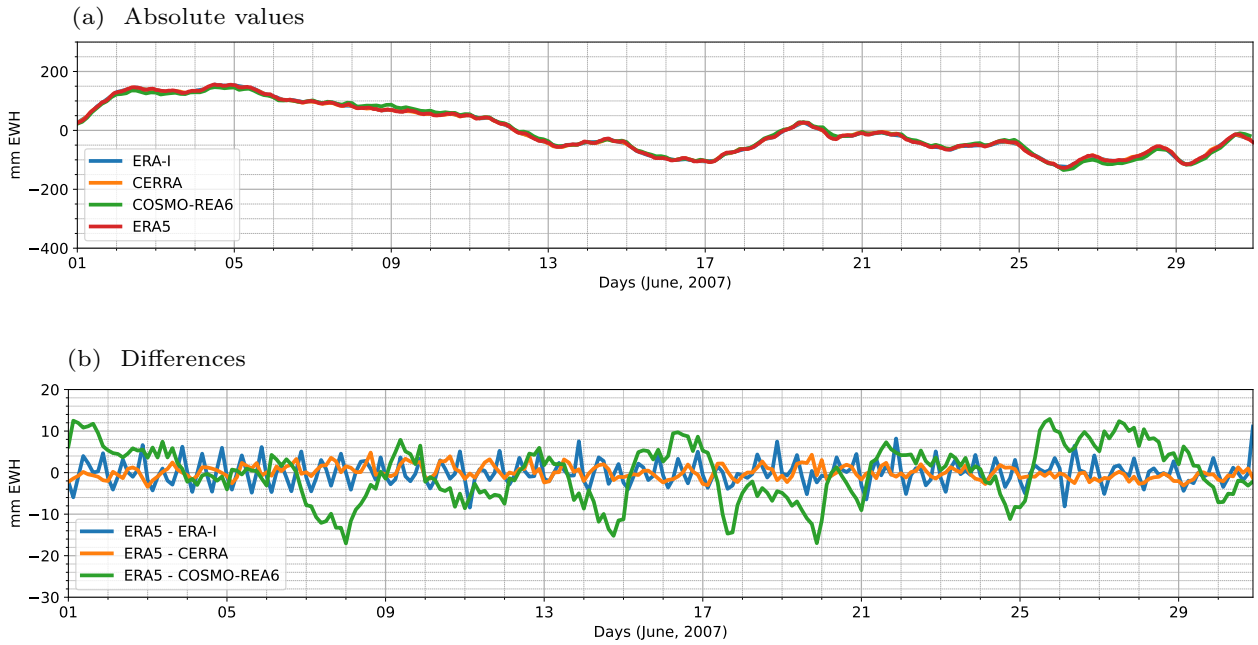

Figure S12. (a) Area-averaged sub-monthly vertically integrated atmospheric mass of all models within the investigated footprint B (France) and (b) the respective differences in comparison to ERA5 in June 2007.

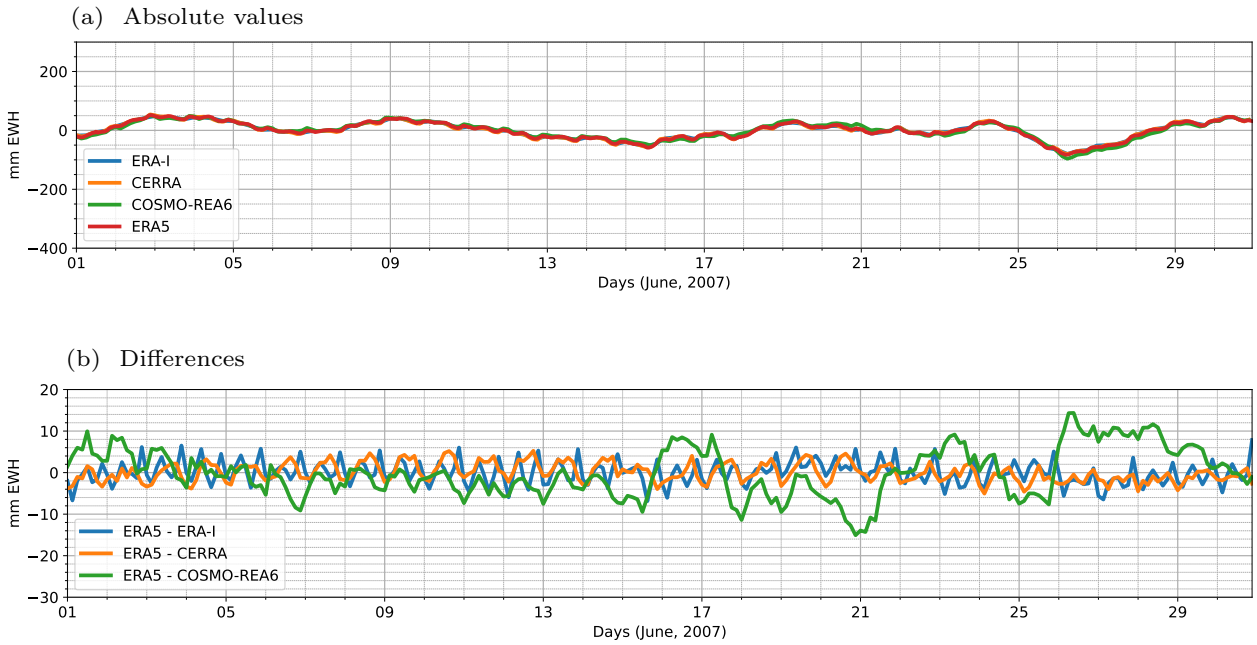

Figure S13. (a) Area-averaged sub-monthly vertically integrated atmospheric mass of all models within the investigated footprint C (Alps) and (b) the respective differences in comparison to ERA5 in June 2007.

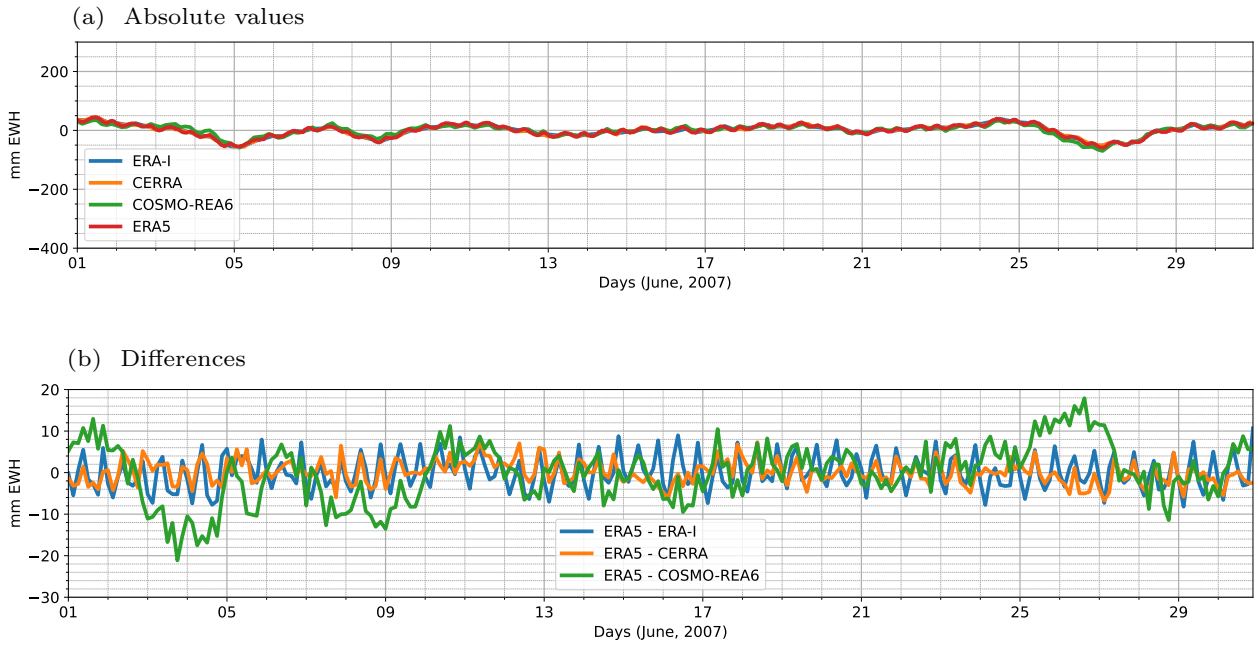

Figure S14. (a) Area-averaged sub-monthly vertically integrated atmospheric mass of all models within the investigated footprint D (Mediterranean Sea) and (b) the respective differences in comparison to ERA5 in June 2007.

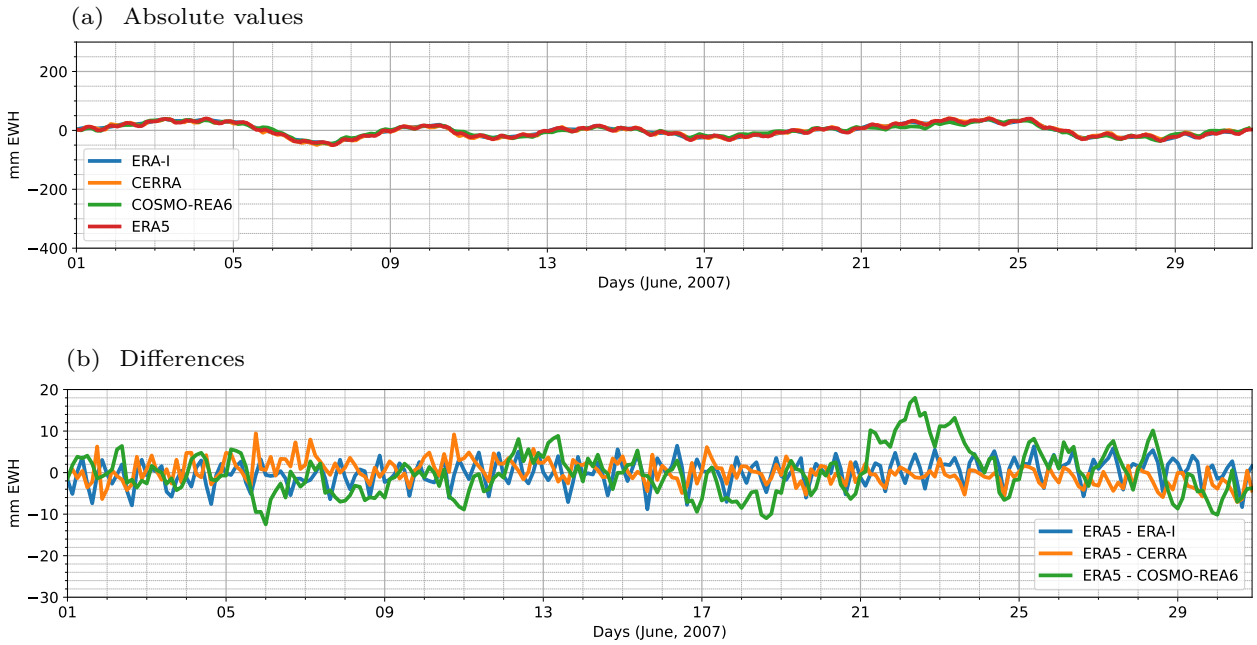

Figure S15. (a) Area-averaged sub-monthly vertically integrated atmospheric mass of all models within the investigated footprint E (Turkey) and (b) the respective differences in comparison to ERA5 in June 2007.

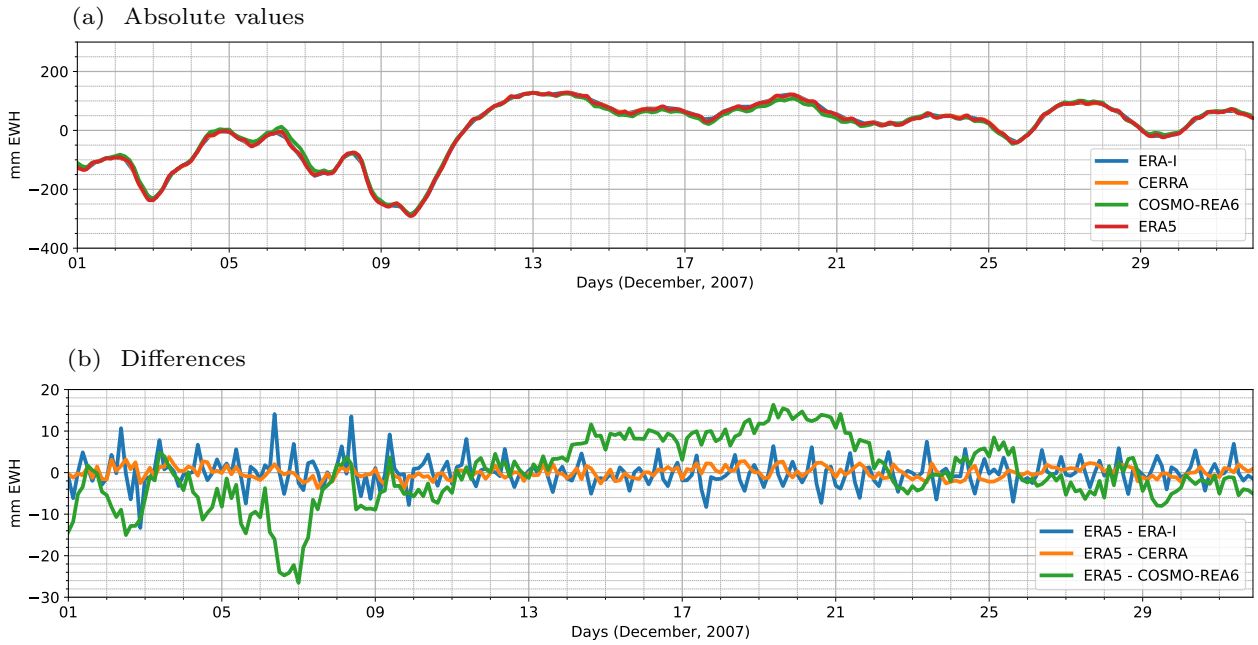

Figure S16. (a) Area-averaged sub-monthly vertically integrated atmospheric mass of all models within the investigated footprint B (France) and (b) the respective differences in comparison to ERA5 in December 2007.

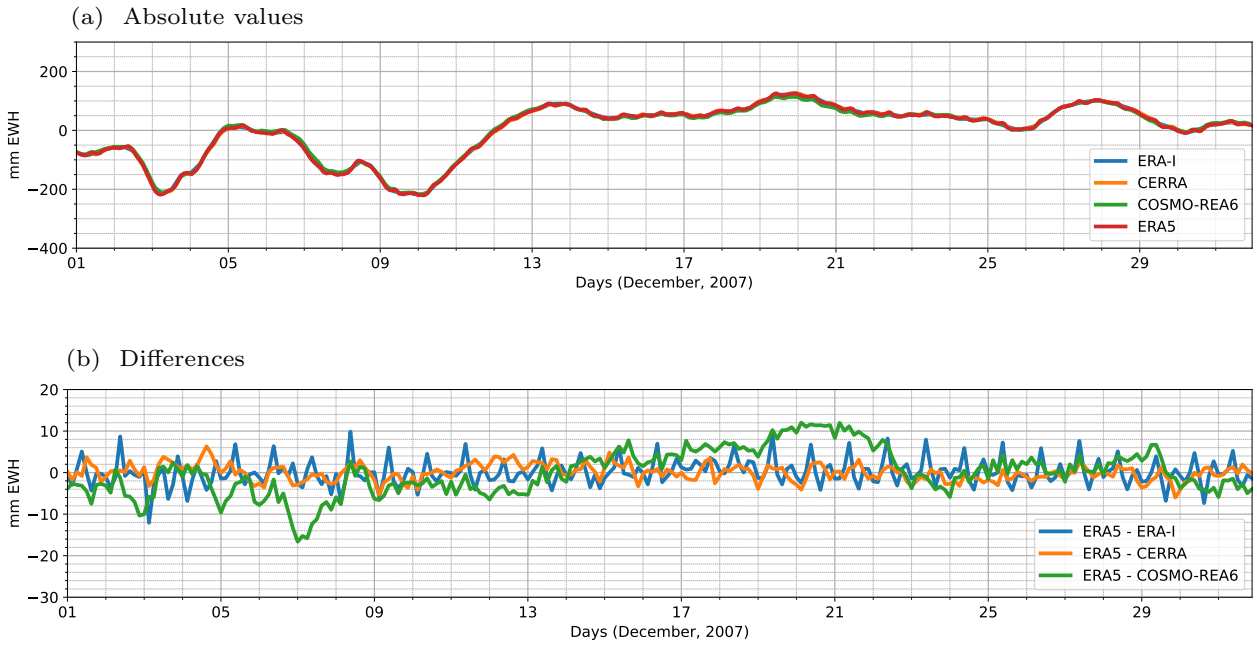

Figure S17. (a) Area-averaged sub-monthly vertically integrated atmospheric mass of all models within the investigated footprint C (Alps) and (b) the respective differences in comparison to ERA5 in December 2007.

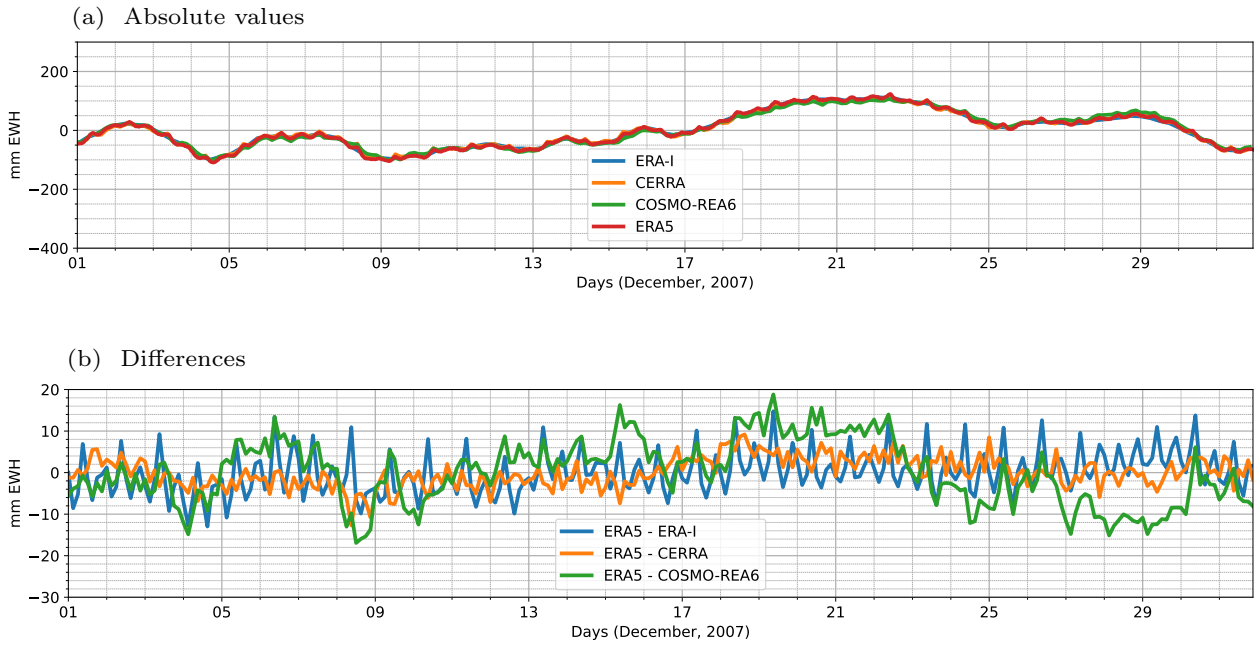

Figure S18. (a) Area-averaged sub-monthly vertically integrated atmospheric mass of all models within the investigated footprint D (Mediterranean Sea) and (b) the respective differences in comparison to ERA5 in December 2007.

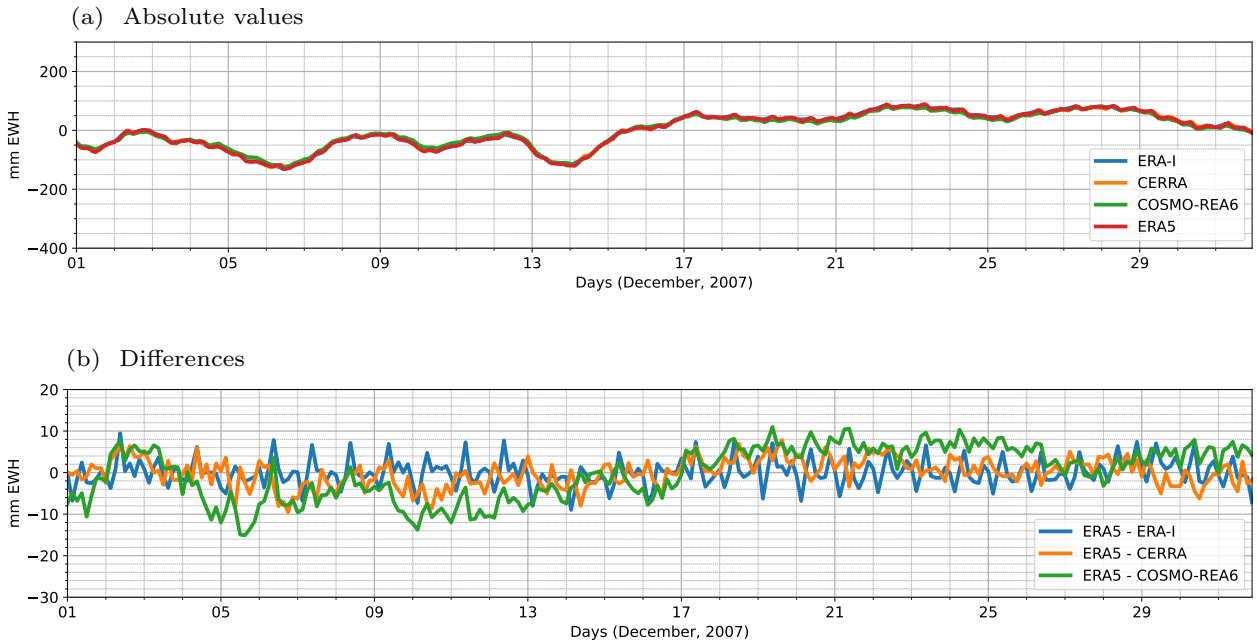

Figure S19. (a) Area-averaged sub-monthly vertically integrated atmospheric mass of all models within the investigated footprint E (Turkey) and (b) the respective differences in comparison to ERA5 in December 2007.

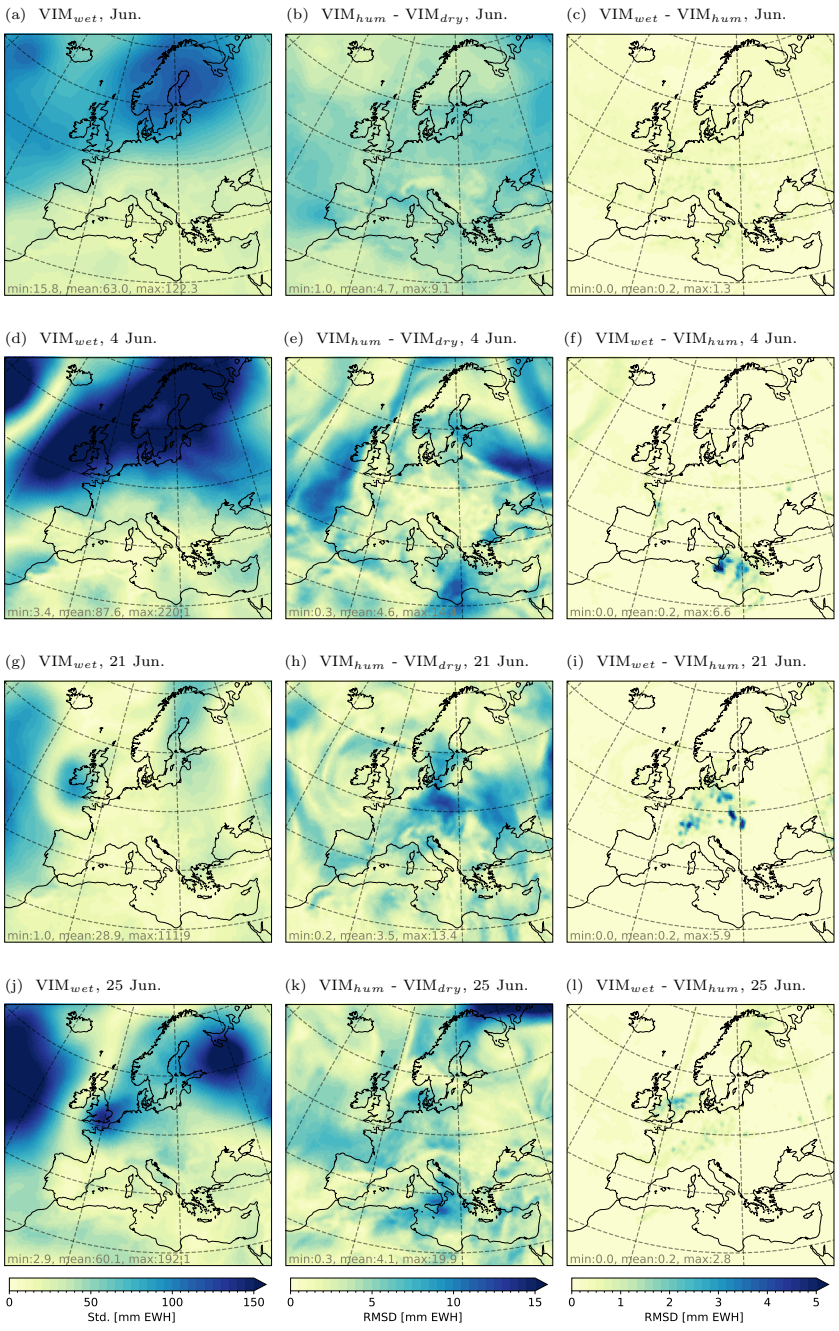

Figure S20. Vertically integrated mass (VIM) was computed for three cases based on (i) only dry air density variations (VIM$_{dry}$), (ii) dry air density and water vapor contributions (VIM$_{hum}$), and (iii) dry air, water vapor, and additional moisture fields including rain water content, cloud water content, cloud ice content and snow content (VIM$_{wet}$). The first row shows (a) standard deviation of VIM$_{wet}$, and the root mean square deviation (RMSD) for (b) VIM$_{hum}$ versus VIM$_{dry}$, and (c) VIM$_{wet}$ versus VIM$_{hum}$ for the entire June 2007. The other rows show the corresponding fields for 4, 21, and 25 June. Note the different scaling of the colorbars in each column.

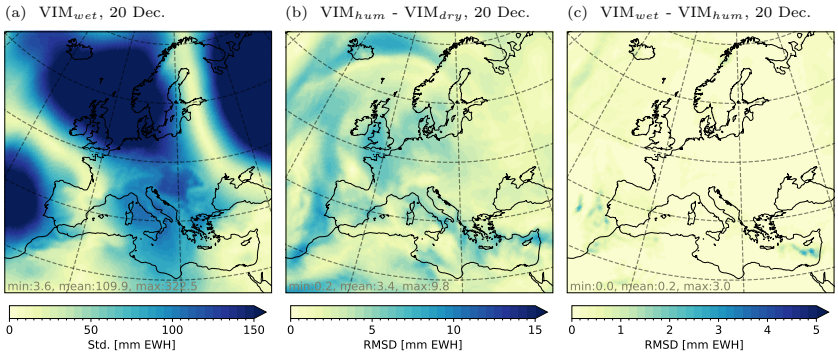

Figure S21. Vertically integrated mass (VIM) was computed for three cases based on (i) only dry air density variations (VIM$_{dry}$), (ii) dry air density and water vapor contributions (VIM$_{hum}$), and (iii) dry air, water vapor, and additional moisture fields including rain water content, cloud water content, cloud ice content and snow content (VIM$_{wet}$). Shown is the (a) standard deviation of VIM$_{wet}$, and the root mean square deviation (RMSD) for (b) VIM$_{hum}$ versus VIM$_{dry}$, and (c) VIM$_{wet}$ versus VIM$_{hum}$ for the 20 December 2007. Note the different scaling of the colorbars in each column.

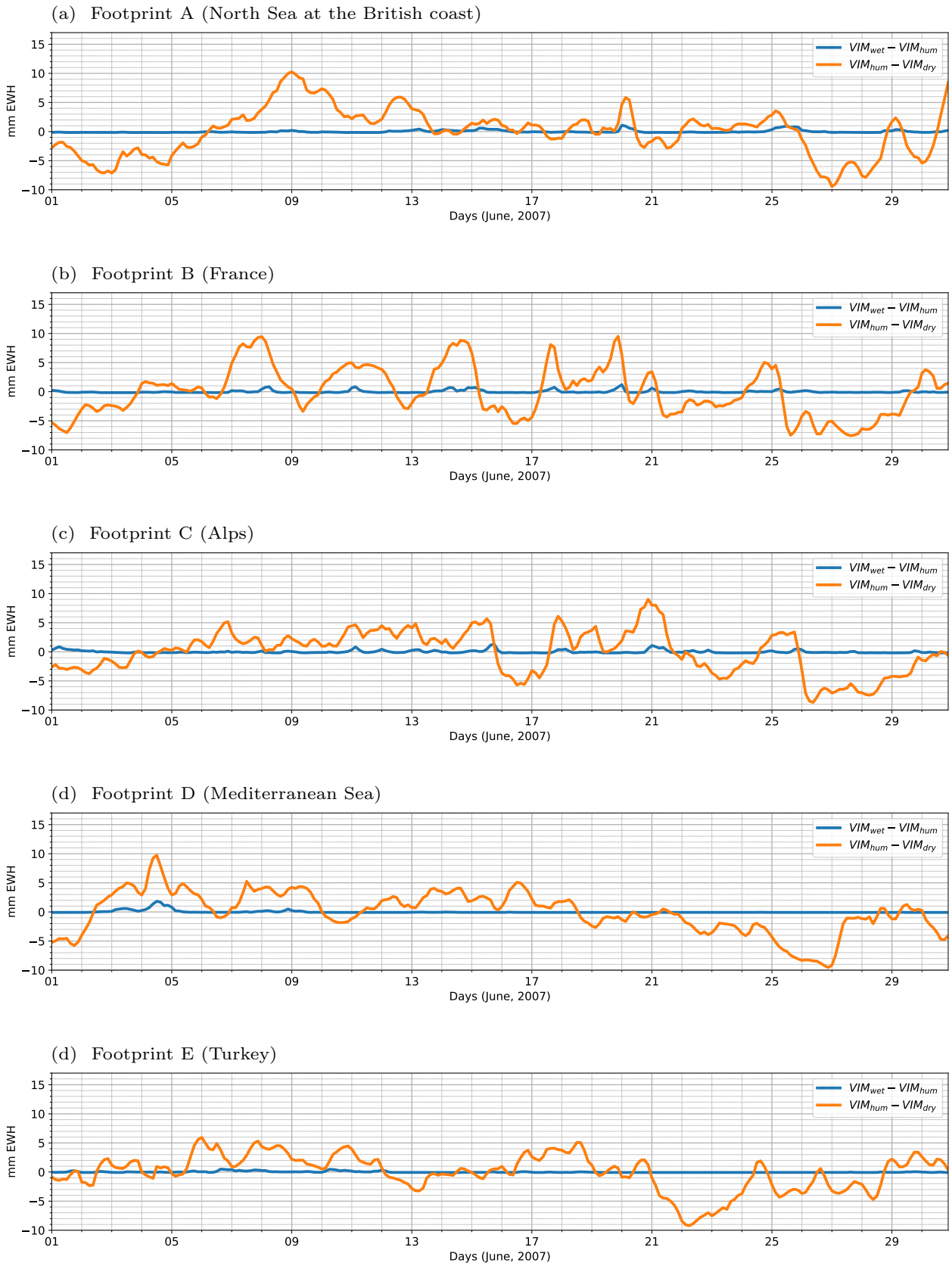

Figure S22. Contribution of water vapor and the liquid moisture fields for selected footprints over Europe in June 2007. We show differences between VIM_{hum} and VIM_{dry} in orange, and differences between VIM_{wet} and VIM_{hum} in blue.

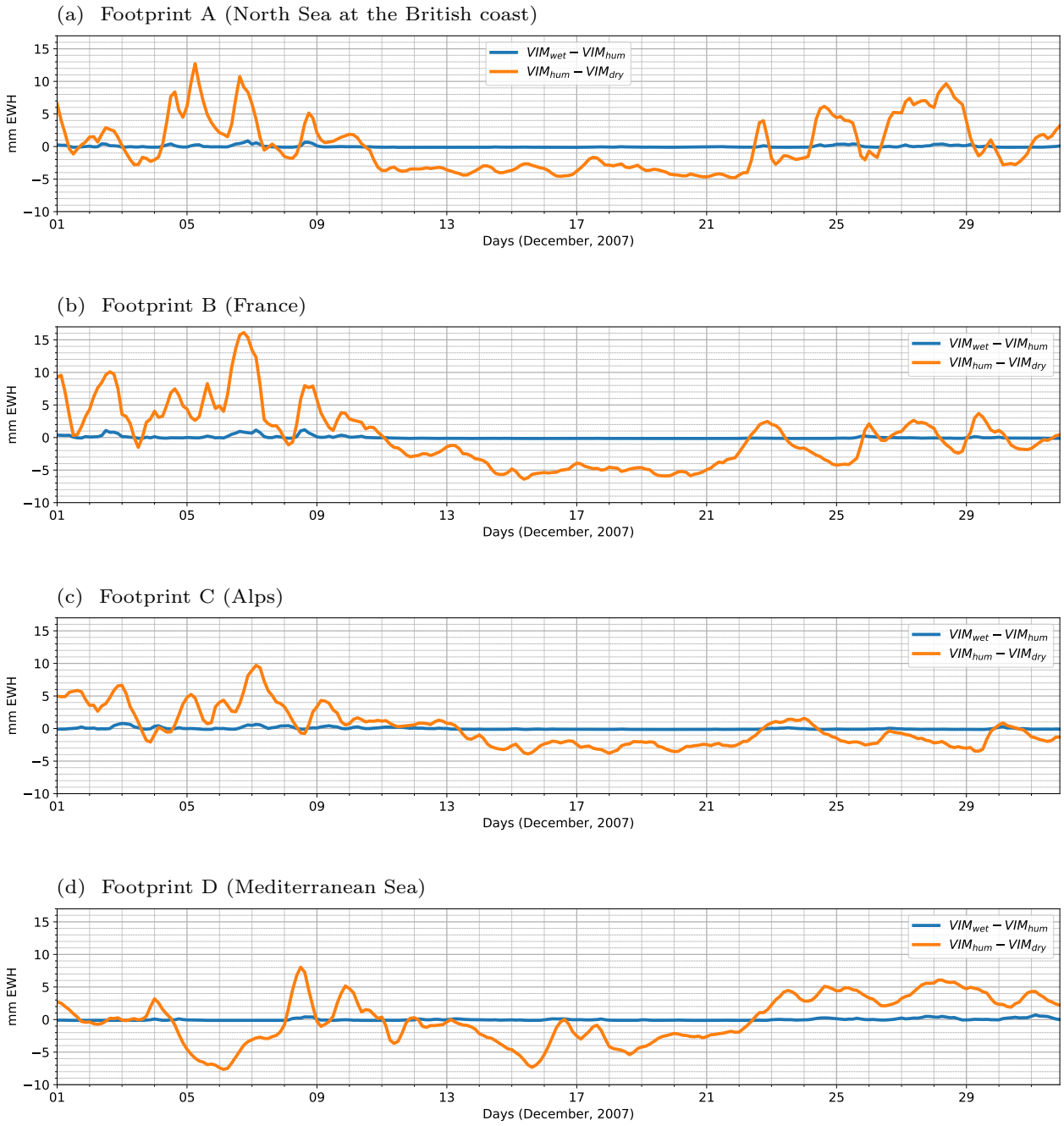

Figure S23. Contribution of water vapor and the liquid moisture fields for selected footprints over Europe in December 2007. We show differences between VIM_{hum} and VIM_{dry} in orange, and differences between VIM_{wet} and VIM_{hum} in blue.

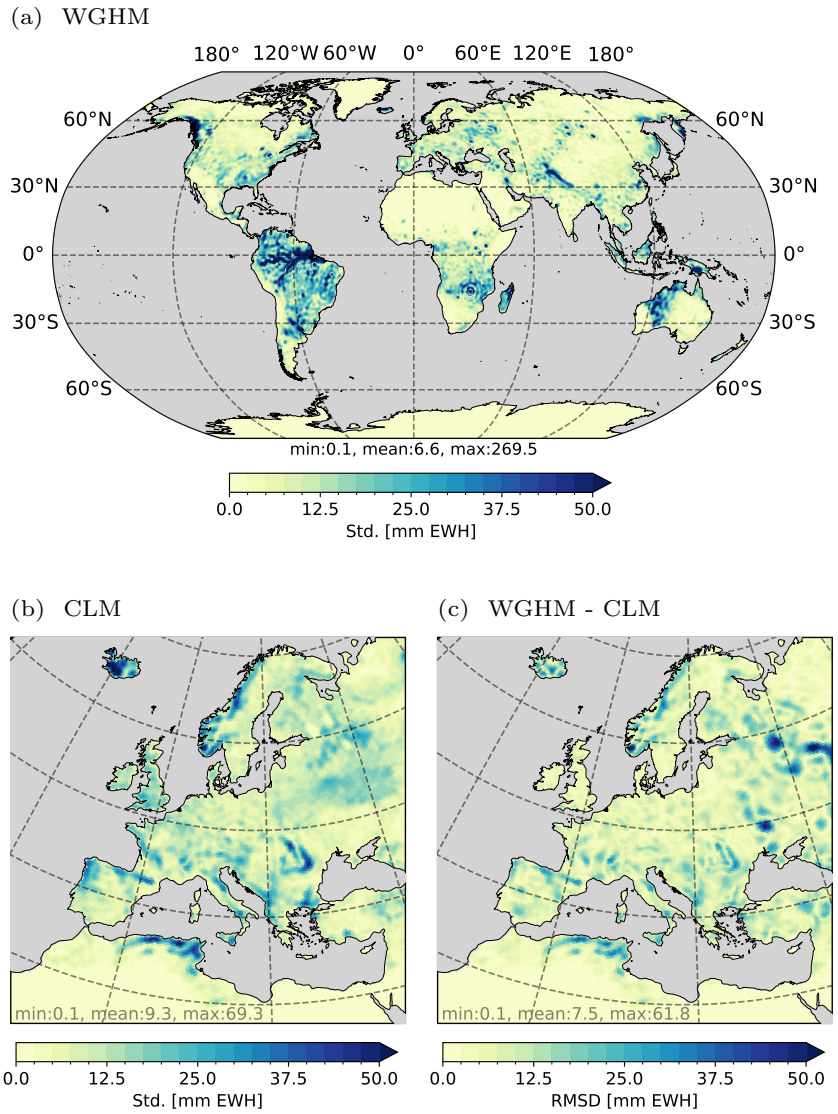

Figure S24. Standard deviation of sub-monthly variability of (a) WGHM- and (b) CLM-based water mass in March 2007. (c) Root mean square deviation (RMSD) between both models.

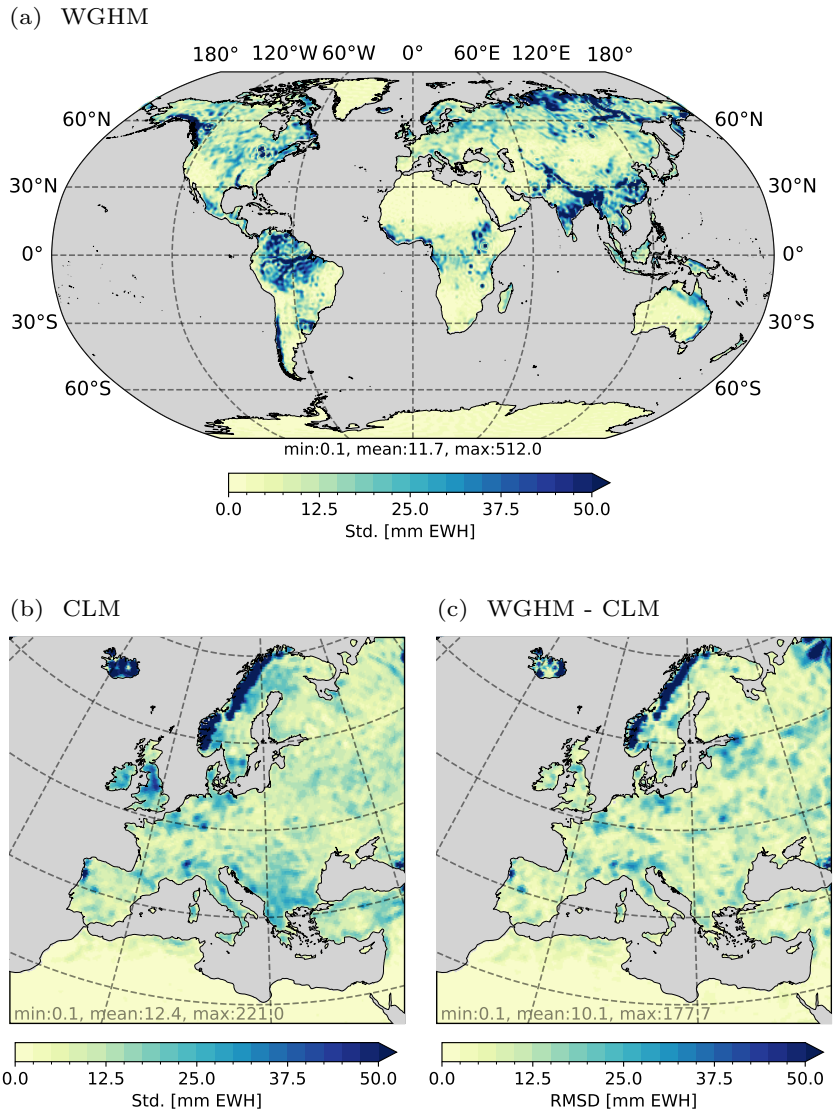

Figure S25. Standard deviation of sub-monthly variability of (a) WGHM- and (b) CLM-based water mass in June 2007. (c) Root mean square deviation (RMSD) between both models.

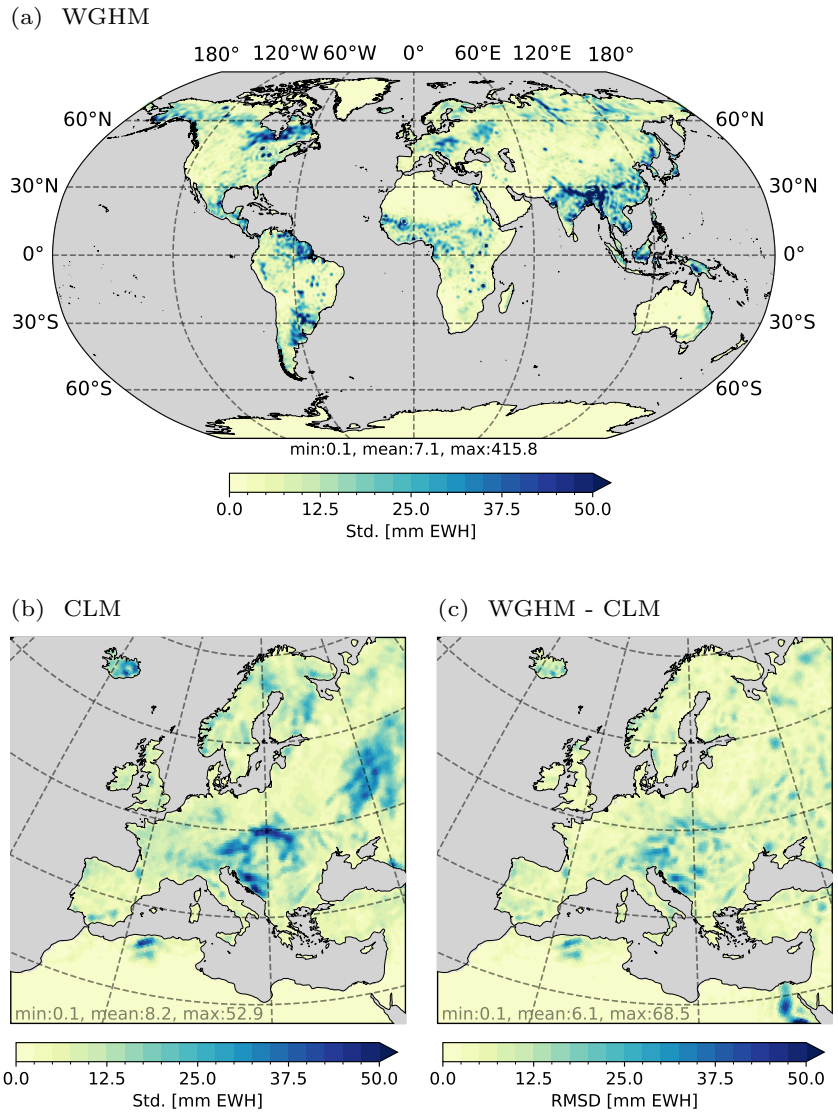

Figure S26. Standard deviation of sub-monthly variability of (a) WGHM- and (b) CLM-based water mass in September 2007. (c) Root mean square deviation (RMSD) between both models.

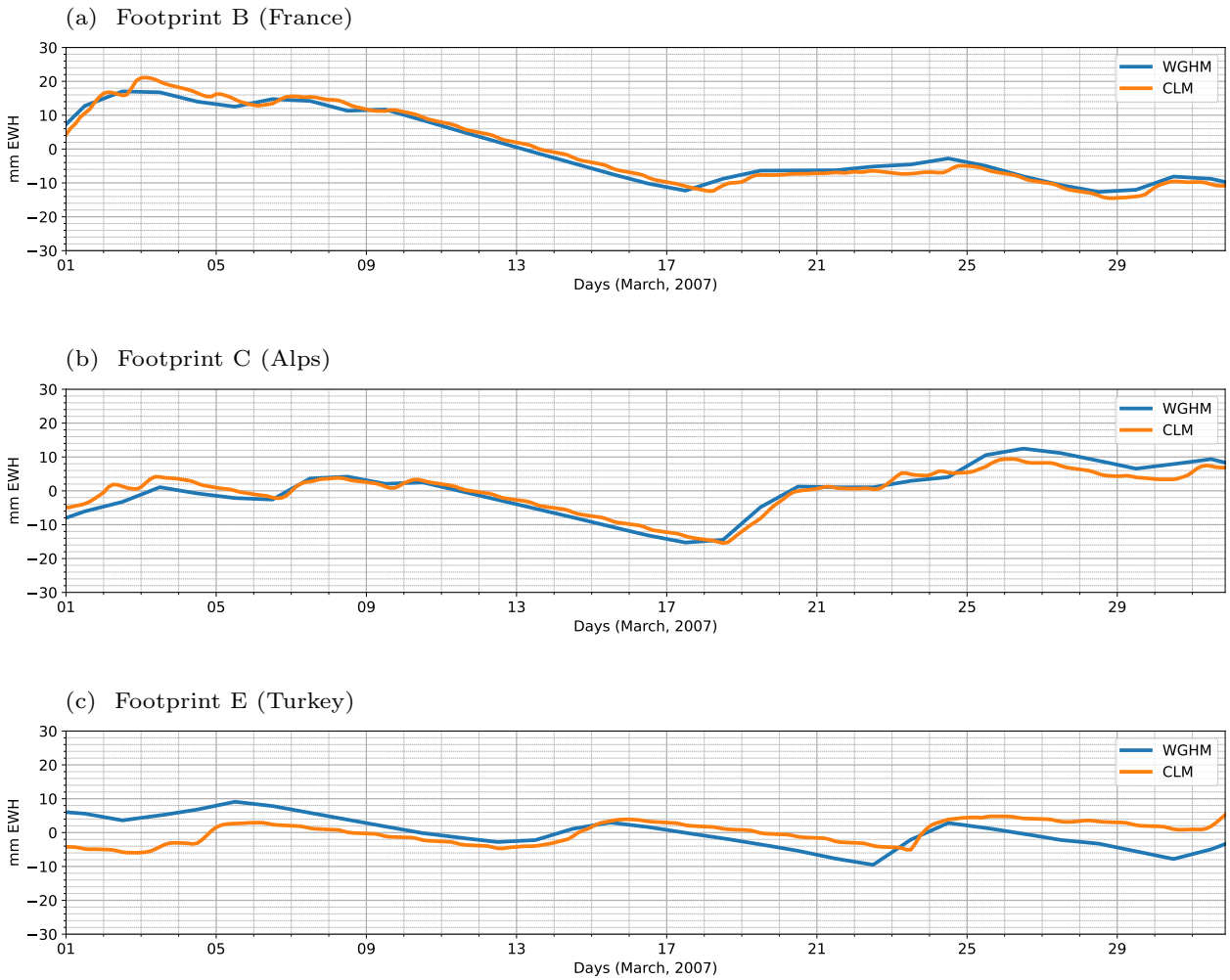

Figure S27. Sub-monthly terrestrial water mass variations of WGHM (blue) and CLM (orange) models for selected footprints over Europe in March 2007.

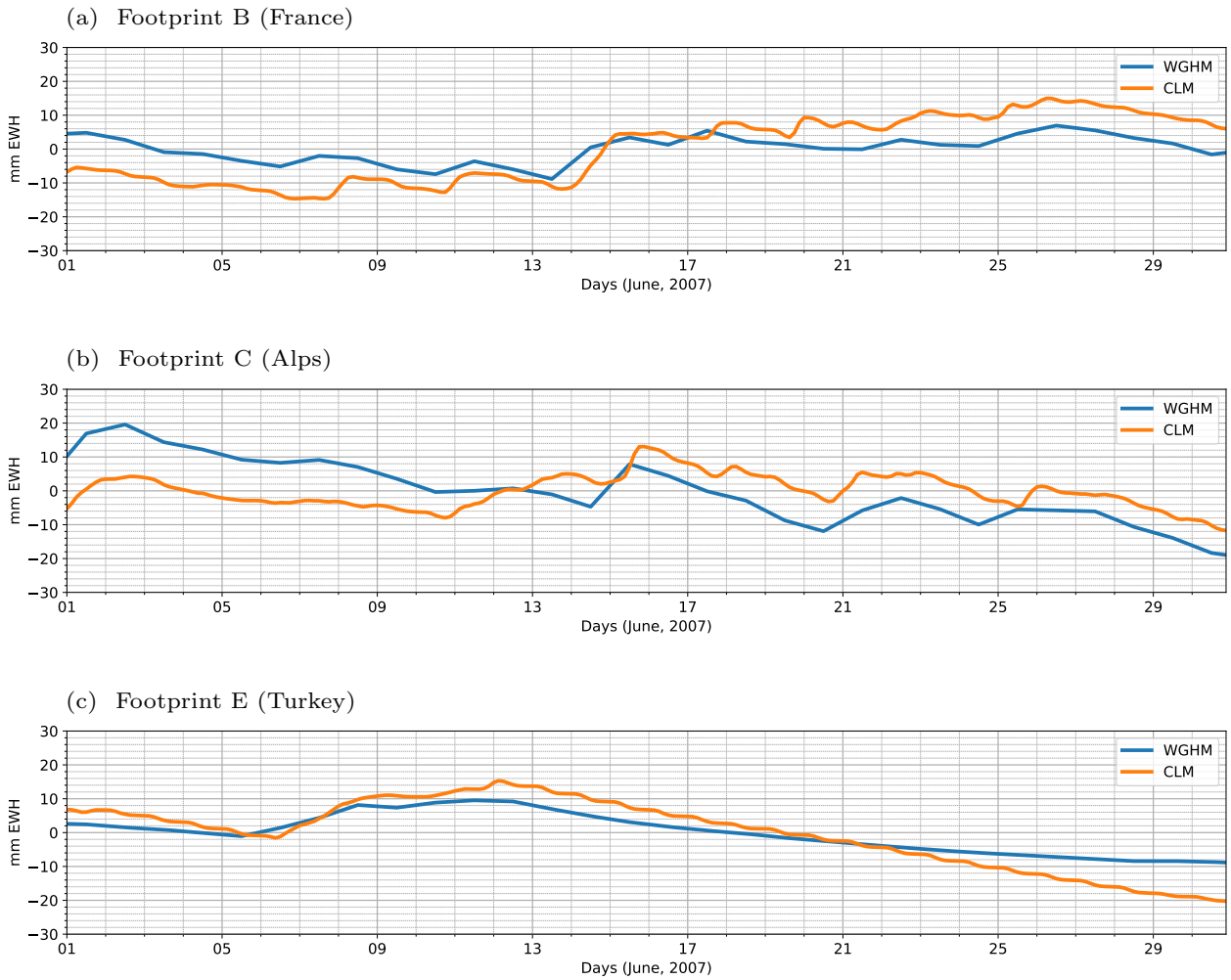

Figure S28. Sub-monthly terrestrial water mass variations of WGHM (blue) and CLM (orange) models for selected footprints over Europe in June 2007.

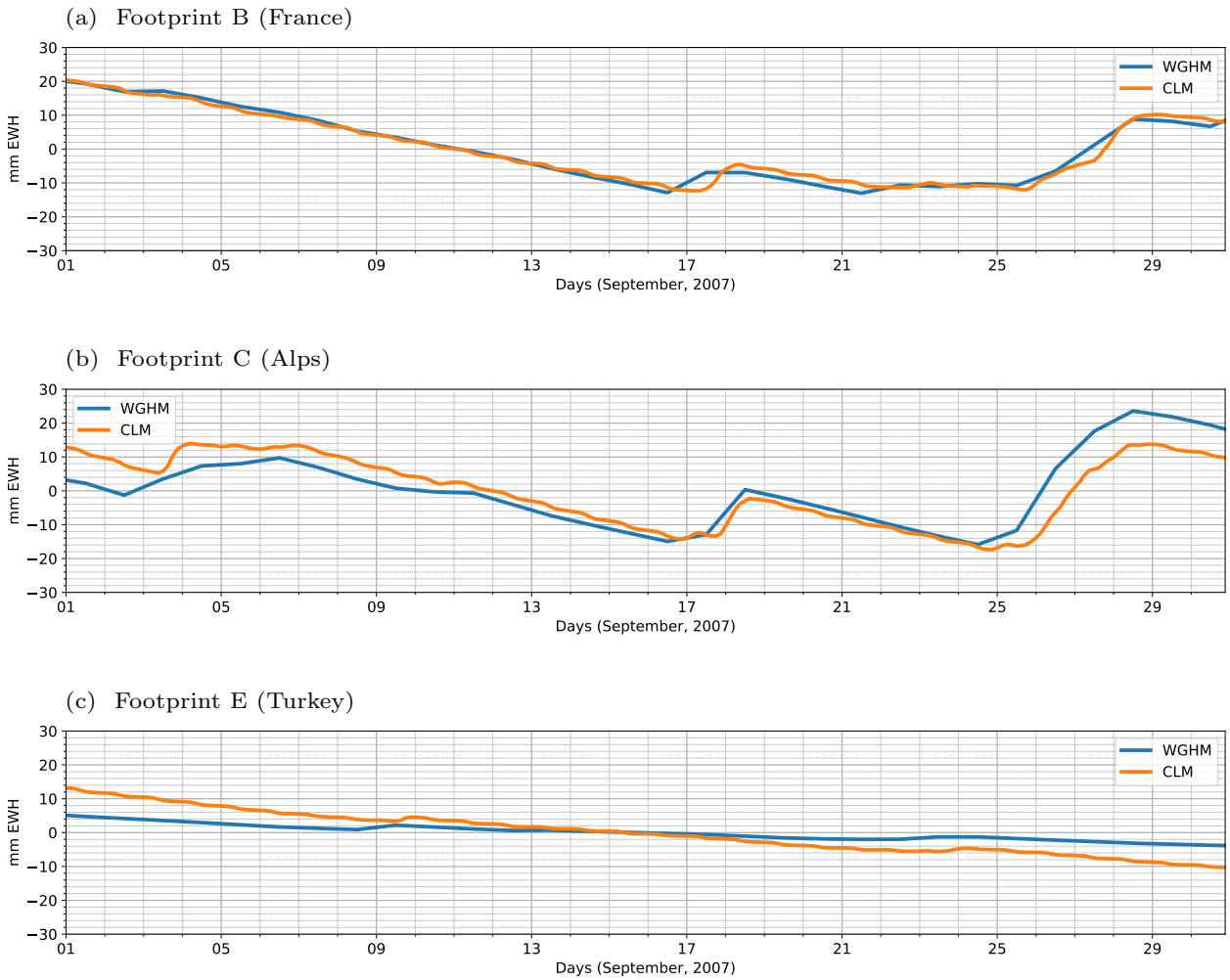

Figure S29. Sub-monthly terrestrial water mass variations of WGHM (blue) and CLM (orange) models for selected footprints over Europe in September 2007.

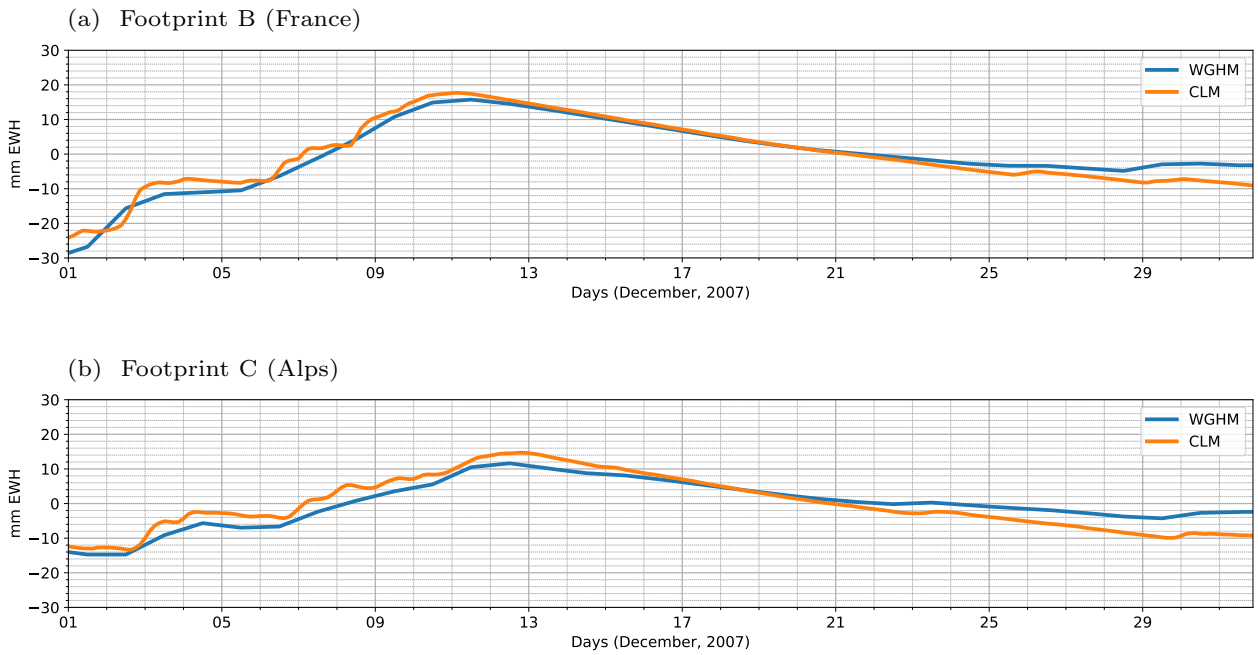

Figure S30. Sub-monthly terrestrial water mass variations of WGHM (blue) and CLM (orange) models for selected footprints over Europe in December 2007.